Ge and GeSi Electroabsorption Modulator Arrays via Strain and Composition Engineering

by

Danhao Ma

B.S. Energy Engineering

Pennsylvania State University, 2015

Submitted to the Department of Materials Science and Engineering in Partial Fulfillment

Of the Requirements for the Degree of

DOCTOR OF PHILOSOPHY IN MATERIALS SCIENCE AND ENGINEERING AT

THE MASSACHUSETTS INSTITUTE OF TECHNOLOGY

September 2020

Signature of Author:_____

Department of Materials Science and Engineering

Certified by:_____

Jurgen Michel

Senior Research Scientist, Materials Research Laboratory

Thesis Supervisor

June 4th, 2020

Certified by:_____

Lionel C. Kimerling

Thomas Lord Professor of Materials Science and Engineering

Thesis Supervisor

Certified by:_____

Anuradha M. Agarwal

Principal Research Scientist, Materials Research Laboratory

Thesis Supervisor

Accepted by:_____

Frances M. Ross

Professor of Materials Science and Engineering

Chair, Departmental Committee on Graduate Studies

This page intentionally left blank

Ge and GeSi Electroabsorption Modulators Arrays via Strain and Composition Engineering

by

Danhao Ma

Submitted to the Department of Materials Science and Engineering on May 28, 2020

in Partial Fulfillment of the Requirements for the Degree of

Doctor of Philosophy in Materials Science and Engineering

Abstract

Electronic and photonic integrated circuits serve as a promising platform for telecommunications and sensing applications. Electroabsorption modulators allow fast modulation, small device footprint, and low power consumption. Epitaxially grown GeSi films on SOI substrates are a suitable materials platform for integrated modulator applications. A modulator's operation wavelength adjustment and its system integration for broadband modulation are two major challenges of fabricating on-chip modulator arrays for telecommunication. Unlike Si MZI modulators, GeSi electroabsorption modulators are not broadband due to its limited working region near absorption edge for the Franz-Keldysh effect. Optimization of a modulator material for a target wavelength can be achieved by tuning material composition or applying strain to the material. In order to realize an integrated system with a broadband modulation, multiple electroabsorption modulators need to be fabricated individually and assembled onto a chip in a conventional

approach. Each fabrication step adds cost to design and processing. Integrating more modulators for multiple operating wavelengths allows a broader optical band coverage and higher optoelectronic data processing capacity, which is desirable with lower cost, simpler layout, and easier electronic and photonic circuits integration.

In this thesis work, a one-for-all strained GeSi modulator array design is proposed and demonstrated to cover a broad telecommunication band with multiple modulators designed and fabricated simultaneously in the same process flow. A stressor layer applies a homogeneous strain to a waveguide modulator. By changing a modulator width, strain in the modulator changes, tuning the material bandgap, therefore, adjusting the modulator operation wavelength. Modulators made of the same material can operate at various wavelengths with the same stressor layer with a simplified layout and device process flow.

The matrix of investigation consists of two compositions (Ge and $Ge_{0.99}Si_{0.01}$) and three types of strain (compressive, tensile, and no strains). Individual GeSi EAMs with waveguide width less than 2 μm have demonstrated an improved extinction ratio/insertion loss value from 1 to 1.7, which is the highest value among Si Mach-Zehnder, and GeSi electroabsorption modulators. Strained $Ge_{0.99}Si_{0.01}$ modulator arrays have demonstrated a broad optical bandwidth of ~100nm in C- and L-bands in telecommunication. An ultralow insertion loss of 2dB and high modulation speed above 100 GHz is achievable with minor improvements in electrode design. An increase in Si composition to 4% allows a strained $Ge_{0.96}Si_{0.04}$ modulator array to cover the optical wavelength from 1300nm to 1450nm. Strained GeSi modulator and detector arrays can be fabricated in the same process flow with the same stressor layers to achieve an integration of transmitters and receivers on a single chip with a simplified design layout and fabrication procedure. That presents

a promising platform for integrated photonic transceivers with an ultrawide optical coverage in the entire telecommunication bands.

Thesis Supervisors:

Jurgen Michel

Title: Senior Research Scientist, Materials Processing Center

Lionel C. Kimerling

Title: Thomas Lord Professor of Materials Science and Engineering

Anuradha M. Agarwal

Title: Principal Research Scientist, Materials Processing Center

Acknowledgments

I would like to thank many people for their encouragement and support during my Ph.D. journey at MIT. First, I sincerely thank my advisors Dr. Jurgen Michel, Professor Lionel C. Kimerling, and Dr. Anu Agarwal (better known as Jurgen, Kim, and Anu) for patiently guiding me through this incredible journey. The Electronic Materials (EMAT) group has been a fantastic place for collaborative, scientific, real-world applicable, and fun researches. I feel genuinely honored to be a part of the EMAT family. During my first year at EMAT, I mainly worked in passive photonic components for sensing applications, supervised by Anu and Kim. That was the first time I experienced cleanroom processing and microphotonic testing. We worked on Silicon Carbide and Silicon Nitride ring-resonators and waveguides for sensing applications. In the following three years, I worked in active photonic components for telecommunication applications, supervised by Jurgen and Kim. Since then, Germanium and Germanium Silicon became the most used words in my life. I am fortunate to have these three advisors who not only introduced me to microphotonics, but also taught me to become a persistent, caring, and responsible person. Thank you, Jurgen, Kim and Anu!

When I first met Anu at the Materials Research Society (MRS) annual meeting on a Thursday in November 2015, we talked briefly about the research projects at EMAT. I instantly felt that this is the group I wanted to join in. When you talk to a person, you can feel the culture that person is cultivated in. When I talked to Anu for the first time, I already felt the supportive and encouraging EMAT culture. The next day, I became a part of the EMAT family. Timing, location, and people have so many possible combinations. On Tuesday of that same week, before I met Anu, I have exchanged an email with Jurgen to set up a meeting on the following Monday.

Since I decided to work on the sensor projects with Anu by the end of that week, Jurgen and I did not get to meet on that Monday. About seven months later, Jurgen and I finally had a formal meeting in his office to discuss the GeSi electroabsorption modulator project. That marked the starting point of this thesis work. Jurgen has always been there to offer valuable advice and provide hand-on guidance on operating the Ge epitaxial growth tool and experiments. I worked closely with Jurgen in the past three years. We overcame many obstacles together in the project. He reshaped my scientific thinking and constantly challenged me to become a better researcher. His generosity of time, efforts, and guidance is deeply appreciated. Kim has also been supportive throughout my PhD journey. Kim taught me how to maximize the usage of time and be well organized on research plans. Kim has also provided valuable advice on my job searching. "…learning and experience, you will be a leader as you keep learning…" his words lighted up the path when I was uncertain about my career choice. To Kim, Jurgen, and Anu, I extend great thanks!

I sincerely thank the support of my committee members, Professors Juejun Hu and Caroline Ross. Both Professors Hu and Ross have provided different perspectives and inspiring new ideas to pursue and questions to answer. Next, I want to thank all the wonderful EMAT and Photonic Materials (PMAT) group members. Specially thanks to Dr. Zhaohong Han, Dr. Qingyang Du, Dr. Peter Su, Dr. Jifeng Liu, Dr. Xiaoman Duan, Yifei Zhang, and Eveline Postelnicu. Zhaohong and Qingyang are my mentors on cleanroom processing and photonic device fabrication. I called them so many times during my processing whenever a question or a concern came up to my mind. They always picked up the phone and answered all my questions patiently. Their generosity in transferring their processing knowledge and experience helped me tremendously in processing skills development. I also want to thank Cory James and Lisa Sinclair, the two main administrative assistants for the group during my time at MIT. Without their help, none of my samples would be

sent to my collaborators overseas; none of my paperwork would be handled on time. They have much enabled the smooth functioning of the group.

I offer gratitude to all of my collaborators: Robin Singh, Professor Suchol Savagatrup, Dr. Peng Xing, Professor Dawn Tan, Dr. Bin Wang, Dr. Ruitao Wen, and Dr. Yiding Lin. Robin and I have worked on aerosol sensor project since 2016. We have demonstrated aerosol particle sensing using micro-ring resonators, which could be used for drug delivery. We have been supportive of each other in sharing fabrication and testing experiences. Suchol and I have worked on complex emulsion droplet sensor project since 2017. We have demonstrated using microphotonic devices to sense the droplet transformation, which could be used for environmental sensing. Peng, Dawn, and I have worked on amorphous Silicon Carbide resonators for nonlinear optics. We have shown the highest intrinsic quality factor and strong Kerr nonlinearity in amorphous Silicon Carbide resonators, which makes amorphous Silicon Carbide a promising platform for amorphous nonlinear photonics. Dr. Bin Wang, Dr. Yiding Lin, Dr. Ruitao Wen, and I have worked closely on straining engineering for Ge and IIIV active photonic devices. Dr. Yiding Lin and I have discussed with our advisor Jurgen frequently on our projects since 2018. We have both worked on strained Ge waveguide integrated photonic devices. Yiding has successfully demonstrated an enhanced performance of strained Ge photodetectors and his valuable insight has allowed us to precisely model and control the strain effect in photonic devices, which is critical to the successful demonstration of strained GeSi modulator arrays in this thesis work.

I want to thank all of the staff that I have worked with at MIT and Harvard: the Center for Materials Science and Engineering (CMSE), Microsystem Technology Laboratories (MTL), and the Center for Nanoscale Systems (CNS). The staff has always been tremendously generous with

their time. Special thanks to Dr. Vicky Diadiuk, Luda Leoparde, Dr. Shiahn Chen, Kurt Broderick, Dennis Ward, and Mark Mondol.

I owe a huge thank you to my friends throughout my five years at MIT: Dr. Zhaohong Han, Yifei Zhang, Zhiwei Ding, Tian Xie, Gabriel Loke, Robin Singh, Hejin Huang, Jiayue Wang, Hongzhou Ye, and Xinghao Li. They have always been around through my good times and rough moments. We are a big family at MIT, and have celebrated many Chinese Festivals together on the fifth floor common kitchen in Ashdown house with dishes of Chinese food, bottles of wines, and cases of beers and cards. Zhiwei, Tian, and Gabrial were in the same classes with me in the first year of graduate school. Since I majored differently at College, I struggled a lot in the first year's courses. Zhiwei and Tian have been really patient in guiding me on the homework and preparing the qualification exam together. Without their help, I would not pass my first-year qualification exam. Yifei and I have explored various cuisines in Great Boston Area; we have a similar appreciation for wines and whiskey. Most of my friends will be graduating this year. I wish them all the best, and thank you for the friendship that will last way beyond our time at MIT.

Finally, I want to thank my family for their unconditional love and support: My parents, Weiping Wang (王伟萍) and Zhibin Ma (马志斌), my significant other, Albee (Ziyu) Ge, and our puppy Danzhu Ma. My parents have been role models in my life. As senior civil engineers, they have taught me the core values of being an engineer: (a) passion, passionate about what you do; (b) teamwork, support and care for each other; (c) ownership, take the initiative and ownership on work, learn from the mistakes. Without their support, I would not be able to come to the U.S. for high school, college, and graduate school. They always encourage me to explore and find my own path in life. When I was in elementary school, they supported me in doing professional gymnasium

for four years and joining the state swimming diving team for one year. We talk at least once a week to share what happens in life, like close friends. My significant other, Albee, and I first met at a student event in Beijing in 2017. I knew the first time we met; she would be hard to forget. We have been on a long-distance relationship for almost three years. Albee is graduated from Wake Forest University and is going to the University of Pennsylvania for her master's degree. The quarantine period due to COVID-19 has allowed us to spend more time together. For us, the smallest distance is too great, and the greatest distance can be bridged. I love you!

Table of Contents

List of Figures and Tables

Chapter 1 Introduction

Germanium (Ge) and Germanium Silicon (GeSi) alloy are the valuable semiconductor materials as they have been gaining attention as the critical materials for electronic photonic integrated circuits (EPICs) because of their functions as emitter, photodetector, and modulator [1-14]. They are known as *c*omplementary metal–oxide–semiconductor *(*CMOS*)* compatible materials. Ge and GeSi can be directly grown and processed on silicon (Si) substrates. This chapter explains why Ge and GeSi are the bridging force for electronic and photonic integration, and why the modulators made from Ge and GeSi have promising performance over other modulators.

1.1 Germanium and Germanium Silicon Materials Advantages and Challenges

Germanium processing is readily adaptive with conventional silicon CMOS processing. Photodiodes made from Ge have been implemented in the process development kit (PDK) as a part of the on-chip optical components utilizing the electronic and photonic integrated circuits layout. These applications include large-scale systems such as the telecommunications system and micro-scale devices such as on-chip sensors. Since silicon is the primary material used in these systems, integration capability with silicon is an advantage of germanium. As an example, for the telecommunication application, which utilizes multiple channels to transmit signals in the 1300nm regime and 1550 nm regime to cover a broad telecommunication band, in which silicon is transparent over the optical bandwidth. Therefore, silicon is often used to fabricate passive components such as waveguides and active components as a phase modulator utilizing its electro-optic effect for transmitting data. Materials such as germanium and germanium silicon alloy, are necessary to be used to fabricate detectors and electroabsorption modulators utilizing the field-induced absorption effect. There are various group III and group V materials based devices

currently being used as photodetectors with decent responsivity and high bandwidth. However, the integration challenge is present for high-volume manufacture and integration. Compared to III-V materials, Ge and GeSi epitaxy on Si substrate is a mature technique for commercial application and production.

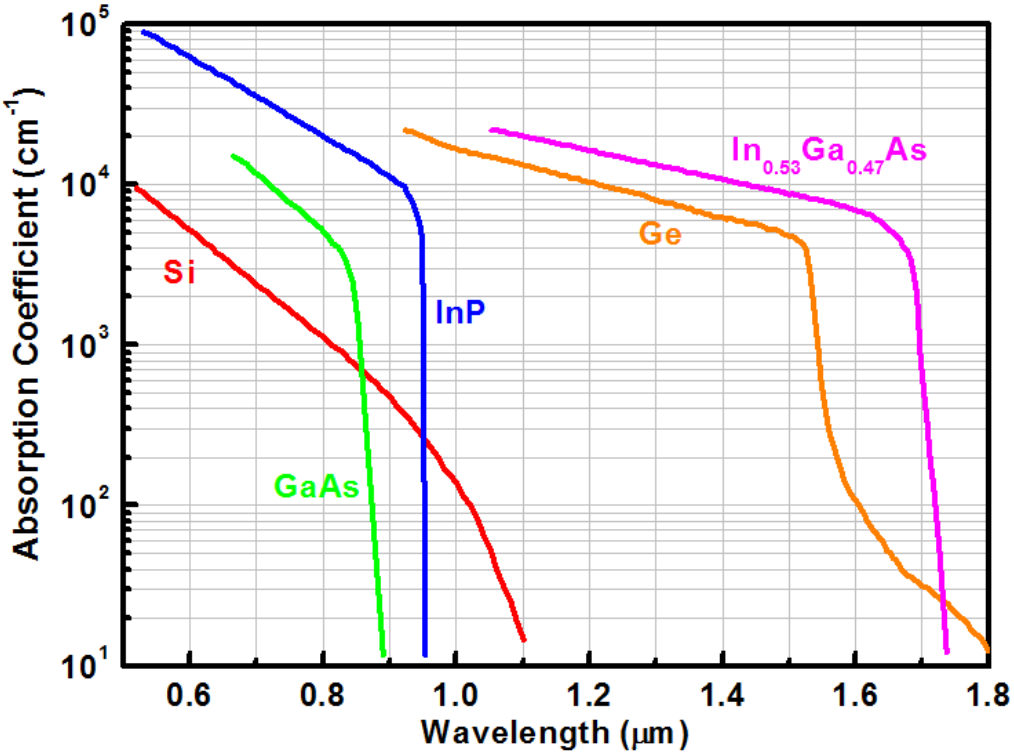

Figure 1.1 Absorption coefficient as a function of wavelength for various materials from visible to near IR range [15].

The challenge for Ge on Si integration lies in the lattice mismatch of 4% between Ge and Si crystal lattices, creating significant stress in the Ge thin films. This stress is relaxed via the generation of misfit dislocations near the Ge-Si interface and threading dislocations penetrating through the Ge film to a free surface. These dislocations degrade the device performance, such as introducing higher leakage current in photodiodes. Various techniques

have been developed to reduce the threading dislocation density in the past. One way to reduce the dislocation density in the active region of the diode is to use relaxed buffer layers where the percentage of Ge is increased slowly over a few microns of GeSi [16-20], which is suitable for solar cells but the thick buffer region causes planar alignment issues in between the components in the EPICs. Another approach that has been developed and used is the cyclic annealing, which drives the dislocations to the sides or edges of the active regions due to thermal-induced stress aiding the gliding of the dislocations [21-22]. Detailed Ge and GeSi epitaxial film growth and quality evaluation are discussed in Chapter 2.

Another challenge posed by working with germanium is its lack of a good native oxide. Not like Si has its excellent native oxide of silicon oxide (SiO_2). Germanium oxide (GeO_2) is water-soluble, which makes it difficult to perform Ge surface oxidation and passivation. In this thesis work, SiO_2, silicon nitride (SiN_x), and aluminum oxide (Al_2O_3) are used in the Ge and GeSi device processing to serve as the passivation layers to improve the surface passivation and electrical and optical performance of the modulators, which is discussed in Chapter 6. Another processing and integration challenge is their difference in melting points among Ge, Si, and contact metals. Germanium requires lower processing temperatures than silicon does. The melting point of Si is 1410 °C, while the melting point of germanium is 937°C. After germanium deposition, processing temperatures must be kept low to avoid interdiffusion of silicon and germanium, and also reduce the dopant and impurity diffusions within the material layers. Thermal budgeting is crucial for a successful Ge and Si integration, which is discussed in detail in the processing flow section in Chapter 6.

1.2 Electronic photonic integrated circuits in the telecommunication system

As more and more transistors are designed and fabricated onto each chip, the efficient connection between the chips and data storage sections is becoming a challenge [23-28]. The electrical interconnects that are commonly used to connect chips do not have a high enough data transfer rate and produce a large amount of heat to be dissipated. One method is to use optical interconnects between the chips. An optical fiber is more efficient than an electrical interconnect because there are no substantial electrical contacts to charge up. Another advantage of optical fibers is that different signals can simultaneously be sent through the fiber at different wavelengths using a process called wavelength division multiplexing (WDM). These advantages of optical interconnect would significantly boost processing power and efficiency if optical links were being integrated into the chips. As shown in the following schematic as an example of an optical interconnect, these optical links are integrated within the chips. That makes the interconnect fabrication be obligated to the CMOS process; this requires efficient monolithic integration between electronic units for driver and controller, and photonic circuits for modulation, detection, and light transmission. It includes a strict set of design rules as to what materials can be used and what processing steps occur. The products would be efficient, low cost, and high speed optical interconnects transceivers, and others [28-29]. As an illustration of the cross-section of the monolithically integrated electronic and photonic circuit components, the advantage of monolithic integration is the reduction of the complexity and packaging cost [29]. The other integration techniques, such as 2.5 D or 3D die stacking strategies, face the challenge of parasitic capacitance management of the control electronics. The low power, optical hybrid CMOS-Si photonic integrated transceivers have been demonstrated with a

modulation speed up to 40-56Gbaud [30-33]. In many cases, the functionality of electronic control units is not optimized for photonic transceiver applications due to the lack of design integration between electronic and photonic components, which requires attention and effort for the future EPICs applications.

The active photonic components, including photodetector, modulator, and light emitter, should be capable of working at the designated wavelength range such as C and L bands. These device functions can be covered by the Ge direct bandgap of ~0.8eV in energy and 1550 nm in wavelength. Therefore, it becomes essential to be able to finely tune the material bandgap to broaden the materials working wavelength with the ambition to cover both C and L bands. There are generally two approaches to alter the material bandgap. One is to involve alloying of various materials to achieve the desired bandstructure; another method is to introduce strain in the material intentionally. This thesis work considers both approaches with a focus on strain engineering and newly developed stressor layer processing for modulator arrays applications, which largely simplifies the design layout and processing steps for the array device fabrication.

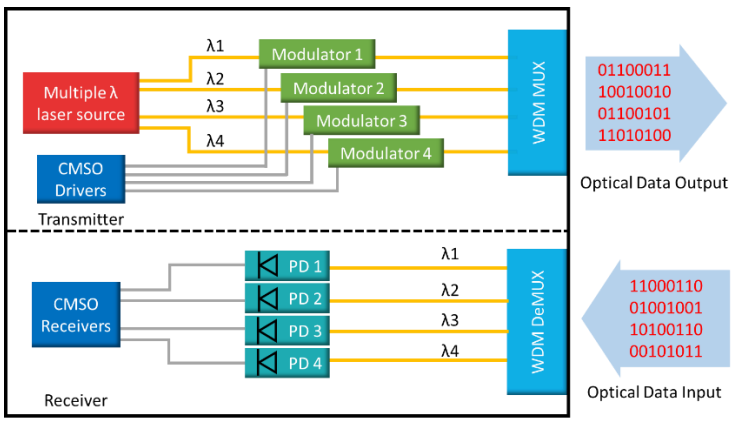

Figure 1.2 Schematic of a four-channel optical transceiver using waveguide integrated light emitters, modulators, and photodetectors in coherence with the on-chip electronic components.

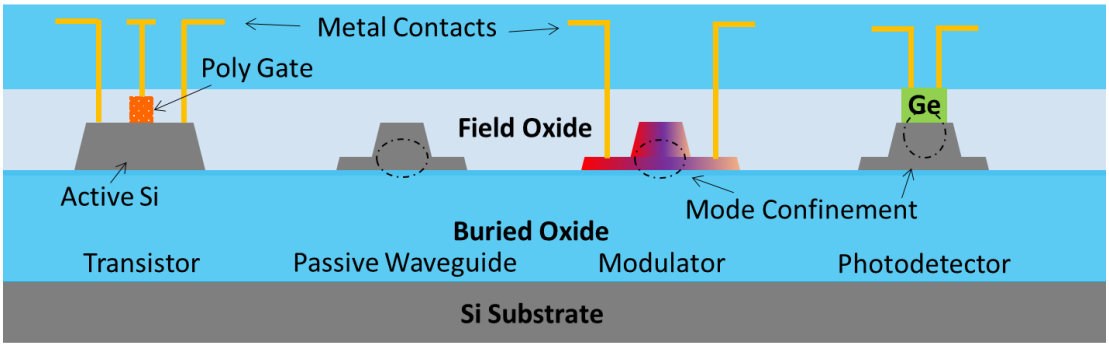

Figure 1.3 Schematic of the components cross-sections for a conventional EPIC layout [12].

1.3 Waveguide Integrated Silicon and Germanium Modulators

Different modulators are reviewed in this section, along with their figures of merits to make a reasonable comparison among various modulators reported in the literature. These are Mach-Zehnder interferometer modulators, ring resonator-based modulators, and electroabsorption modulators. The modulation mechanisms are introduced along with the specific modulator structures.

Mach-Zehnder Interferometer (MZI) modulators

The MZI modulators use the plasma dispersion effect, which relates to the free carrier concentration in a semiconductor. The change in the free carrier concentration during carrier injection changes both the real and imaginary parts of the refractive index. This can be expressed by the Drude-Lorenz equations that relate the concentration of electrons (N_e) and holes (N_h) to the absorption coefficient α and refractive index n. The change in the absorption coefficient and refractive index, Δα, and Δn, with the change in electron and hole densities, are expressed as:

$$\Delta\alpha = \frac{e^3\lambda_0^2}{4\pi^2 c^3 \varepsilon_0 n}\left(\frac{\Delta N_e}{\mu_e (m_{ce}^*)^2} + \frac{\Delta N_h}{\mu_h (m_{ch}^*)^2}\right) \quad \text{Eq. 1.1}$$

$$\Delta n = \frac{-e^2\lambda_0^2}{8\pi^2 c^3 \varepsilon_0 n}\left(\frac{\Delta N_e}{m_{ce}^*} + \frac{\Delta N_h}{m_{ch}^*}\right) \quad \text{Eq. 1.2}$$

As for Si material, numerous experiments have been done in the literature to arrive the empirical expression of free carrier induced refractive index and absorption coefficient change, as expressed for Si at the wavelength of 1550nm:

$$\Delta\alpha = \Delta\alpha_e + \Delta\alpha_h = 8.5 \times 10^{-18}\Delta N_e + 6.0 \times 10^{-18}\Delta N_h \quad \text{Eq. 1.3}$$

$$\Delta n = \Delta n_e + \Delta n_h = -(8.8 \times 10^{-22}\Delta N_e + 8.5 \times 10^{-18}(\Delta N_h)^{0.8}) \quad \text{Eq. 1.4}$$

where Δn_e is the change in refractive index due to the change in free-electron carrier concentrations; Δn_h is the change in refractive index resulting from the change in free hole carrier concentrations; $\Delta\alpha_e$ is the change in absorption resulting from the change in free-electron carrier concentrations; and $\Delta\alpha_h$ is the change in absorption resulting from change in free hole carrier concentrations.

The commonly used structure in MZI modulator is the PIN diodes in revere biased for carrier depletion, as shown in the following figure. The free carrier concentration change inside the waveguide alters the refractive index of the modulator material. In the PIN phase modulator, the space charge region is expanded as the reverse bias applied across the diode is increased, hence sweeping out carriers from the waveguide. Therefore, figures of the metric for the phase modulator are the number of carriers that can be moved in and out of the modulator waveguide by a certain voltage change, also known as linear capacitance, and so the optical mode overlap with the depletion region. The higher the linear capacitance and lower the driven voltage. The energy used to drive the modulator at high speed needs to be evaluated as well. In general, the modulator energy

consumption can be expressed as $E = (1/2)CV^2$, where C is the capacitance, V is the driving voltage. An increase in the phase modulator capacitance tends to reduce the voltage needed to reach the specific phase shift, such as a π shift; therefore, it reduces the power consumption. However, there is a practical limit for the capacitance increase. The excess amount of free carriers due to capacitance increases causes free-carrier absorption. For phase modulators, the loss might come from the free-carrier absorption of the modulator materials or line edge roughness of the waveguide due to the fabrication. Eventually, the device loss becomes the limiting factor for the phase modulator, such as MZI modulators. The advantage of the MZI modulators includes its excellent broadband modulation performance and temperature tolerance. Their disadvantages are large device footprint, large power consumption, and potential complexity for traveling wave electrodes design, which associates with its large device size and high-speed requirement. Many academic groups and industrial research labs have demonstrated Si MZI modulators operating at 1300nm or 1550nm wavelength range with a modulation rate up to 50 Gbit/s [34-41]. The reported modulators normally have the length in the order of several millimeters. The modulator's optical bandwidth is as broad as 100nm.

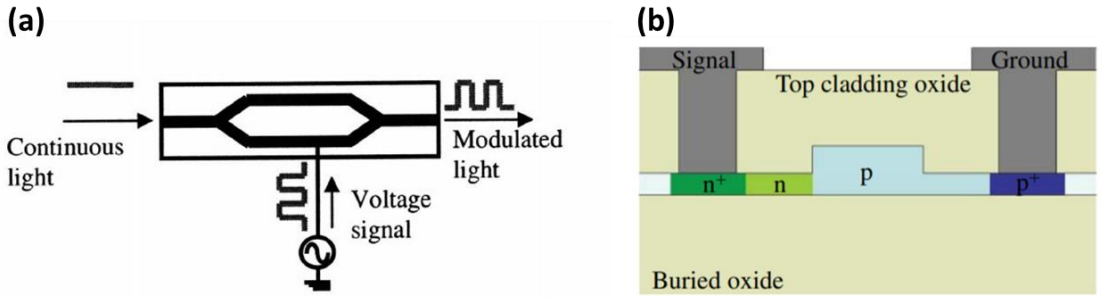

Figure 1.4 (a) Schematic of MZI modulator [35], (b) cross sectional diagram of phase modulator [37].

Ring Resonator-based Modulator

The silicon ring resonator structure is the benchmark structure in Si modulators for its small footprint and low power consumption. The use of ring resonator takes advantage of an optical resonance effect to enhance optical confinement and effective optical path, which enhances the change in the refractive index without sacrificing the device footprint, as shown in the following schematic [42-51]. The p-i-n junctions are embedded across the ring resonator to create variations in carrier concentrations. The plasma dispersion effect is used in ring resonator-based modulators, similar to the phase modulation in MZI modulators. The Si ring resonator operates under a forward bias injecting carriers into the waveguide core. The advantage of a ring resonator-based modulator is its compact device size and lower power consumption. The disadvantage includes its wavelength-selective resonator coupling, which causes a narrow optical modulation window and temperature sensitivity demanding a sophisticated thermal management strategy. The Si ring resonator-based modulator has been demonstrated with the modulation rate up to 44 Gbit/s and dynamic power consumption as low as one fJ/bit and voltage swing as low as 0.5 V at 1550nm operation wavelength [47]. Its optical bandwidth is only 0.1 nm due to the nature of resonator critical coupling.

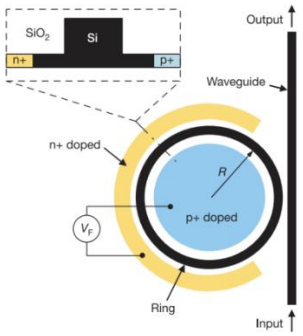

Figure 1.5 Schematic of ring resonator based Si phase modulator

Electroabsorption modulators

The Electroabsorption modulators utilize the Franz-Keldysh effect. The Franz-Keldysh effect is caused by tilting the energy bands of a semiconductor due to an applied electric field [25]. As illustrated in Figure 1.6, an electron can transit from the valence band to the conduction band by absorbing a photon with energy $hv > E_g$ in the absence of an external field. Under an external electric field, the maximum of the valance band, the minimum of the conductance band along with the wavefunction of holes and electrons may extend to the bandgap between valance and conductance bands. An electronic transition with lower energy than the bandgap energy E_g can happen through a photo-assisted tunneling effect. If the incident light energy is near the bandgap E_g, the absorption spectrum shifts to longer wavelength as a uniform electric field is applied [52]. Details about the Franz Keldysh effect in GeSi electroabsorpiton modulator are discussed in Chapter 5 with optimized composition and strain parameters for GeSi modulator arrays.

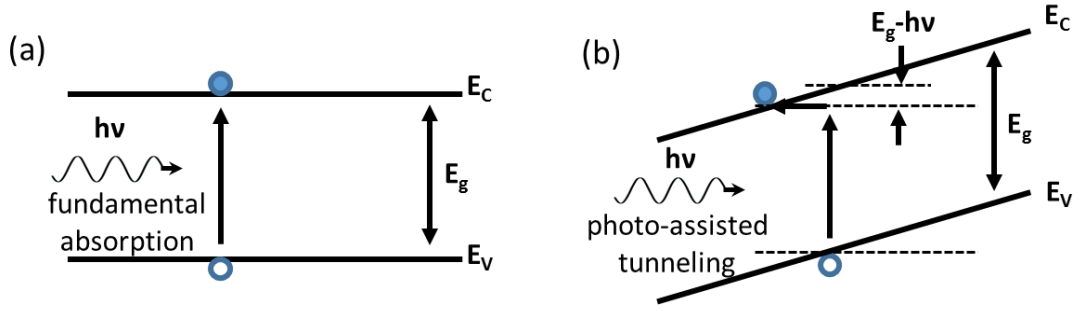

Figure 1.6 Photon absorption in (a) equilibrium state, (b) Franz-Keldysh effect with the titling of energy bands in a uniform electric field

Electroabsorption modulators offer lower energy consumption than phase modulators. The electroabsorption modulators operate through turning the material from transparent to opaque at the working wavelength regime via an applied electric field. The change in the absorption coefficient is typically in the order of 100–1000 cm^{-1}. That allows a compact device area with the

waveguide length in the order of 10–100 μm compared to the millimeter length scale for MZ modulators. This reduction in device footprint also reduces the capacitance of the devices, by which the modulator power consumption is reduced following the energy relationship as $(1/2)CV^2$. Electroabsorption modulation is a field-induced effect where the response time is less than a picosecond, and the bandwidth is only limited by RC delay [52]. The limitation of the electroabsorption effect is its reliance on direct gap transitions. While Ge has a direct bandgap of 0.8 eV, which is at 1550 nm wavelength. Although Ge is an indirect gap semiconductor, the energy difference between its direct gap at the Γ valley and the indirect gap at the L valleys is only 136 meV. In order to achieve optimal absorption contrast in the1550 nm wavelength region, or even extend to the entire C and L bands, the Ge can be alloyed with a small amount of Si to increase the direct bandgap. In 2007, the design with a small amount of Si inclusion (0.75%) into Ge was proposed by our group, MIT EMAT, led by Dr. Jifeng Liu and my advisors Dr. Jurgen Michel and Professor Lionel Kimerling. That marked as a milestone for low power high-speed GeSi electroabsorption modulation [3]. From then on, GeSi electro-absorption modulators have been actively researched and demonstrated by several research teams over the world. S.A. Srinivasan and his group at IMEC in Belgium have demonstrated Ge electroabsorption modulator with modulation rate up to 56 Gbit/s and low dynamic power consumption of 12.8 fJ/bit [52-61].

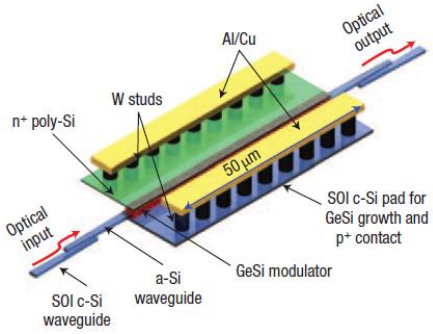

Figure 1.7 Schematic of the waveguide integrated $Ge_{0.9915}$ $Si_{0.0075}$ modulator [3].

1.4 GeSi modulator arrays for high-speed broadband modulation

As shown in Table 1.1 for the comparison of the figures of merits among the state of the art Si and Ge modulators, each type of modulators has its advantages and limitations. Si MZI modulators have shown excellent broadband modulation capability with relatively high insertion loss and low extinction ratio. It has been demonstrated for high-speed modulation in both 1300nm and 1550nm telecommunication bands. However, the dispersion effect on refractive index change for phase modulation generally requires a much longer device compared to the ring resonator-based phase modulators and electroabsorption modulators. Moreover, as the modulation speed is pushed to a higher RF domain, the millimeter long modulator is required with a complex design of traveling wave electrodes to avoid the extra RF attenuation due to the RF electrode effective index and optical mode effective index mismatch. Many research and design efforts have been investigated on this matter to further enhance the Si MZI phase modulation speed in both academics and industry. Si ring resonator-based modulators provide an excellent extinction ratio due to its resonance enhancement, along with the lower insertion loss, the lower power consumption, and smaller device size compared to Si MZI modulators. However, the major drawback of the Si ring resonator-based modulators is its wavelength selectivity and temperature sensitivity for its modulation. The resonance enhancement only works during the coupling condition between the ring and bus waveguide, which gives the ultra-narrow optical bandwidth of several nanometers or less. For the modulation to work at a specific wavelength, sophisticated thermal isolation and tuning strategy are needed. Advancement of the Si under-etching and trenches patterning has helped on improving the thermal stability of the ring resonator-based modulators [29]. As for electroabsorption modulators, they have small device footprint, high extinction ratio, low insertion loss, and low energy consumption, compared to Si MZI modulators. Although GeSi modulators have only shown its

functionality in the 1550 nm wavelength range, it is a promising modulator structure for high-speed and low power modulation. The optical bandwidth of the current GeSi electroabsorption modulators is about 20nm, which is limited by the nature of the Franz-Keldysh effect. The most considerable absorption coefficient change only occurs at the energy slightly less than the bandgap. The optical bandwidth of the electroabsorption modulator is about half or one-third of that in MZI modulators and two orders of magnitude larger than that in the ring resonator-based modulators.

As for the EPICs application in a telecommunication system, such as the one illustrated in Figure 1.2, there is a need for an array of modulators to cover various wavelength channels in order to expend the total data transfer rate. As a comparative example, if Si MZI modulators are used for the modulation array, no individual tuning of the Si materials property might be needed to cover the total modulation optical bandwidth of 100nm with four channels. However, that requires the modulators to be arranged in parallel, which requires the total array footprint of 12mm by 2 mm without considering the spaces reserved for electrical contact layout. That limits the device design and application into the large scale systems. The same system using Si ring-resonators-based modulator array demands the smallest device area of 0.04 mm by 0.04 mm. However, each channel of the ring resonator-based modulator requires excess processing steps and chip space for thermal insulation and thermal stabilization. The individual Si ring resonator-based modulators channel needs to be designed for its target wavelength in each channel. That adds a lot of design and processing costs for the system design and fabrication. The application of the GeSi electroabsorption modulator array provides a promising and balanced solution. It requires the total array area of 0.2 mm by 0.04 mm without the need for a complex thermal strategy. The usage of electroabsorption modulator array provides as large as 3000 times of area reduction, and one order of magnitude lower power consumption compared to the Si MZI modulator array. There is one

critical challenge for this electroabsorption modulator array approach. It is its narrow optical bandwidth, which means each modulator might need to be engineered and fabricated individually toward a specific wavelength in each channel. That will increase the total device fabrication cost and processing complexity. This thesis work is aimed to solve this challenge and make electroabsorption modulator array advantageous with simplified design and device layout, much smaller device area, and lower device power consumption for a high-speed broadband modulation in competing with Si MZI modulator array.

Table 1.1 Figures of merits summary of various modulators.

Modulator Type	Ref.	Footprint [um^2]	Wavelength [nm]	Voltage Swing [V]	Optical Bandwidth [nm]	ER [dB]	IL [dB]	Static Power [mW]	Dynamic Power [fJ/bit]	Bit Rate [Gb/s]
Si MZI	39	3000*500	1300	1.5	80	3.4	7.1	20	450	50
Si Ring	47	10*10	1550	0.5	0.1	6.4	1.2	0.01	1	44
IIIV on Si	5	100*350	1300	2.2	30	10	4.8	6.2	484	50
GeSi EAM	6	40*1.5	1566	4.0	40	5.2	10.6	11.3	44	56
Ge EAM	58	40*10	1615	2.0	22	4.6	4.9	1.2	12.8	56

Chapter 2 Epitaxial film growth of Ge with small Si alloy composition on Si-on-insulator substrate

The realization of the Ge and GeSi electroabsorption modulators requires a high-quality epitaxial film growth of Ge and Ge-rich GeSi on Si-on-insulator (SOI) substrates. This chapter describes the experimental results of the epitaxial film growth using ultrahigh vacuum chemical vapor deposition (UHVCVD) system along with the material characterizations, including strain, composition, dislocation density, and surface roughness evaluations.

2.1 Growth model of Ge and GeSi on Si epitaxy

The ultrahigh vacuum chemical vapor deposition of Ge and GeSi with reaction gases of SiH_4 and GeH_4 involves a series of kinetic reactions. The overall process can be expressed as:

$$SiH_4(g) \rightarrow 2H_2(g) + \underline{Si} \quad \text{Eq. 2.1}$$

$$GeH_4(g) \rightarrow 2H_2(g) + \underline{Ge} \quad \text{Eq. 2.2}$$

The initial step is the adsorption of Si or Ge molecules and their decomposition into SiH_3 or GeH_3 and H molecules [62-63]. The adsorption reaction for each Si or Ge molecule requires two free surface sites. $\underline{Si}H_3$, $\underline{Ge}H_3$, and $\underline{H}$ represent gas species attached to surface sites. Free surface sites available for the adsorption reactions are represented by _. The free sites are released when the H_2 gas molecules desorb from the surface in the following reactions [63]. Since the adsorption reactions can only happen on the free sites, the H_2 desorption becomes a limiting factor for the growth rate.

$$SiH_4(g) + 2\_ \rightarrow \underline{Si}H_3 + \underline{H} \quad \text{Eq. 2.3}$$

$$GeH_4(g) + 2\_ \rightarrow \underline{Ge}H_3 + \underline{H} \quad \text{Eq. 2.4}$$

$$2\underline{H} \rightarrow H_2(g) + 2\_ \quad \text{Eq. 2.5}$$

Ge and GeSi heteroepitaxial growth has been a significant and popular technology for the Ge and GeSi integration on Si CMOS platforms. The deposition provides a unique opportunity to engineer a band structure with improved device performance. The structural similarity in Si and Ge allows miscibility in GeSi alloys and provides solid solutions over the entire composition range. The Si composition is precisely controlled in the growth. Si inclusion is varied from 0% to 3%. Challenge in the heteroepitaxial deposition of Ge films on Si substrates comes from the ~4% crystal lattice mismatch, which introduces film strain and dislocations. As the epitaxial film grows beyond a critical thickness of several nanometers, the strain energy in the film is relaxed elastically or plastically [64-66]. The strain causes surface corrugation while keeping coherent films. Misfit dislocations are introduced to relieve the strain energy of an elastically strained layer. Since the dislocations cannot end within the crystal network, they must terminate on the edge or surface boundaries of the films or close upon themselves by forming a misfit loop [67]. Some misfit dislocations propagate along (111) planes to the film surface; these dislocations are threading dislocations. The threading dislocations introduce the midgap states that reduce carrier lifetime and are detrimental to the electronic device performance. Therefore, monitoring and reducing threading dislocation density becomes a significant task in Ge and GeSi epitaxial film growth for the electroabsorption modulator applications.

The chemical vapor deposition technique of Ge and GeSi epitaxial layers on Si substrates has been researched and developed in recent decades to reduce dislocation density [66-69] There are two different approaches. One is the deposition of GeSi grated buffer layers to

achieve high-quality epitaxial films on Si substrates gradually [66]. The graded buffers are deposited at high temperatures, causing a fully relaxed buffer surface and accommodating strain relieved by existing misfit dislocations. In this approach, the nucleation of new dislocation is suppressed. It has been discovered that the dislocations can glide very fast at a high temperature of 750C to 850C, which allows effective removal of dislocations via cyclic annealing. In terms of composition, it was reported in the literature that above 50% of Ge composition, the strain introduces surface undulation and cause surface roughness. The chemical-mechanical-polisher (CMP) process is needed to flatten the surface and to resume the film growth. The lowest threading dislocation density reported was 2.lx $l0^6$ cm^{-2}. The graded buffer layer is generally a thick layer that requires a slow composition gradient from the substrate to the target film composition [68]. That poses challenges for Si CMOS electronic and photonic components integration due to the strict design and processing rules on the various layer thickness.

Another heteroepitaxial growth technique is the two-step deposition technique using the low-temperature constant composition buffer layer. The buffer layer with composition matched to the films is deposited at a low temperature of 350ºC. Despite a large lattice mismatch between Ge and Si, the buffer deposited at this temperature is planar due to the limited surface-diffusion, which prevents surface islanding [65]. The remainders of the films are deposited at a high temperature of 750C, followed by thermal cyclic annealing [67]. Upon cooling, tensile strain is accumulated in Ge films since the expansion coefficient of Ge is larger than that of Si. This thermally induced strain, especially during the thermal cyclic annealing process, produces the dislocation gliding along with dislocation annihilation and a reduction in dislocation density. The as-grown Ge or GeSi film, therefore, preserves a tensile strain due to the

thermal expanse coefficient difference between the film and substrate at a fully relaxed high annealing temperature when cooled down to room temperature for further processing. The reported value for the dislocation density is in the order of $2x10^{7}cm^{-2}$. Compared to the graded buffer approach, this two-step growth method only relies on the lower temperature buffer layer thickness in the order of sub-hundred nanometers. That makes it a promising approach for high-quality Ge and GeSi integration on the Si CMOS foundry process.

2.1 Experimental results of Ge and GeSi epitaxial film on Si-on-insulator substrate

In this thesis work, the two-step growth approach is used to grow high-quality Ge and GeSi films epitaxially. The Ge and Ge-rich GeSi heteroepitaxy deposition growths were conducted in the UHVCVD system. Prior to loading the wafers into the UHV-CVD reactor, the wafers were surface cleaned via the RCA process (organic and ionic cleaning). The wafers were then carefully dipped in the dilute HF solution ($HF:H_20=1:50$) for 30 seconds to passivate the substrate surface with hydrogen. The wafers were loaded into the UHV-CVD system. 100% germane (GeH_4) gas was used as a reactive source to deposit the buffer layer at 350°C. Then, the temperature was ramped to 730 ^oC for high-quality Ge epitaxial film growth at a controlled growth rate of 6 nm/min. The film was cyclically annealed between 600C and 850^oC. The total reactive gas flow was kept constant at ten sccm. The processing pressure was maintained to be 15 mTorr. The deposition of Ge-rich GeSi takes into account of reaction kinetics of both Ge and Si growth at a controlled germane and silane (SiH_4) gas flow rates.

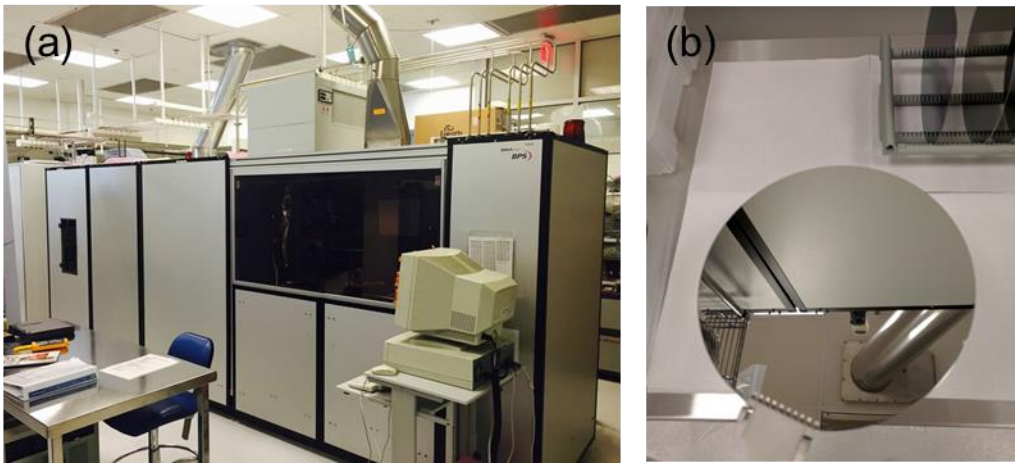

Figure 2.1 (a) Ultra-high vacuum chemical vapor deposition (UHV-CVD) system; (b) GeSi epitaxial film grown on a SOI wafer.

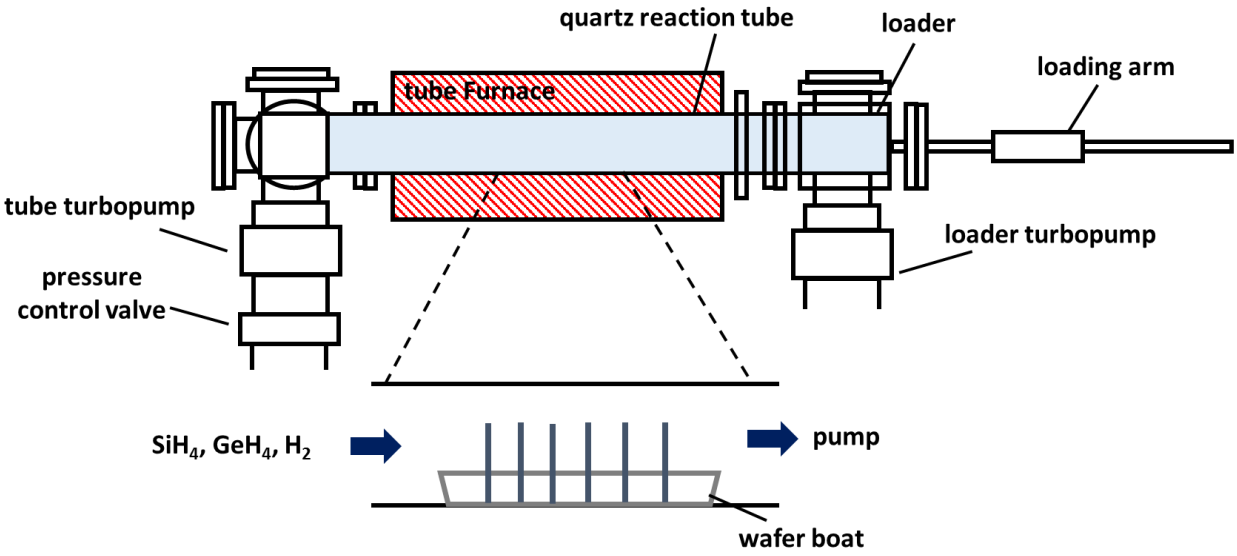

Figure 2.2 Tool layout of the UHV-CVD system.

2.2.1 Film surface uniformity characterization in AFM

In the two-step heteroepitaxial deposition technique, the buffer layer is critical for the film quality. If the buffer layer is too thin, the planar buffer layer will not be formed, which leads to the

unsuccessful growth of high-quality Ge film. If the buffer layer is thick, it becomes the source of increased threading dislocation density, which suppresses the epitaxial film quality. In the electroabsorption modulator, the Ge waveguide has a height of 300nm. It becomes essential to optimize buffer layer thickness. A series of Ge epitaxial film deposition with various buffer layer thickness and the same total film thickness of 300nm has been conducted. The optical profilometer was used to evaluate the surface roughness of the films. The one micrometer Ge heteroepitaxial layer with a buffer layer thickness of 100nm was also prepared and compared with the thin 300 nm Ge and GeSi heteroepitaxial layers. As shown in Table 2.1, the surface roughness increases dramatically as the buffer layer thickness is reduced from 40 nm to 20 nm. That indicates the buffer layer threshold of 40 nm for high-quality film growth. The average surface roughness gradually improves from 1.18 nm to 0.98 nm as the buffer layer increases from 40 nm to 80 nm. The trade-off of the thick buffer layer is the increased threading dislocation density, which might degrade the electroabsorption modulator performance. This evaluation indicates that the Ge buffer layer thickness can be lowered to 40 nm, maintaining the smooth film surface. The $Ge_{0.99}Si_{0.01}$ and $Ge_{0.97}Si_{0.03}$ films with a total thickness of 300nm and buffer layer thickness of 40 nm were grown with a good surface quality.

Table 2.1 Surface roughness evaluation of Ge or GeSi heteroepitaxial films on Si substrate.

	300 nm Ge				300 nm $Ge_{0.99}Si_{0.01}$	300 nm $Ge_{0.97}Si_{0.03}$	1 µm Ge
Buffer Layer (nm)	20	40	60	80	40	40	100
Average Roughness (nm)	9.73	1.18	1.02	0.98	1.21	1.23	0.75
Root Mean Square Roughness (nm)	12.20	1.44	1.28	1.19	1.45	1.51	0.94

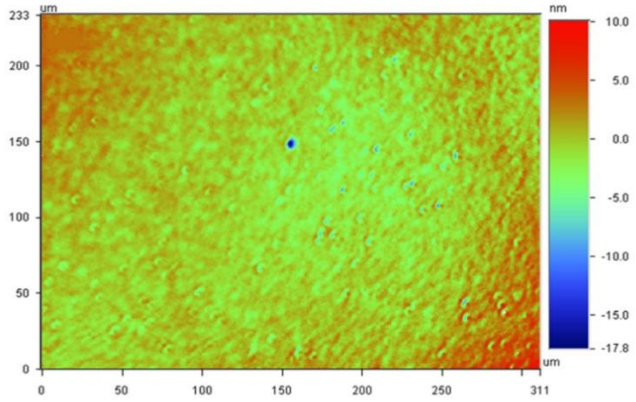

Figure 2.3 Surface roughness evaluation of the 300nm Ge-on-Si epitaxial film at a planar view.

2.2.2 Threading dislocation density evaluation in Etch Pit Density (EPD) and Transmission Electron Microscope (TEM)

The measurement of etch pit density has been developed to evaluate the film quality. The basic principle for the selective etching on the threading dislocation sites is that the strain field created by dislocations distorts the atomic bonds in the crystal lattice, and increases the potential energy of the chemical bonds [71-73]. This increase in potential energy lowers the activation energy for etching reactions. That causes the etch rates to increase in the vicinity of the location where a dislocation terminates at an exposed surface. By placing the samples in a GeSi etching solution, the film is more quickly etched at the dislocation sites, which forms etch pits. Etch pits

are visible in the optical microscope allowing for the analysis of large sample areas. An etching solution is a chemical mixture of 20% HNO_3, 10% HF, and 70% CH_3COOH with 0.3 g/L dissolved iodine [73]. Etching time in the solution is typically between 2 and 3 seconds, followed by the deionized water rinse. As shown on the microscopic images in Figure 2.4, the etch pits are distinctive. An automatic pits identification and counting method has been developed using image analysis software to efficiently obtain the statistics of the etch pit density. As illustrated in Figure 2.4, the original image is converted to binary black and white image. Adjusting the color threshold reduces the noise. Pits are identified, labeled, and counted by defining the element size and circularity. During the pits identification, the overlapping of the elements is successfully separated and identified by adjusting circularity and size range. The threading dislocation density per unit area is obtained to be $2x10^7$ cm^{-2} from the EPD evaluation.

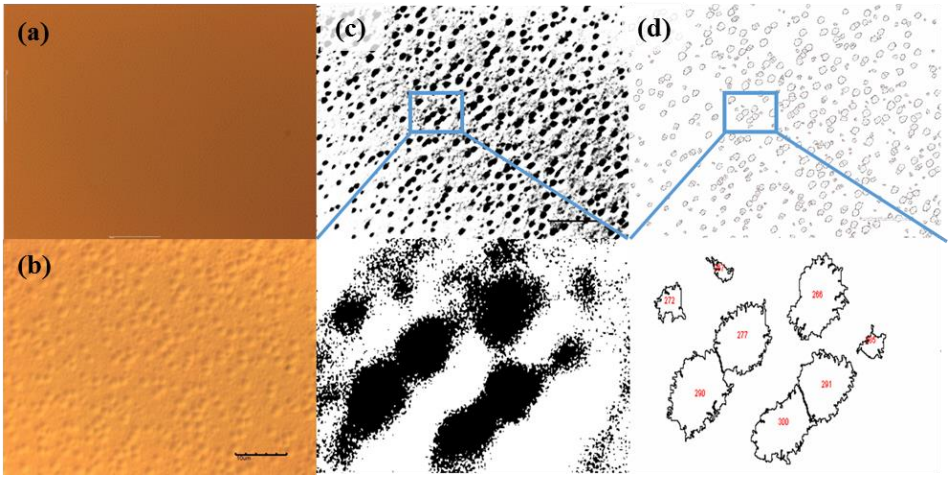

Figure 2.4 Optical microscope top surface image of the (a) Ge film, (b) Ge film after selective dislocation etching; (c) binary processed image (b), and (d) automatic etch pits identification and labeling via image analysis.

Besides etch pit density evaluation, a planar view transmission electron microscope is used to observe and count the threading dislocation density. Both the misfit and threading dislocations are visible on planar TEM images, as shown in Figure 2.5. Through statistically count tens of TEM images, the threading dislocations per unit area were determined to be $4x10^7$ cm^{-2}. It is close to the result of the etch pit density evaluation. In general, there is a little overestimation from the TEM method compared to the density value obtained from the EPD analysis. It is because the TEM analysis has a small field of view, which tends to capture none or couple threading dislocations per field of view. The TEM imaging, hence, tends to focus on the locations with the presence of dislocations and subconsciously reduce the imaging probabilities of the area without dislocations. The cross-check of those two approaches demonstrated high-quality Ge films.

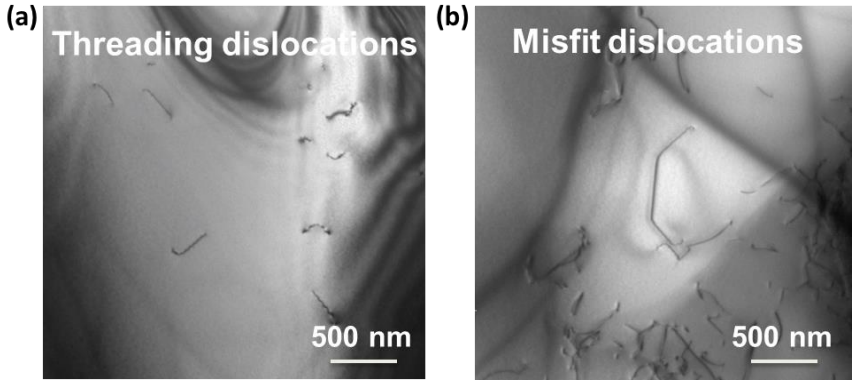

Figure 2.5 Planar TEM images of (a) threading and (b) misfit dislocations for the Ge epitaxial film on an SOI substrate on (001) plane.

2.2.3 Film strain characterization in XRD

The strain of the Ge and GeSi films is characterized via X-Ray Diffraction techniques. The Ge (004) peak position in 2Θ XRD step scans is measured and calculated into the lattice spacing *d* of (004) planes. The spacing and the strain is related as a follow [74]:

$$d_{004} = \frac{1}{4}(1 + \varepsilon_{\perp}{}^{004})a_{GeSi} \qquad \text{Eq. 2.6}$$

Where *a* represents bulk Ge lattice constant. Under biaxial stress, the in-plane strain $\varepsilon_{||}$ in cubic structure is related to the out-of-plane strain as following:

$$\varepsilon_{||} = -\frac{2C_{11}}{C_{12}}\varepsilon_{\perp} \qquad \text{Eq. 2.7}$$

The in-plane strain and the out-of-plane strain are then obtained from the XRD data. The elastic moduli parameters C_{11} and C_{12} are applied with the correlation to the Si composition x, as $C_{11} = 128.53 + 37.27x$ and $C_{12} = 48.26 + 15.62x$ [75]. In the epitaxial growth, the tensile strain is accumulated in the Ge and GeSi films due to the large thermal expansion coefficient of SiGe films compared to the SOI substrates. This is the thermally-induced strain in SiGe films that can be simulated by considering the thermal expansion coefficients. The strain simulation on both Ge and GeSi films and waveguide structures is discussed in detail in Chapter 4. The small Si inclusion does not provide enough composition information through XRD. All 500nm Ge, $Ge_{0.99}Si_{0.01}$, and $Ge_{0.97}Si_{0.03}$ films strain measured from XRD shows the biaxial tensile strain of 0.198%.

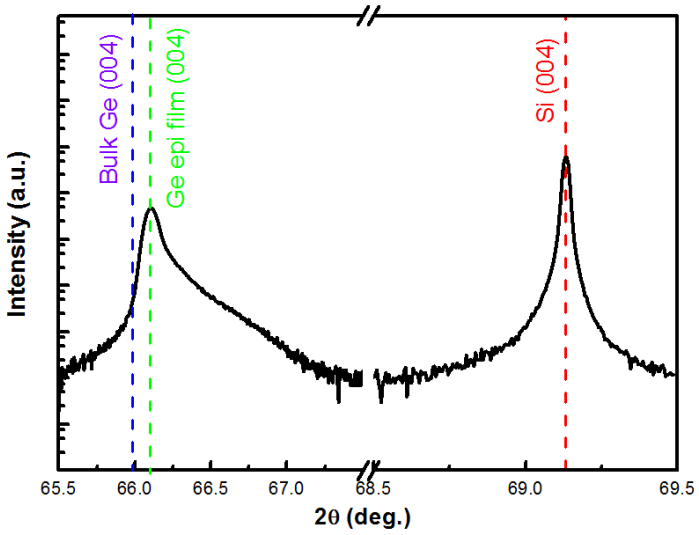

Figure 2.6 XRD spectrum of bulk Ge and Ge epitaxial film on a Si substrate.

2.2.4 Composition and strain characterization in photoreflectance spectra

For those 500nm thick Ge and GeSi epi film on SOI substrate grown at 730 ^{0}C and annealed at 850 ^{0}C, the photoreflectance (PR) measurements are performed to correlate the composition and strain information with band structure in Ge and GeSi films. The PR measurements were done together with Professor Sabina Merlo during her visit at MIT in 2016. Professor Sabina Merlo's contribution and dedicated patience in aligning the optics allowed the successful PR measurements, which is sincerely appreciated.

The XRD measurement discussed in the previous section gets a probed depth of the whole Ge and GeSi epitaxial film thickness. As for the PR measurement, the probed depth is based on the carrier diffusion length, expressed as,

$$L = \sqrt{D\tau} \qquad \text{Eq. 2.8}$$

Where D is the diffusivity of minority carrier (holes in this case) in Ge, (D_{Ge} is about 100 cm^2/sec); τ is the minority carrier lifetime with threading dislocation density in the order of ~$2x10^7$ cm^{-2} in correspondence to the threading dislocation density measured in the EPD and TEM (τ_{Ge} is about 0.02ns). Hence the probed depth in PR is ~450nm, which is about the epitaxial film thickness of all the measured Ge and GeSi films. The strain value applied in the PR measurement and bandgap derivation is, therefore, consistent with the XRD measured strain value. This consistency of the strain is critical for deriving the precise composition values of GeSi films in the PR measurements because the PR peaks, as shown in the following figure, are the resultant peaks due to both strain and composition contributions in the GeSi films.

Photoreflectance measurement is applied to determine the direct bandgap of the Ge and GeSi films. Figure 2.7 shows the layout for the photoreflectance measurement. A 532nm wavelength laser is used as the pump laser source. It is modulated at a frequency of 201Hz by a chopper to achieve electric field modulation on the sample surface by injecting carriers into the Ge or GeSi films. A halogen lamp with a scanning monochrometer is used as the light source for reflectance measurements, as illustrated in Figure 2.8. Due to the modulation of the pump laser, the reflectance of the Ge film at wavelengths near its direct band edge can be modulated, which is a similar mechanism of Franz-Kelydsh effect in electroabsorption measurement but used for reflectance measurements with pump laser injection. The initial electric field of about 10 kV/cm is built in the epitaxial film due to the requirement of equalizing the Fermi level between intrinsic Ge and p+ Si substrate. When the pump laser is shone on the film surface, it generates electrons and holes, which drift under the built-in electric field in a way to weaken the built-in electric field. This change in the electric field can be observed in terms of the difference in the measured

reflectance. A photodetector collects the reflected signal and feeds electrical signals into a multimeter and a lock-in amplifier. The multimeter measures the average reflectance, R, between pump on and pump off state. The synchronized lock-in amplifier captures the difference in the reflectance, ΔR, due to the pump laser injection. By monitoring the relative change in reflectance ΔR/R versus wavelength near the direct band edge of Ge or GeSi, the information on the material direct bandgap is captured, which indicates the operation wavelength range of the electroabsorption modulator.

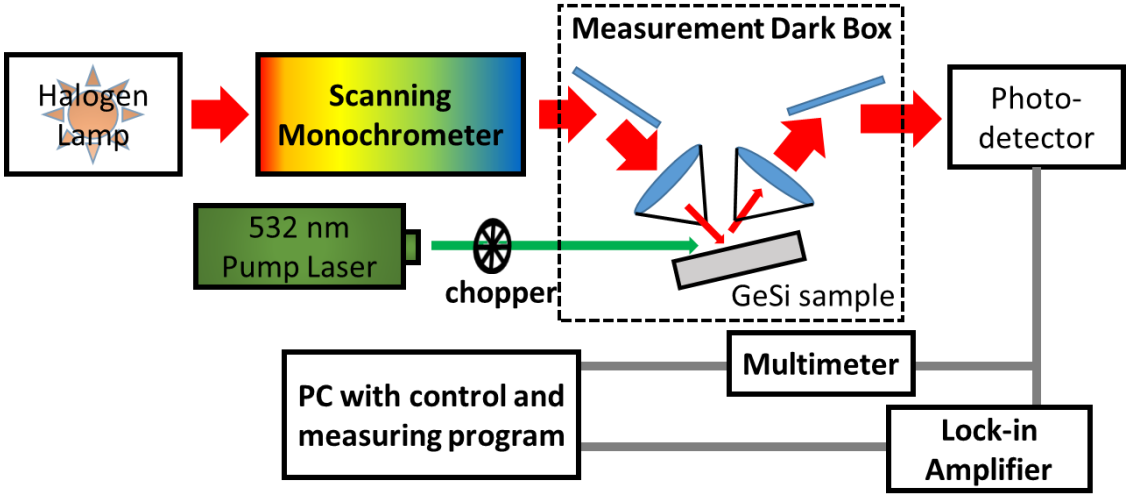

Figure 2.7 Schematic of the photoreflectance measurement.

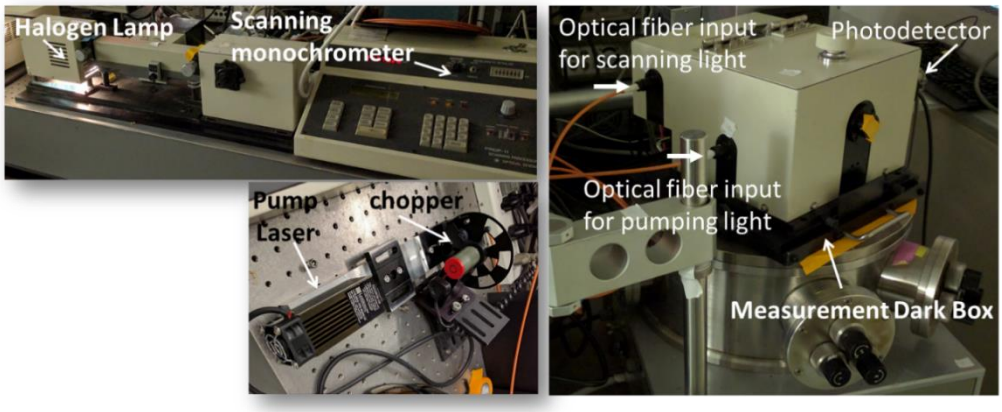

Figure 2.8. Optical images of the components in the photoreflectance measurement stage.

The systematic study of the Ge epitaxial growth at various temperatures with its PR spectrum has been reported by Dr. Liu at EMAT in 2004 [76]. It is observed that the presence of the tensile strain the Ge epitaxial film caused the non-degeneracy of the light hole and heavy hole valence bands. Both the strain and composition in the film cause the light hole and heavy hole bandgap peaks to shift. The PR spectrum of Ge and Ge with 1% Si film show sharp and distinct PR peaks in Figure 2.9. The Fourier Transfer Filter (FFT) is applied to suppress the instrumental noise.

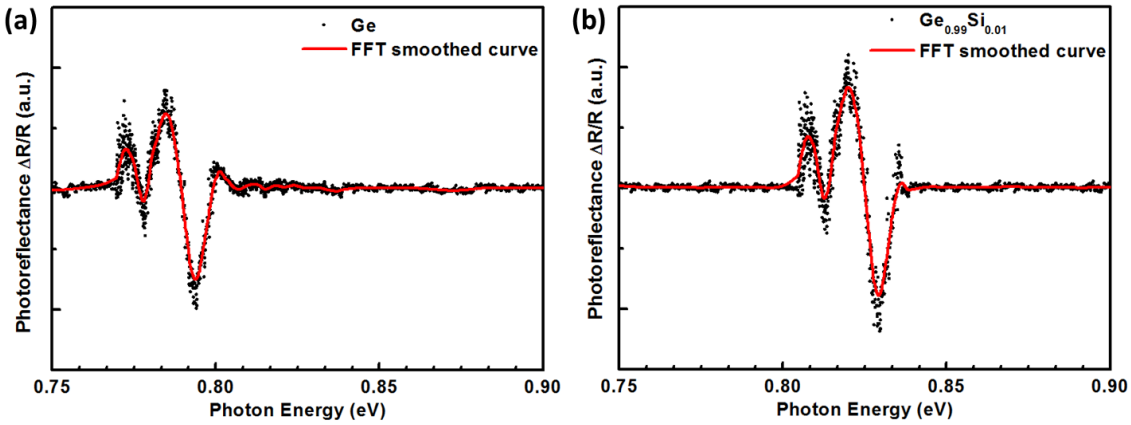

Figure 2.9 Photoreflectance measurements of (a) Ge and (b) $Ge_{0.99}Si_{0.01}$ films.

The measured PR data for Ge and GeSi epitaxial films are fitted via the generalized Franz-Keldysh equations, as developed in the literature for the fundamental direct bandgap transition [77-78]. The PR signal is proportional to the change in the real part of the dielectric constant under the electric field.

$$\frac{\Delta R}{R} \propto Re(\delta\varepsilon) \qquad \text{Eq. 2.9}$$

$$\delta\varepsilon(\hbar\omega, F_{dc}, F_{ac}) = \Delta\varepsilon(\hbar\omega, F_{\mathrm{dc}}) - \Delta\varepsilon(\hbar\omega, F_{\mathrm{dc}} - F_{ac}) \quad \text{Eq. 2.10}$$

Where $\hbar\omega$ is the incident photon energy, F_{dc} is the built-in electric field in the Ge or GeSi epitaxial film grown on Si substrate without pumped laser illumination, and F_{ac} is the pump laser-induced electric field. For the Ge or GeSi epitaxial film grown on Si substrate at a high temperature. The thermal expansion coefficient difference generates biaxial tensile stress in the film. That makes the light hole and heavy hole valence bands non-degenerate and causes separate band transitions for light holes and heavy holes. Hence, the total dielectric function becomes the sum of both light hole and heavy hole transitional contributions, as expressed following

$$\Delta\varepsilon(\hbar\omega, F) = \left(\frac{1}{\hbar\omega}\right)^2 \{B_{lh}(\hbar\theta_{lh})^{1/2}[G(\eta_{lh}) + iF(\eta_{lh})] + B_{hh}(\hbar\theta_{hh})^{1/2}[G(\eta_{hh}) + iF(\eta_{hh})]\} \quad \text{Eq. 2.11}$$

where B_{lh} and B_{hh} are light hole transition constant and heavy hole transition constant. The $G(\eta)$ and $F(\eta)$ are electro-optic functions, which are defined as

$$G(\eta) = \pi[Ai'(\eta)Bi'(\eta) - \eta Ai(\eta)Bi(\eta)] + \eta^{1/2}H(\eta) \quad \text{Eq. 2.12}$$

$$F(\eta) = \pi[Ai'^2(\eta) - \eta Ai^2(\eta)] - (-\eta)^{\frac{1}{2}}H(-\eta) \quad \text{Eq. 2.13}$$

$$\eta_{lh} = \left[E_g^{\Gamma}(lh) - \hbar\omega - i\gamma_{lh}\right]/\hbar\theta_{lh} \quad \text{Eq. 2.14}$$

$$\eta_{hh} = \left[E_g^{\Gamma}(hh) - \hbar\omega - i\gamma_{hh}\right]/\hbar\theta_{hh} \quad \text{Eq. 2.15}$$

Where $H(\eta)$ is the unit step function, Ai, Bi, Ai', and Bi' are the Airy functions and their derivatives. The γ_{lh} and γ_{hh} are the broadening factors for light hole and heavy hole band

transitions. The electro-optical energies for these light hole and heavy hole band transitions are expressed as,

$$\hbar\theta_{lh} = (e^2\hbar^2F^2/2m_{r,lh})^{1/3} \quad \text{Eq. 2.16}$$

$$\hbar\theta_{hh} = (e^2\hbar^2F^2/2m_{r,hh})^{1/3} \quad \text{Eq. 2.17}$$

Where e is the electron charge, and $m_{r,lh}$ and $m_{r,hh}$ are the reduced effective mass of electron-hole pairs of light and heavy holes, respectively [77]. The $\hbar\theta_{lh}$ and $\hbar\theta_{hh}$ are related to the assisted energy for the tunneling under the electric field. The higher the electric field, the higher this electro-optical energy, and the easier the tunneling process occurs. The terms η_{lh} and η_{hh} describes the characteristic of the potential barrier in the light hole and heavy hole band transitions under the electric field. Functions $G(\eta)$ and $G(\eta)$ are the mathematical solutions for this electric field-induced tunneling process. As shown in Figure 2.10, both the Ge and GeSi PR spectrum are fitted using the generalized FK model with the peak positions well fitted. The broadening factors are optimized to achieve the best fitting outcomes. The light hole and heavy hole bandgap information is derived and further analyzed to obtain the strain and composition information of the Ge and GeSi epitaxial films.

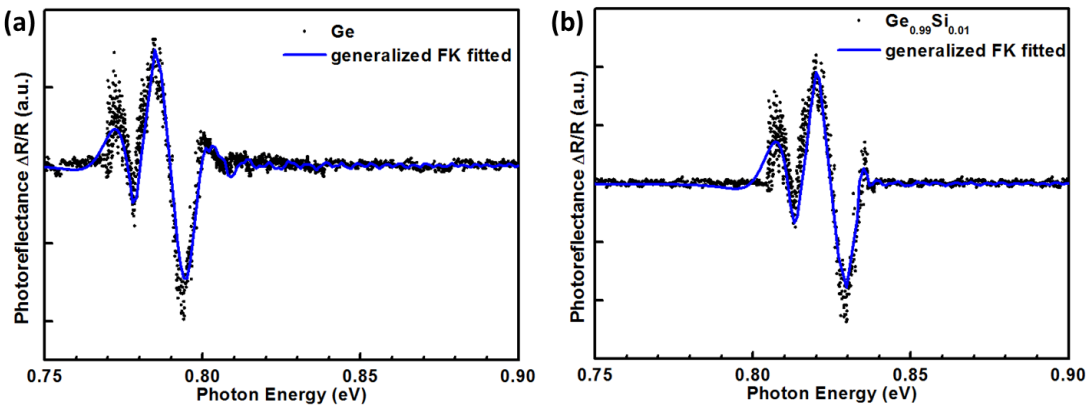

Figure 2.10 Measured and Simulated photoreflectance data of (a) Ge and (b) $Ge_{0.99}Si_{0.01}$ films on the SOI substrates.

The PR spectra for 500nm thick Ge on SOI wafer is fitted using the generalized Franz-Keldysh formula and obtained the light hole bandgap at 0.772 eV, and heavy hole bandgap at 0.785 eV. The peaks fitted for 500nm thick Ge with expected 1% Si inclusion on SOI wafer were at 0.807 eV for light hole bandgap, and 0.820 eV for heavy hole bandgap. The deformation potential theory is used to derive the GeSi epitaxial film composition coupled with the film strain information. The biaxial strain of the films is 0.198% tensile in all Ge and GeSi epitaxial films on the SOI substrate as determined in XRD measurements. The relationship between the biaxial film strain, and light hole and heavy hole bandgaps is expressed as:

$$E_{g,lh} = E_g(0) + a\left(\varepsilon_\perp + 2\varepsilon_{||}\right) + \frac{\Delta_0}{2} - \frac{1}{4}\delta E_{100} - \frac{1}{2}\sqrt{\Delta_0^2 + \Delta_0\delta E_{100} + \frac{9}{4}(E_{100})^2} \quad \text{Eq. 2.18}$$

$$E_{g,hh} = E_g(0) + a\left(\varepsilon_\perp + 2\varepsilon_{||}\right) + \frac{1}{2}\delta E_{100} \quad \text{Eq. 2.19}$$

$$\delta E_{100} = 2b\left(\varepsilon_\perp - \varepsilon_{||}\right) \quad \text{Eq. 2.20}$$

where $E_{g,lh}$ and $E_{g,hh}$ are the band gaps from the maxima of the light hole and heavy hole valence bands to the bottom of gamma valley under an in-plane strain. The deformation potential theory applied here only considers the direct bandgap of the Ge and GeSi material, as it is the most relevant bandgap for electroabsorption modulators. E_g is the bandgap of unstrained bulk Ge at room temperature; a and b are deformation potential constants of [001] Ge at room temperature. Δ_0 is the split-off band energy. For the Ge with a small amount of Si inclusion, the deformation potential constants can be linearly interpolated between Si and Ge. The Si inclusion fraction is x.

The deformation potential constants are a=-8.97+3.87x; b=-1.88-0.32x; Δ_0 =0.29 – 0.246x. For the Ge film with the biaxial tensile strain of 0.198%, the $E_g(0)$ is fitted to be 0.8eV, which is consistent with the bulk strain-free Ge direct bandgap. As for the Ge with expected 1% Si inclusion under the biaxial tensile strain of 0.198%, the Si fraction x value is fitted to be 1.1%, which is close to the expected composition, within the measurement precision. Although the sample of Ge with an expected 3% Si inclusion did not provide distinct peaks due to the large relative noise and low signal to noise ratio. The composition of Si is linearly extracted to be ~3.3% based on the Germaine and Silane reactive gas flow ratio applied for pure Ge and Ge with 1.1% Si epitaxial film growth. The correlation of direct light hole and heavy hole bandgaps as a function of Si inclusion is plotted in Figure 2.11. Therefore, the PR measurements prove the biaxial strain and Si alloying composition of the GeSi epitaxial films for the application in GeSi electroabsorption arrays. The electroabsorption modulators are designed and fabricated based on the 300nm epitaxial film of Ge or $Ge_{0.99}Si_{0.01}$ on 250nm on a 3um buried oxide structure.

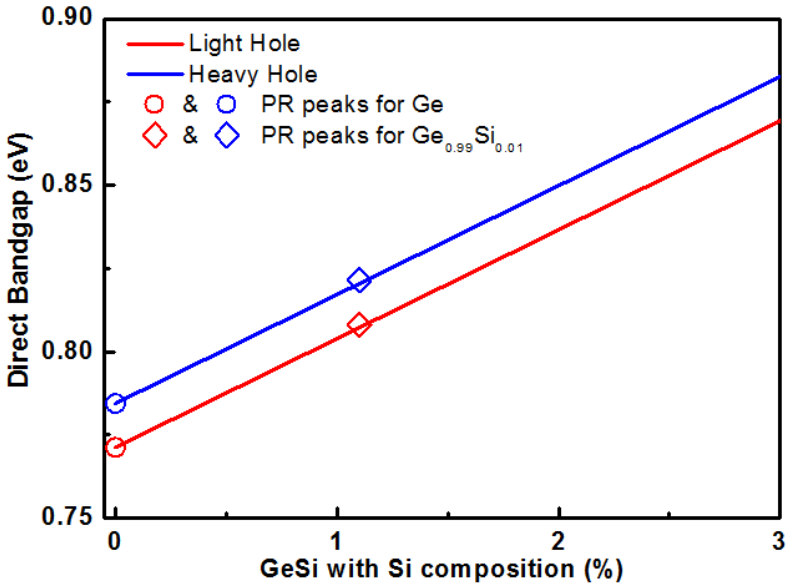

Figure 2.11 GeSi direct light hole and heavy hole bandgap as a function of Si composition.

Chapter 3 Waveguide integrated GeSi electroabsorption modulator design

The electron-photonic integrated circuits systems require the integration of passive components, such as waveguides and ring resonators, with active components including lasers, modulators, and photodetectors on a single chip. In this chapter, the design of Ge and GeSi electroabsorption modulators with Si waveguides integration is discussed. The two significant design challenges to be resolved are (1) optical coupling between the Si ridge waveguide and the waveguide modulator, (2) electrical contacts to apply a uniform electric field across the waveguide modulator. The design of the stressor layer for strained Ge and GeSi modulator array is introduced and discussed in Chapter 4.

3.1 Modulator waveguide optical coupling design

The modulator waveguide coupling design contains three optical parts, as shown in Figure 3.1. The Ge waveguide is on top of the Si ridge waveguide with Ge optical tapers on both ends of the waveguide modulator for the light coupling in and out of the waveguide modulator. The electroabsorption optical modulation occurs in the Ge or GeSi waveguide. The width and height of Si waveguide are 450nm and 250nm, respectively. The waveguide dimensions are set to be 350 nm wide and 300 nm tall for the initial simulation. The actual Ge modulator waveguide is a unique design parameter to vary the modulator materials bandgap as a response of the external stressor layer. The modulator operation wavelength can be tuned based on the modulator waveguide design along with the applied stressor layer.

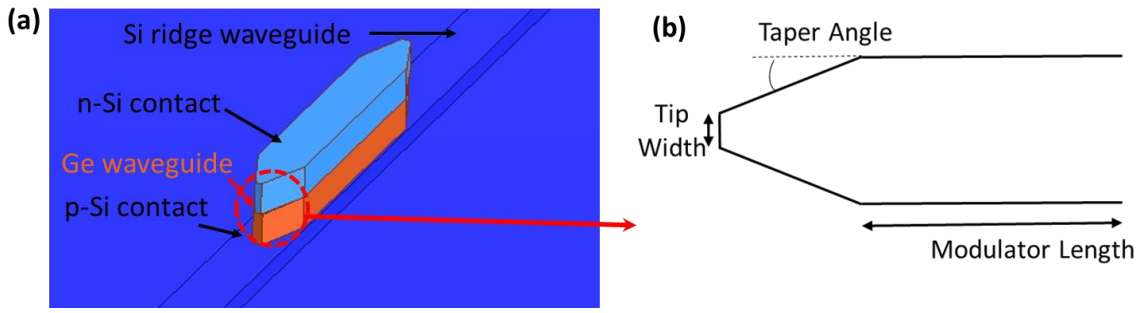

Figure 3.1 (a) Schematic of the Ge electroabsorption waveguide modulator; (b) design specifics of the Ge taper.

The effect of the taper angle on the insertion loss of the modular has been evaluated in the three-dimensional finite-difference time-domain (FDTD) model. The setup of the initiate model was contributed by the visiting scholar Hao Tian in 2016. He investigated the effect of the taper dimensions on the light coupling in the waveguide modulator with the Si bus waveguide at the waveguide width of 400nm. Insertion loss is the major source of loss when the light signal is coupled from the Si waveguide to the waveguide modulator. The simulation result shows that the taper angle of 5 degrees or less ensures the low insertion loss of the modulator. The taper structure is critical for the light coupling in the electroabsorption modulator. Besides the evaluation of the taper angle design, the effect of taper tip width on the loss of the modulator is investigated. As the taper tip width increases, the butt coupling efficiency lowers at the interface between the Si waveguide and the beginning of the taper tip. That is due to the refractive index discontinuity between the Si waveguide and the introduction of the Ge waveguide. This coupling coefficient can be improved by reducing the taper tip width. As shown in Figure 3.2, the decrease of the taper tip width enhances the ER/IL value at various Ge modulator lengths. The extinction ratio calculated is based on the assumed electric field difference between 10kV/cm and 40kV/cm. The insertion loss is calculated based on the material's absorption only, without considering the waveguide

surface and sidewall roughness due to the fabrication resolution. Detailed analysis of the loss mechanisms is discussed in Chapter 7 with the measured transmission spectrum in waveguides with various dimensions. Ideally, the taper tip width approaching zero gives the smallest effective index disturbance and hence the best coupling performance. However, the lithography resolution was limited, and the best performance occurred at the taper tip width of 100nm based on the experimental results.

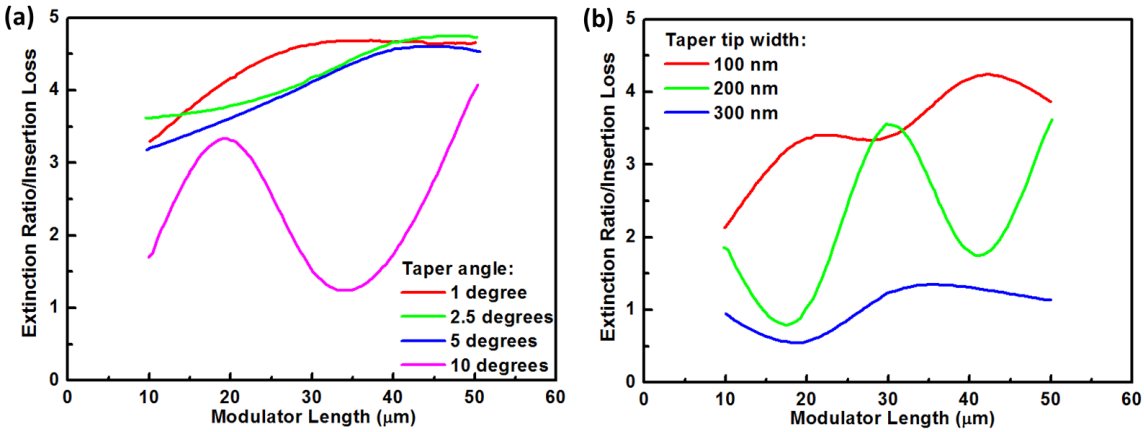

Figure 3.2 Extinction ratio/insertion loss evaluation of various (a) taper angles at the fixed taper tip width of 100nm and (b) taper tip width as a function of modulator waveguide length at a fixed taper angle of 5 degrees (courtesy of Hao Tian)

The influence of the shift of Ge waveguide position with respect to the underneath Si waveguide has also been investigated. The evaluation takes into account device fabrication tolerance. Since the device geometries are in the order of nanometers, it is important to know the tolerable fabrication error for the commercial CMOS processing flow. One challenging step in device fabrication is the alignment and etching of the Ge waveguide on top of the Si waveguide. The optical mode distribution and ER/IL evaluation indicate the tolerance of the horizontal shift of 30nm of Ge waveguide central position on top of the Si waveguide. There will be no distinctive

effects on the simulated modulator performance if the Ge waveguide is fabricated 30nm off from the central position of the underneath Si waveguide. The taper tip design is optimized to be 100 nm wide with the taping angle of 5 degrees. The coupling section with the tapers on both ends is designed accordingly in the masking, alignment, and patterning processing steps.

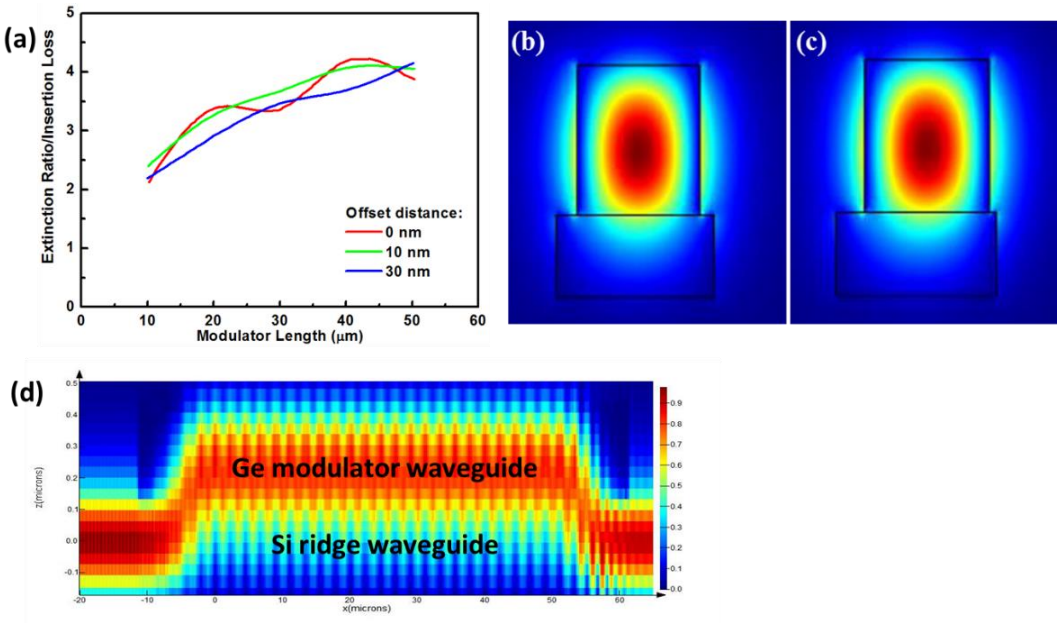

Figure 3.3 (a) Extinction ratio/insertion loss evaluation of various Ge waveguide position shifts on the top of the Si waveguide. Finite difference time domain optical mode simulation of the Ge waveguide (b) centered and (c) 30nm shifted to the left on top of the Si waveguide. (d) cross-sectional electric field intensity map for the light coupling from Si ridge waveguide to 400 nm wide Ge waveguide. (courtesy of Hao Tian for figures (a) through (c))

The width of the waveguide modulator increase leads to the increase in the insertion loss with a fixed taper tip width and taper angle, especially when the waveguide width increases over several micrometers wide. For wider modulators, the mode distribution variation in differently shaped waveguides cross-section; the direct taper might excite the higher-order mode and cause

extra propagation loss. The tapers for wider waveguide modulators (one micrometer to four micrometers wide) are designed with a two-step tapered coupling. The Si ridge waveguide for inter-component light coupling has a fixed dimension of 450nm wide and 250 nm tall with 80 nm unetched. At the first step of the coupling, the same taper design is used to couple the light into the 700 nm width modulator waveguide. Once the light is coupled into the modulator waveguide, the waveguide width is then gradually widened to the target width (one micrometer to four micrometers) in the second coupling step, as illustrated in Figure 3.4. The same approach is used to couple the light out from the modulator waveguide at the other end. The electric field intensity mapping on the center vertical plane is performed to investigate the light propagation efficiency for various modulator waveguides. Compared to the case of using the direct taper on a 4um wide modulator waveguide, as shown in Figure 3.4 (a) and (b), the application of a two-step taper significantly improves the coupling efficiency, as shown in Figure 3.4 (c) and (d). The transmission is enhanced from 20% to over 90% for the usage of a two-step taper on a 4um wide modulator waveguide. Then the various waveguide modulators are designed to have efficient light coupling and low insertion loss. The single-mode propagation is ensured in the design preventing the propagation loss due to higher-order mode excitation.

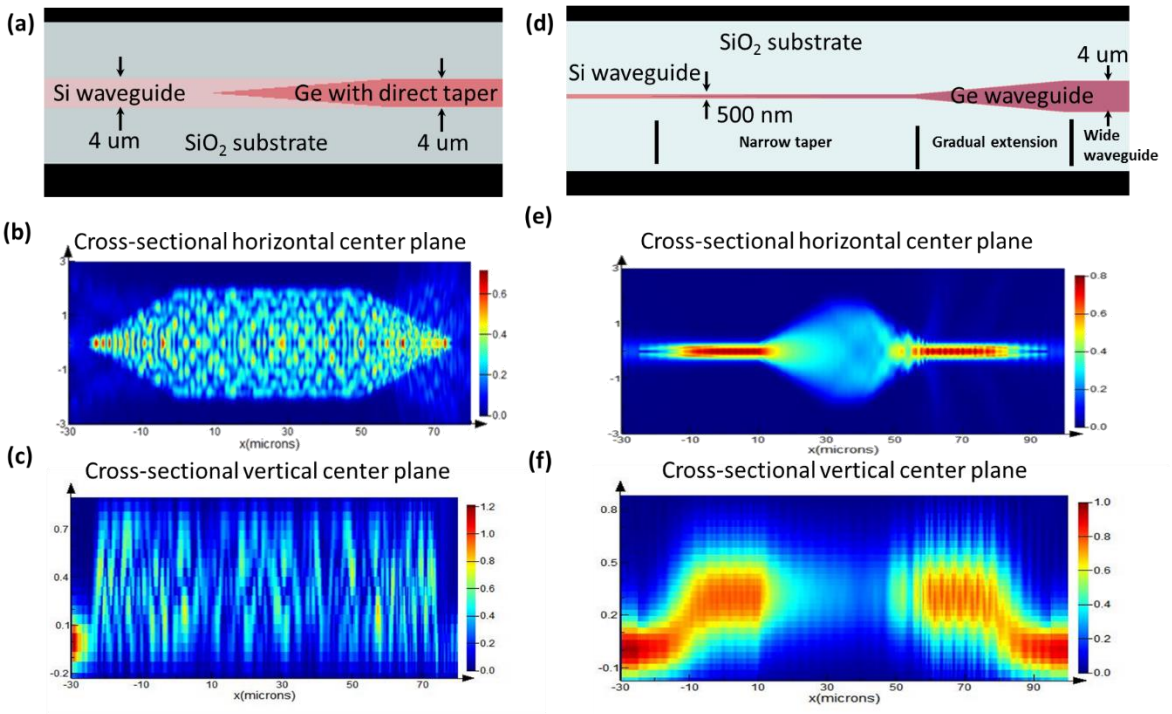

Figure 3.4 (a) schematic of the direct taper for a 4 um wide modulator waveguide with the cross-sectional electric field intensity mapping on the modulator waveguide (b) horizontal center plane and (c) vertical plane. (d) schematic of the two-step taper for a 4 um wide modulator waveguide with the cross-sectional electric field intensity mapping on the modulator waveguide (e) horizontal center plane and (f) vertical plane showing significant improvement on the light coupling.

3.2 Modulator electrical contacts design

Besides optical coupling design, the modulator electrical contacts design is critical to modulate the coupled light in the Ge or GeSi modulator waveguide region. The application of a high and uniform electrical field within a short transient time is the key for high speed and energy efficient electroabsorption modulators. The careful consideration is made on the Si contact layer formation in terms of doping levels and positions of the contacts, and the placement of the metal pads for the high-speed modulation.

3.2.1 Dopant implantation and diffusion model for top and bottom Si contacts

The top and bottom Si contact structures are designed to allow the accessible free facets on the sides of the waveguide modulators for the strain engineering. The details on the stressor placement and modulator strain engineering is the focus of Chapter 4. The technology CAD (TCAD) models are built using Synopsys Sentaurus workbench to optimize the doping procedures for both the bottom n-type Si and top p-type Si. The boron ion implantation is designed to be performed on patterned SOI wafers. As shown in Figure 3.5, the combination of boron implantation energy, tilt angle, shadow oxide thickness, ion dosage, and annealing temperatures is optimized to achieve the target active boron concentration of 10^{20} cm^{-3}. The actual implantation condition includes 100 nm shadow oxide layer, 7 degrees tilt, implantation energy of 60 keV, the dose of $2.5x10^{15}$ cm^{-2}, and the activation annealing temperature at 1000 ^{o}C for 30 minutes. The shadow oxide is removed after annealing by dipping in the buffered oxide etching solution for 3 minutes to ensure complete surface oxide removal. The four-point probe measurements are performed on all the wafers to confirm the expected doping level of 10^{20} cm^{-3}.

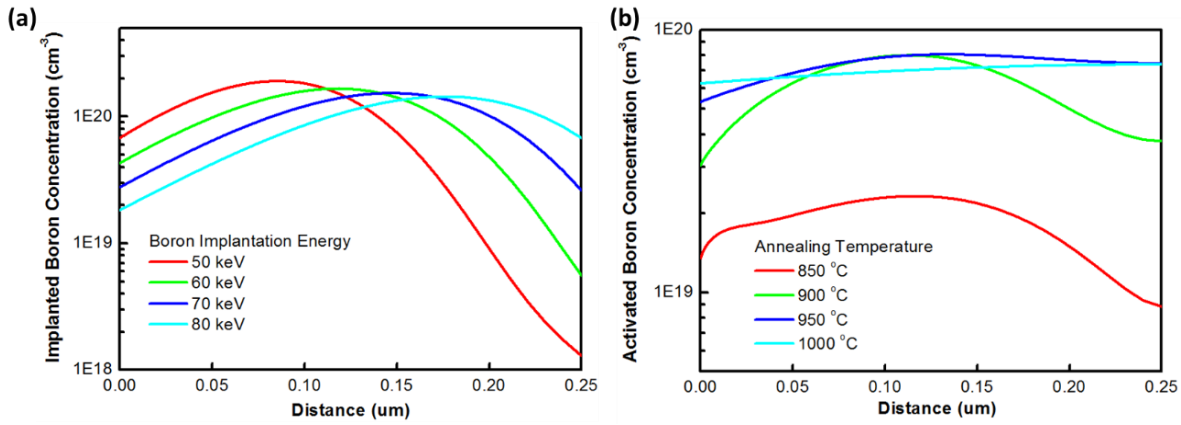

Figure 3.5 (a) Implanted boron concentration as a function of boron implantation energy with a top 100 nm shadow oxide. (b) Activated boron concentration as a function of annealing temperature

for the 30 minutes duration with 7 degrees tilt, the implantation energy of 60 keV, the dose of $2.5x10^{15}$ cm^{-2}, and 100 nm shadow oxide removed after annealing.

After the boron implantation, the wafers were cleaned in the RCA process and underwent the epitaxial growth of Ge or Ge with small Si inclusion in the UHVCVD system. The cyclic annealing was performed after Ge or GeSi epitaxial growth. The top Si layer was then grown in the UHVCVD system right after the cyclic annealing without breaking the vacuum of the environment to ensure the surface quality for top Si growth. The top Si layer was grown at 650 ºC for a thickness of 400nm. The top shadow oxide was deposited separately in a PECVD tool after the batch growth of top Si and GeSi epitaxial layers. The TCAD model is built to simulate and optimize the phosphorous ion implantation procedure taking into account the layered structures underneath epitaxial GeSi on the Si-on-oxide substrate. As illustrated in Figure 3.6, the combination of phosphorous implantation energy, tilt angle, shadow oxide thickness, ion dosage, and annealing temperatures is optimized to achieve the target active phosphorous concentration of 10^{20} cm^{-3}. The actual implantation condition included the shadow 100 nm oxide layer, 7 degrees tilt, implantation energy of 190 keV, the dose of $8x10^{15}$ cm^{-2}, and activation annealing temperature at 650C for 30 minutes. The shadow oxide is removed after annealing by dipping in the buffered oxide etching solution for 3 minutes to ensure complete surface oxide removal.

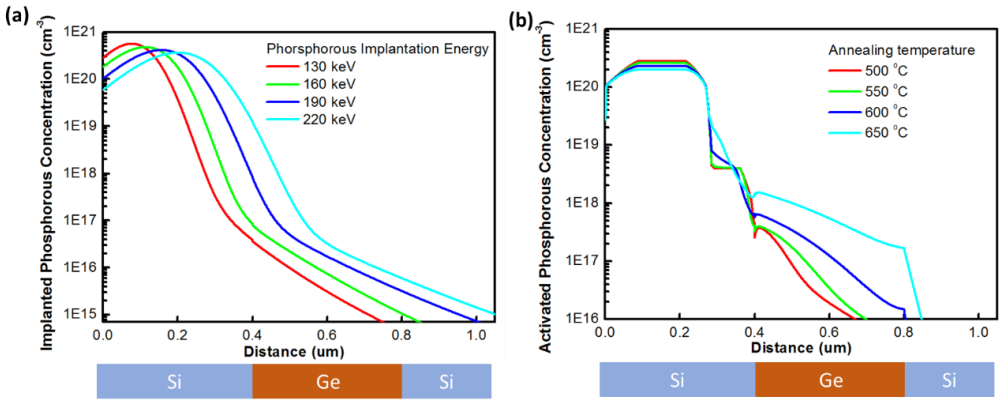

Figure 3.6 (a) Implanted phosphorous concentration as a function of phosphorous implantation energy with a top 100 nm shadow oxide. (b) Activated phosphorous concentration as a function of annealing temperature for the 30 minutes duration with 7 degrees tilt, the implantation energy of 190 keV, the dose of $8x10^{15}$ cm^{-2}, and 100 nm shadow oxide removed after annealing.

The overall dopant distribution across the layers is modeled based on the processing steps and temperatures during the processing of the layers starting from SOI layer implantation, to Ge epitaxial growth, to Si growth, to top Si implantation and annealing. The overall dopant concentration is plotted in Figure 3.7. This distribution is critical in the later model and comparison between the current-voltage (IV) measurement under DC bias for electrical contacts and diode performance evaluations in Chapter 8. That also serves as the parameters for the electric field simulation in the time domain in the following section.

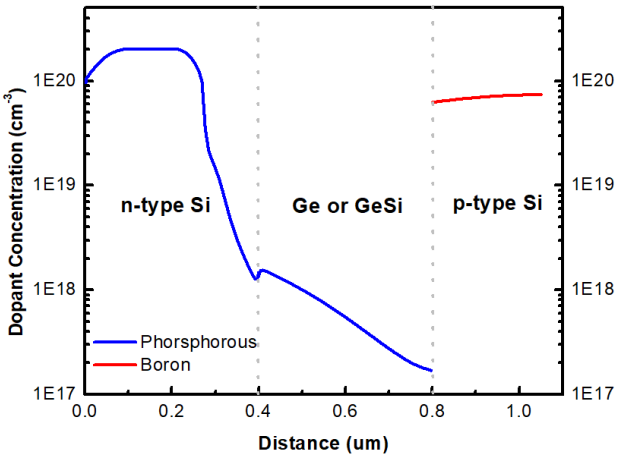

Figure 3.7 Dopant concentration and distribution simulated in the layers after all the film growth and processing steps.

3.2.2 Electrical field transient model for high-speed modulator electrodes

The electric field distribution model in the time domain is built using the COMSOL multiphysics Semiconductor module. As shown in Figure 3.8, the model takes into account the n-Si on GeSi on the p-Si ridge waveguide structure. The metal contacts are placed on top of the diode stack and the bottom Si layer next to the diode stack, as illustrated in Figure 3.8 (a). The reverse bias of 3 V is applied in the contact terminals. The variant is the distance of the bottom metal contact to the edge of the modulator waveguide. That is critical in the design because the gap between the bottom metal contact and the modulator needs to be minimized to enhance the electric field accumulation speed and intensity, as well as to achieve a compact device layout as possible. Meanwhile, it needs to reserve enough distance to avoid excessive loss due to the metal-include absorption in the ambiance of the waveguides. The electric field intensity is evaluated to ensure a uniform field along the vertical direction in the Ge or GeSi modulator waveguide, as shown in Figure 3.8 (b) with arrows showing the direction of the electric field across the waveguide. It has

been shown in Figure 3.8, a uniform electric field intensity is achieved across the vertical plane, which aligns with the top and bottom Si electrodes.

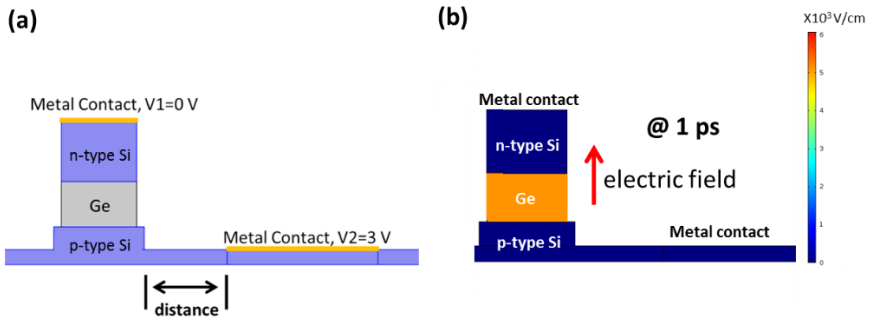

Figure 3.8 (a) The schematic of the finite element model in the time domain for modulators with top and bottom Si contacts and metals contacts. (b) example of electric field intensity and distribution across the device for 3um distance of the bottom metal contact away for the modulator edge at the one ps time frame.

The electric field intensity as a function of time and distance of the bottom metal from the modulator edge is plotted in Figure 3.9. It is noticed that the time needed to build up a uniform and sufficient electric field across the modulator waveguide is in less than one ps, which corresponds to the responsive frequency of ~ one THz. An uniform electric field intensity in the Ge is GeSi modulators is determined by the electric field intensity at the center plane of the modulator active region at a certain modulation frequency. That indicates the limiting factor is not the transient effect of the electric field in the electroabsorption modulator but possibly the resistance-capacitance (RC) delay of the device. The investigation of the RC delay on the device modulation speed is discussed in Chapter 8 with the device's electrical measurements. The distance of the bottom metal contact from the waveguide modulator edge is designed to be 3 um in the device layout, as illustrated in Figure 3.9. The high-speed modulator electrodes utilized the ground-signal-ground electrodes configuration, which reduces the capacitive coupling of the signal lines and

ensures the sufficient signal level at high-speed operation. The doping profiles for Si top and bottom contacts are not yet optimized. The lower doping levels might be preferred to reduce the impurity induced background absorption in the modulator region, which further reduces the device insertion loss. Because the electroabsorption utilizes the field-induced effect instead of the free carrier injection, its carrier distribution response time is less of a limiting factor. In Chapter 10, a systematic study of the optimized doping profile for a sufficiently high-speed modulation and superior modulators performance is discussed.

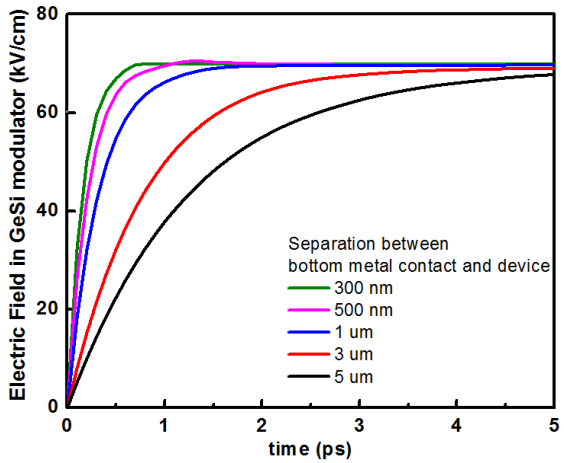

Figure 3.9 Electric field intensity in the waveguide modulator in a time domain with the various separation distance between the bottom metal and the modulator edge.

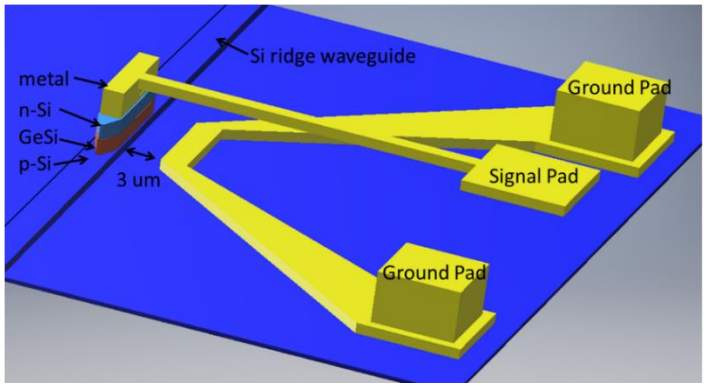

Figure 3.10 Schematic of ground-signal-ground electrodes design for GeSi waveguide modulators with top and bottom Si contacts.

Chapter 4 Strain model and bandgap engineering for modulator arrays

Extensive research concerning the effect of strain on the band structure of semiconductors has been conducted with the focus on the applications in electronic and optoelectronic devices in recent decades. Strained Si on the GeSi alloy layer has been developed for high-frequency CMOS compatible devices. Strain in material causes the lattice change of the semiconductor crystals, thereby alternating their band structures. The semiconductor parameters that can be engineered by strain are the bandgap and the carrier mobility in electronic and photonic devices. Bandgap engineering modifies the absorption properties so that photon absorption of the material can be tuned to fit the application requirements. That is the critical engineering parameter of this thesis work. The Ge and GeSi waveguide modulator design discussed in Chapter 3 has covered the design on the optical coupling with high extinction ratio and low insertion loss, and the design on electrical contacts for uniform electrical field application with a fast response and low energy consumption. In this chapter, the design on the stressor layer and its effect on modulator operation wavelength are discussed for an individual modulator design first. Then a one-for-all modulator array design is proposed with an innovative design for high-modulation efficiency, low cost, and large scale modulator integration on electronic and photonic integrated systems. All the device design fulfills the design rules in CMOS compatible fabrication procedures, and are readily adaptable for CMOS integrated electronic and photonic devices fabrications.

4.1 GeSi bandgap and strain correlation

The fundamental physics of strain and bandgap relationship is introduced here. It serves as a theoretical guideline for the straining engineering in GeSi electroabsorption modulator array. That bridges the design parameter of the modulator waveguide dimensions and the modulator performance parameters in its optical modulation domain. The lowest bandgap of the bulk Ge is an indirect gap of 0.664 eV at the L valley (corresponding to the wavelength of 1867nm), and the second-lowest bandgap is a direct gap of ~0.800 eV at the Γ valley (corresponding to the wavelength of 1550nm). The indirect bandgap transition is not efficient or dominant due to the fact that a phonon with a precise crystal momentum is required together with a photon to complete the excitation of an electron from the valence band to the L valley. For the wavelength longer than 1550nm, the absorption of bulk Ge is mainly due to this indirect bandgap transition. It is beneficial from an application perspective to increase the efficiency of Ge electroabsorption modulators in the broad optical band for telecommunication. Therefore, it would be desirable to engineer the bandgap of Ge by some means so that the absorption with the applied electric field in the wavelength range of interest would be much more efficient. As discussed in Chapter 2, the composition engineering has been performed in the Ge and GeSi epitaxial growth procedure, which fabricated GeSi epitaxial films with 0% Si, 1% Si, and 3% Si composition on Si-on-insulator substrates. The strain engineering is then applied to all three epitaxial films with the device fabrication. The previous experimental studies on the effect of stress/strain on the band structure of Ge have been based on uniaxial, biaxial, or hydrostatic compression tests in the material's structure of epitaxial films, mesas, and bulk [79-87]. Thus, there have been not many experimental reports on the effect of uniaxial stress either tensile or compressive with a constant strain on the other transverse axis on the band structure of Ge and GeSi waveguides. This chapter provides a

theoretical study of the Ge and GeSi waveguide design on the applied stressor and predicts the modulator wavelength region as a function of strain in the waveguide, which serves as the guideline for the device fabrication and experimental results discussion.

Ge and Si both have the diamond cubic structure. The strain of the Ge and GeSi crystal can be generalized with the following equations. The deformation of the elastic solid is assumed. Hooke's law can predict the linear relation between stress tensor and strain tensor as,

$$\sigma_{ij} = C_{ijkl}\varepsilon_{kl} \quad \text{Eq. 4.1}$$

Under the cubic symmetry, this elastic stiffness tensor can be expanded by three coefficients, c_{11}, c_{12}, and c_{44}. Therefore, the equations can be simplified and inversely expressed with elastic compliance tensor s_{ij} into the following equations. The elastic compliance can be expressed via elastic stiffness constants. The values of the elastic compliance and stiffness constants are listed in Table 4.1.

$$\begin{pmatrix}\sigma_{11}\\ \sigma_{22}\\ \sigma_{33}\\ \sigma_{23}\\ \sigma_{31}\\ \sigma_{12}\end{pmatrix} = \begin{pmatrix}c_{11} & c_{12} & c_{12} & 0 & 0 & 0\\ c_{12} & c_{11} & c_{12} & 0 & 0 & 0\\ c_{12} & c_{12} & c_{11} & 0 & 0 & 0\\ 0 & 0 & 0 & c_{44} & 0 & 0\\ 0 & 0 & 0 & 0 & c_{44} & 0\\ 0 & 0 & 0 & 0 & 0 & c_{44}\end{pmatrix}\begin{pmatrix}\varepsilon_{11}\\ \varepsilon_{22}\\ \varepsilon_{33}\\ 2\varepsilon_{23}\\ 2\varepsilon_{31}\\ 2\varepsilon_{12}\end{pmatrix} \quad \text{Eq. 4.2}$$

$$\begin{pmatrix}\varepsilon_{11}\\ \varepsilon_{22}\\ \varepsilon_{33}\\ 2\varepsilon_{23}\\ 2\varepsilon_{31}\\ 2\varepsilon_{12}\end{pmatrix} = \begin{pmatrix}s_{11} & s_{12} & s_{12} & 0 & 0 & 0\\ s_{12} & s_{11} & s_{12} & 0 & 0 & 0\\ s_{12} & s_{12} & s_{11} & 0 & 0 & 0\\ 0 & 0 & 0 & s_{44} & 0 & 0\\ 0 & 0 & 0 & 0 & s_{44} & 0\\ 0 & 0 & 0 & 0 & 0 & s_{44}\end{pmatrix}\begin{pmatrix}\sigma_{11}\\ \sigma_{22}\\ \sigma_{33}\\ \sigma_{23}\\ \sigma_{31}\\ \sigma_{12}\end{pmatrix} \quad \text{Eq. 4.3}$$

$$s_{11} = (c_{11} + c_{12})/[(c_{11} - c_{12})(c_{11} + 2c_{12})] \quad \text{Eq. 4.4}$$

$$s_{12} = (-c_{12})/[(c_{11} - c_{12})(c_{11} + 2c_{12})] \quad \text{Eq. 4.5}$$

$$s_{44} = 1/c_{44} \quad \text{Eq. 4.6}$$

Table 4.1 Elastic stiffness constants of Si and Ge.

	c_{ij} (GPa)		s_{ij} (1/GPa)	
Si	c_{11}	165.8	s_{11}	7.7E-3
	c_{12}	63.9	s_{12}	-2.1E-3
	c_{44}	79.6	s_{44}	1.3E-2
Ge	c_{11}	128.5	s_{11}	9.8E-3
	c_{12}	48.3	s_{12}	-2.7E-3
	c_{44}	66.8	s_{44}	1.5E-2

The effect of bandgap distortion by the stress along [100] applied to the Ge or GeSi crystal structure can then be derived using deformation potential theory [77]. The valence band energy gaps are expressed into the following equations. These equations provide a foundation for strain simulation and bandgap engineering.

$$\Delta E_{HH} = \frac{1}{3}\Delta_0 - \frac{1}{2}\delta E_{100} \quad \text{Eq. 4.7}$$

$$\Delta E_{LH} = -\frac{1}{6}\Delta_0 + \frac{1}{4}\delta E_{100} + \frac{1}{2}\sqrt{\Delta_0^2 + \Delta_0\delta E_{100} + \frac{9}{4}(\delta E_{100})^2} \quad \text{Eq. 4.8}$$

$$\Delta E_{SO} = -\frac{1}{6}\Delta_0 + \frac{1}{4}\delta E_{100} - \frac{1}{2}\sqrt{\Delta_0^2 + \Delta_0\delta E_{100} + \frac{9}{4}(\delta E_{100})^2} \quad \text{Eq. 4.9}$$

$$\delta E_{100} = 2b(\varepsilon_{xx} - \varepsilon_{zz}) \quad \text{Eq. 4.10}$$

4.2 Individual waveguide modulator strain engineering

To understand the strain distribution in both the Ge and GeSi blanket films and their waveguide structures in the modulator, and to investigate the application of the stressor tuning the modulator's operation wavelength, a finite element strain model was developed. The Ge epitaxial film was simulated to have the growth on the Si-on-insulator (SOI) wafer at the temperature of 730 ^{o}C with the cyclic annealing from 650 ^{0}C to 850 ^{0}C, which is consistent with the experimental growth condition. The ~0.2% tensile strain was obtained in the epitaxial film in the simulation, taking into account the thermal expansion coefficient difference between the Ge and the Si substrate. Since the Ge epitaxial film needs to be fabricated into waveguides for the device application, the waveguide structure was defined in the model as an illustration in Figure 4.1. The ~0.2% tensile strain is maintained along the long axis of the waveguide, and the strain along the short axis of the Ge waveguide is relaxed gradually from the film-substrate interface to the top surface of the Ge waveguide. The equations derived from the deformation potential theory were applied to both the epitaxial films and the waveguides to calculate the strain effect on the band structure. As shown in Figure 4.1, the change of the Ge absorption edge as a function of strain ranged from the 5% compressive to 5% tensile has been modeled for both cases.

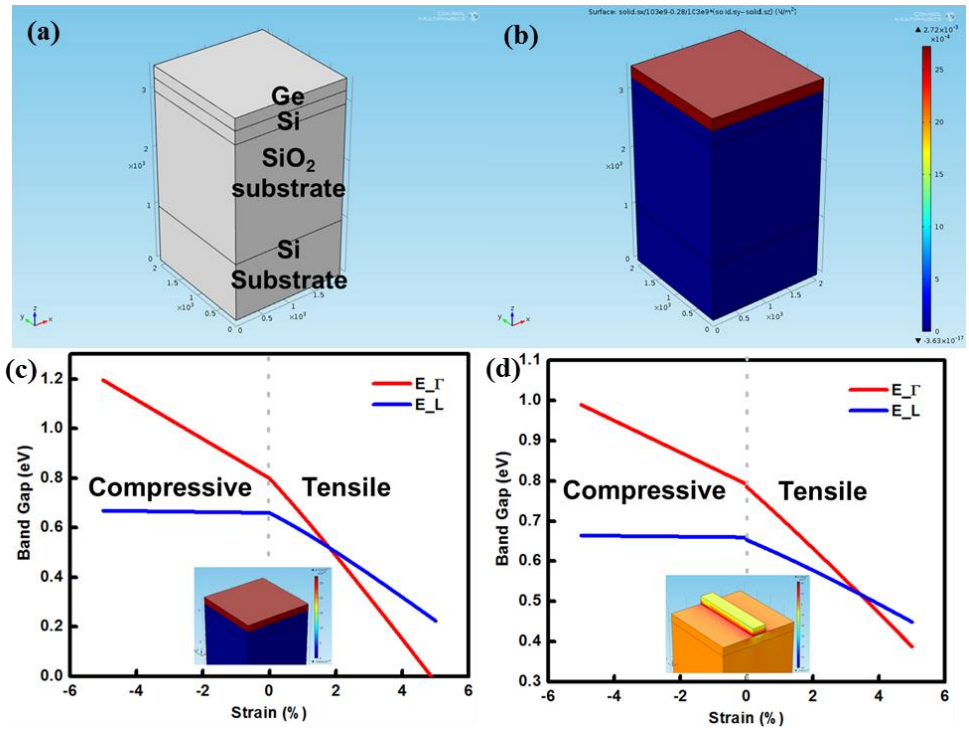

Figure 4.1 (a) schematic of the finite element strain model for Ge epitaxial film on SOI wafer; (b) Ge epitaxial layer shows 0.2% biaxial tensile strain in the model; (c) bandgap simulation as a function of strain in the Ge film; (d) bandgap simulation as a function of strain in the Ge waveguide.

The as-grown Ge waveguide on the SOI substrate has the absorption edge at the wavelength of 1600nm, which means the modulator has the operational wavelength range above and near 1600nm. In that case, the input light at the wavelength less than 1600nm will be absorbed by the Ge waveguide, and will not be able to participate in the electro-absorption modulation. The Ge absorption edge could be modified by applying an intrinsically-stressed material on the sides of the Ge waveguide. This method directly applies the strain on the short axis of the waveguides. The stressor layers were added to the model. The simulation results show that a 0.75 GPa compressive stress is required in the stressor layer to generate 0.4% compressive strain in the Ge

waveguide, and a 0.8 GPa tensile stress is needed in the stressor layer to achieve 0.4% tensile strain in the Ge waveguide.

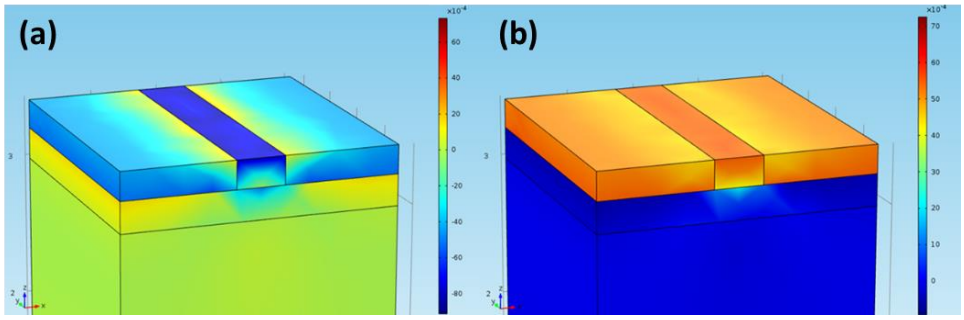

Figure 4.2 Strain distribution of the modulator with stressors on the sides under (a) 0.4% compressive strain and (b) 0.4% tensile strain in the finite element strain model

The non-uniformity of the strain in the Ge waveguide is observed in the model and makes it challenging to modulate the absorption edge. That causes absorption edge variation across the modulator waveguide. It is critical to design innovatively to achieve a uniform and stable strain distribution in a Ge or GeSi waveguide integrated modulator. A new design for the strain application was proposed in the electroabsorption modulator, which was inspired by a collaborative work done with Dr. Yiding Lin at Nanyang Technology University. By applying the strain on both Ge (or GeSi) and the underneath Si ridge waveguides, a more uniform strain distribution is achieved for both tensile and compressive conditions. With stressor on the sides of the modulator waveguides, top and bottom contact structures are adopted. Therefore, the underneath Si layer cannot be fully etched through. The Ge strain uniformity was then simulated as a function of Si contact thickness and concluded that 80 nm of Si is sufficient to serve as a contact layer and maintains the strain uniformity in the modulator waveguide.

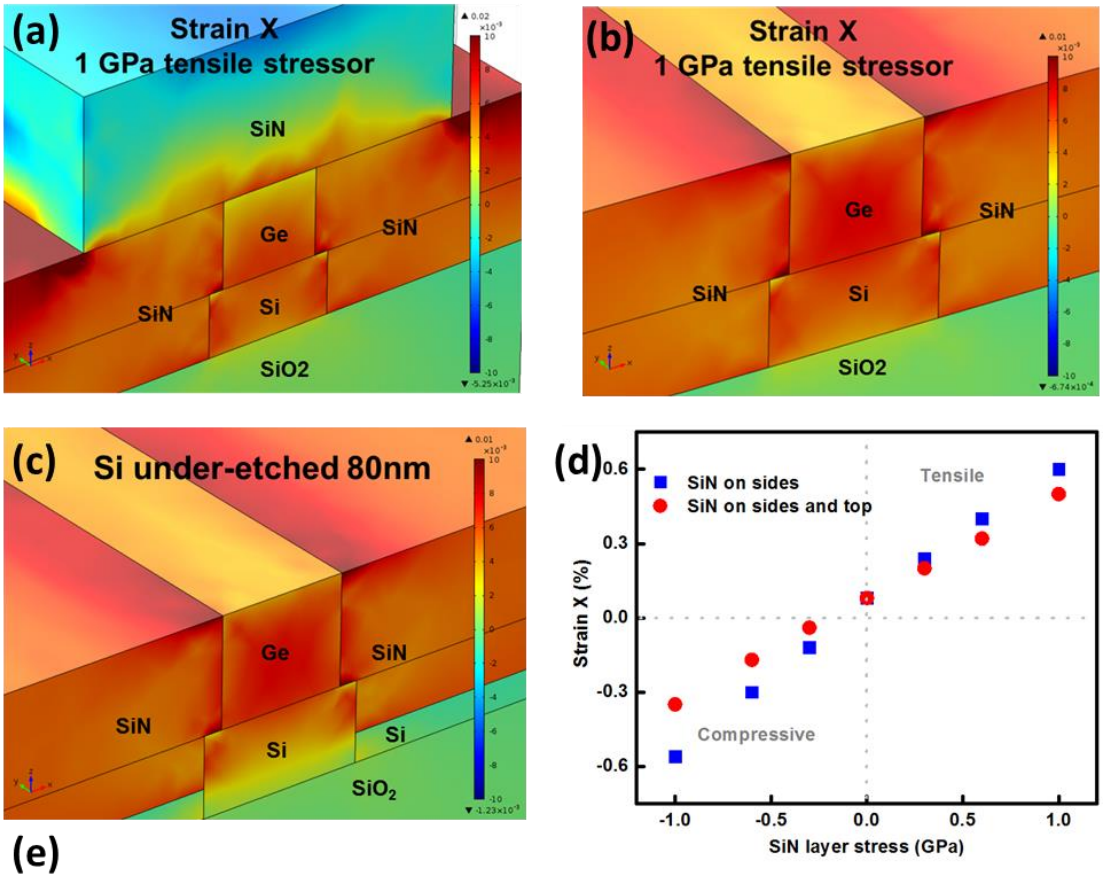

(e)

Si under-etched thickness (nm)	0	40	80	120	160	200
Ge strain variation (%)	0.05	0.05	0.05	0.10	0.12	0.40

Figure 4.3 Simulated strain distribution with 1 GPa tensile SiN_x stressor applied (a) on the top and sides of the Ge on Si waveguide, (b) on the sides of the Ge on Si waveguide, (c) on the sides of the Ge on Si waveguide with 80 nm Si un-etched. (d) Strain X as a function of the applied intrinsic stressor in comparison to the stressor applications in cases (a) and (b). (e) Table of the strain variation in Ge waveguide as a function of un-etched Si layer thickness.

Silicon nitride (SiN) synthesized via Plasma Enhanced Chemical Vapor Deposition (PECVD) is an attractive candidate material for the stressor application. The origin of intrinsic stress in the PECVD silicon nitrogen composite film is a function of atoms per volume and forces

affecting bond lengths. At lower frequency, there is higher ion energy. Hence, ion bombardment and densification are increased, which makes the film more compressive. While at a higher PECVD frequency, the opposite happens, and the tensile stressed film is deposited. Therefore, the concentration of high and low radio frequencies in the PECVD process can be controlled to tune the stress in the silicon nitrogen composite, as shown in Figure 4.4 (b). The intrinsic stress in the dual-frequency PECVD deposited SiN film can achieve stress ranged from 1 GPa compressive to 0.6 GPa tensile. That meets the requirement for the strain variation in the modulator material. Therefore, a complete map of the effect of the GeSi composition, and the induced strain in the waveguide on the absorption band edge with the applied external stressor layer's intrinsic stress is completed as Figure 4.4. This map is based on the waveguide width of 400 nm. The strain in the waveguide and the waveguide material composition are independent of the waveguide dimension. The waveguide width, in this case, is fixed to aid in the correlation of the PECVD SiN_x intrinsic stress. With all the information obtained from this map, the GeSi electroabsorption modulator can be designed to operate at any specific waveguide with a narrow optical bandwidth of ~15nm due to the limitation of Franz-Keldysh effect. However, to achieve the modulation at a broad optical window, individual strain and material optimizations are still needed. This might not be the only solution for a large scale modulator array with a broad modulation optical bandwidth.

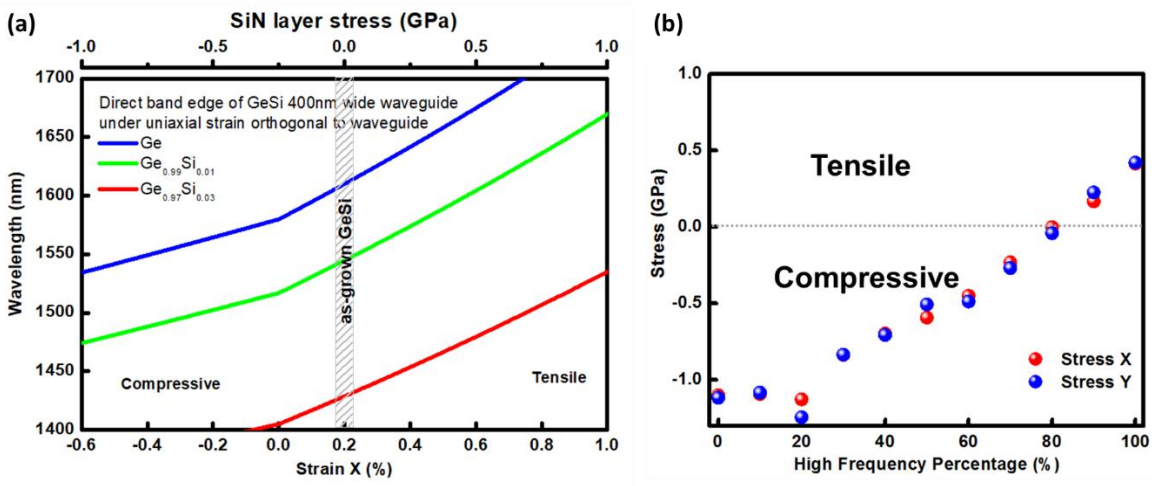

Figure 4.4 (a) Modulator materials absorption edge as a function of strain X in the modulator waveguide with the top x-axis of the stressor layer's intrinsic stress needed for 400 nm wide Ge on Si waveguides. (b) The applied intrinsic stress as a function of the high-frequency components in the dual-frequency (low frequency and high-frequency mixing) PECVD SiN_x deposition process.

4.3 One-for-all strained modulator array design

The conventional strategy of inserting a modulator for a specific wavelength modulation involves specific materials engineering and device fabrication for each individual modulator [31-33]. To realize an integrated system with broadband modulation, multiple modulators have to be fabricated individually and assembled onto a chip. Each fabrication step adds cost to design and processing. Integrating more modulators for multiple operation wavelengths gives broader band coverage and higher optoelectronic data processing capacity. In the thesis work, a one-for-all strained Ge and $Ge_{0.99}Si_{0.01}$ modulator array design is proposed and demonstrated to cover a broad telecommunication band with multiple modulators designed and fabricated simultaneously in a single lithography and patterning flow [88-89]. A stressor layer applies a homogeneous strain to the modulator structures. By changing the modulator width, the strain in the modulator changes, tuning

the material bandgap and, therefore, the modulation operation wavelength. Thus, modulators made of the same material can operate at various wavelengths with the same stressor layer by simply changing in the dimension of the modulators.

4.3.1 Ge modulator array with a compressive stressor

Compressive strained Ge waveguide modulator arrays are studied in this section. The silicon nitride compressive stressor layer are designed to be placed on both sides of the Ge and Si waveguides for strain engineering. The modulator waveguide width is a unique design parameter to vary the modulator material's bandgap as a response to the external stressor layer. The 1GPa compressive stressor layer is designed to be placed on the sides of the modulator waveguides to apply uniform and sufficient compressive stress across the short axis (X-axis in the solid mechanics model coordinates) of the modulator waveguide. As a proof of concept, Ge waveguides with a width of 400nm, 700nm, 2um, and 4um are modeled using the solid mechanics module in COMSOL Multiphysics, as introduced in the previous section. Both p-Si and n-Si contacts and bottom Si waveguides are structured in the model. The deformation potential theory based on quantum mechanics is applied to derive the strain effect on the band structure of semiconductor materials. The electroabsorption modulator operation wavelength is related to its materials band structure; in this case, the direct bandgap of the Ge waveguides. Therefore, the correlation between the operation wavelength and modulator waveguide strain is established. As illustrated in Figure 4.5, a uniform compressive strain of about 0.8%, 0.7%, 0.5%, and 0.3% is distributed across in the Ge waveguides with widths of 400nm, 700nm, 2μm, and 4μm, which corresponds to absorption edges at 1520 nm, 1524 nm, 1539 nm, and 1559 nm, respectively. Therefore, a compressively strained Ge electroabsorption modulator array is demonstrated theoretically to achieve a much

wider optical wavelength window of over 80 nm. The experimental demonstration based on this theoretical design is shown in later chapters.

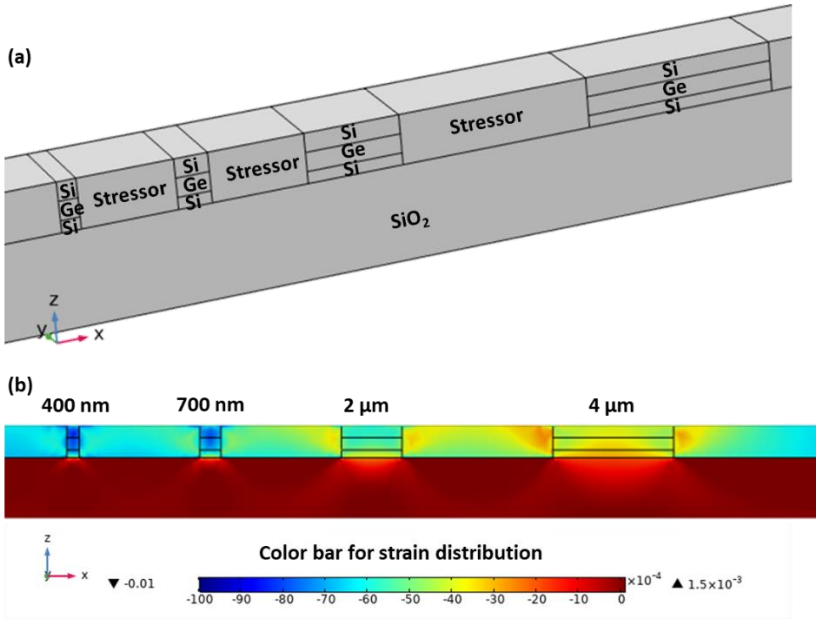

Figure 4.5 (a) Solid mechanics model of Ge on Si waveguide structure with top Si contact and 1GPa compressive Silicon nitride stressor on waveguide sides, (b) strain distribution across Ge waveguides as a function of waveguide width.

4.3.2 $Ge_{0.99}Si_{0.01}$ Modulator array with a Tensile stressor

The strain model is then applied to investigate the tensile strain distribution in $Ge_{0.99}Si_{0.01}$ modulator array for broadband modulation. The stressor layer is designed to be silicon nitride with a tensile stress of 0.6 GPa. The strain distribution in 500nm, 1µm, and 3µm wide $Ge_{0.99}Si_{0.01}$ waveguide modulators are plotted in Figure 4.6. The uniform tensile strains of 0.4%, 0.3%, and 0.2% are obtained in $Ge_{0.99}Si_{0.01}$ waveguides with widths of 500nm, 1µm, and 3µm, respectively. The electro-absorption modulator operation wavelength is related to its material band structure. Therefore, the correlation between the operation wavelength and modulator waveguide strain was

established and plotted in Figure 4.6. The $Ge_{0.99}Si_{0.01}$ waveguide modulators with widths of 500nm, 1μm, and 3μm are simulated to have absorption edge at 1572 nm, 1563 nm, and 1542 nm, respectively. Therefore, the tensile strained $Ge_{0.99}Si_{0.01}$ electroabsorption modulator array is demonstrated theoretically to achieve a much wider optical wavelength window of over 60 nm. The experimental demonstration based on this theoretical design is shown in later Chapters.

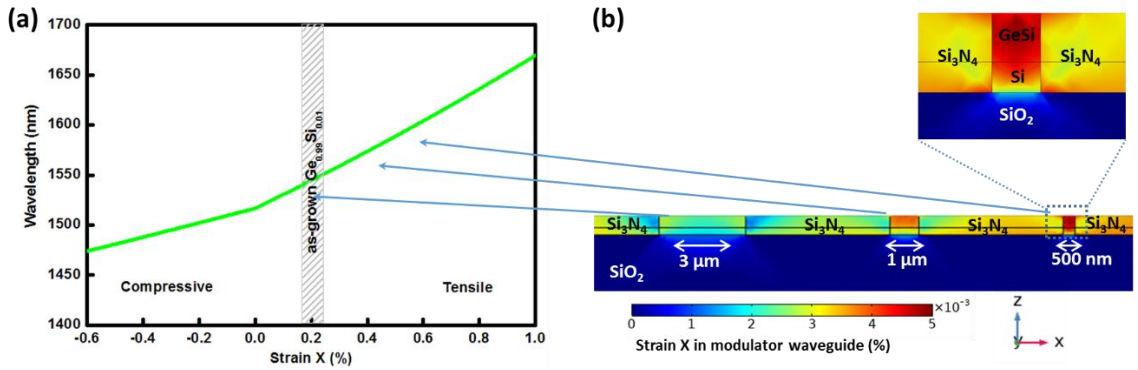

Figure 4.6 (a) modulator absorption edge as a function of uniaxial strain X in $Ge_{0.99}$ $Si_{0.01}$ waveguide. (b) strain distribution in the waveguides under the 0.6GPa stressor layer.

The reasons for the two separate modulator array designs of the Ge modulators with compressive stressors and $Ge_{0.99}Si_{0.01}$ modulators with tensile stressors are mainly based on the limitation of the optical testing wavelength window. The single-mode laser source and photodetector with the optical window from 1510 nm to 1610 nm are available for the optical transmission measurements. As a demonstration of this one-for-all stress engineering innovation on modulator arrays for both tensile and compressive stressors application, the modulator arrays with two different compositions and corresponding stressor choices are intentionally designed to ensure the designed modulation performance is captured in our optical testing wavelength window. The inclusion of 1% Si in GeSi causes the bandgap shift toward lower wavelength, hence allows

the application of tensile stressor to demonstrate the bandgap shift toward higher wavelength in the range of 1510 nm to 1610 nm.

4.4 Experimental results on strained waveguides

In order to evaluate the strain effect on the waveguide structure for electroabsorption modulators application, the test structures of 300 nm tall Ge waveguides on 250 nm tall Si ridge waveguide with 80 nm unetched on SiO_2 substrate have been fabricated. The width of the waveguides is varied from 400 nm to 4 um. It mimics the real stressor application in the Ge or GeSi waveguide modulator array. The difference between this test structure and the actual devices is the placement of top Si contacts and metal contacts. In this test structure, only the Ge waveguide with a specific width was aligned on top of the Si waveguide with the corresponding width. It matches well to the strain model structures designed in the previous sections. The placement of top doped Si waveguide and the metal contact would cause absorption in the micro-Raman spectrum measurements, and reduce the resultant signal to noise ratio. Therefore, there is no top Si or metal contact placed on top of the Ge waveguides. However, the strain information obtained in this test structure should correctly reflect the actual strain in the real modulator array because the placement of top Si and metal contacts does not alter the strain effect in the modulators waveguide. The 0.6 GPa SiN_x tensile stressor layer and the 1.0 GPa SiN_x compressive stressor layer were deposited separately on two identical sample chips with the testing waveguides. Due to the conformal deposition of the PECVD SiN_x, another step of pattern alignment, lithography, and dry etching was performed to remove the SiN_x stressor layer on top of the waveguides. It is illustrated in the strain engineering design section that the top SiN_x would reduce the strain effect in the modulator waveguides and induce non-uniform strain distribution in the waveguides.

Micro-Raman measurements were used to determine the strain in the various Ge on Si waveguides. As shown in Figure 4.7, the obtained Raman peak shifts were used to derive the strain effect in the waveguides. Theoretically speaking, the strain induces changes in the equilibrium positions of the atoms in the semiconductor crystal. The phonon structure is consequently altered due to the anharmonic terms of the interatomic potential. Therefore, the phonon frequencies and Raman scattering tensors are modified due to the strain effect. Monitoring the resulting changes in the Raman mode frequencies makes Raman spectroscopy a promising technique for studying strain distributions in semiconductor devices. Under the action of strain, the threefold degenerate optical phonon of a cubic crystal such as Si or Ge generally splits into three modes (TO_1, TO_2, and LO). The frequencies ω_i of the modes can be expressed using the quasi-harmonic approximation from the eigenvalues λ_i of the secular matrix,

$$\begin{pmatrix} p\varepsilon_{11}+q(\varepsilon_{22}+\varepsilon_{33}) & 2r\varepsilon_{12} & 2r\varepsilon_{13} \\ 2r\varepsilon_{21} & p\varepsilon_{22}+q(\varepsilon_{11}+\varepsilon_{33}) & 2r\varepsilon_{23} \\ 2r\varepsilon_{31} & 2r\varepsilon_{32} & p\varepsilon_{33}+q(\varepsilon_{11}+\varepsilon_{22}) \end{pmatrix} \quad \text{Eq. 4.11}$$

by using the following relation,

$$\omega_i^2 = \omega_0^2 + \lambda_i \quad \text{Eq. 4.12}$$

Where ω_0 is the degenerate (unperturbed) phonon frequency. ω_0 = 300 cm^{-1} for Ge. In the equations, p, q , and r are the phonon deformation potentials. p=-1.45 ω_0^2, q=-1.95 ω_0^2 and r = -1.10 ω_0^2 for Ge. The ε_{ij} are the components of the strain tensor, which correlate with the stress tensor components via Hooke's law. Similar to the deformation potential theory discussion in the device strain engineering section, the non-zero components of the compliance tensor for a cubic crystal are S_{11}, S_{12}, and S_{44}. Together with the appropriate selection rule, equations can be

formulated to obtain the stress tensor from the experimentally determined modified frequencies ω_i in a Raman spectrum. It was observed in the literature that the Raman spectroscopy is sensitive to the LO mode using the conventional confocal Raman spectroscopy on the (001) oriented cubic crystals. Applying the stress-induced LO phonon frequency splitting relation with the biaxial stress, σ11, and σ12, we derived Equation xx. For Ge or GeSi epitaxial film on the SOI substrate, σ11= σ12, as determined in both the strain model on the epitaxy film and the XRD and photoreflectance measurements in Chapter 2. For Ge on Si waveguide test structures, one of the strain is fixed to be the film strain along the long axis of the waveguide; another strain component is the SiN_x stressor induced strain along the short axis of the waveguides. These two strain components in each waveguide were decomposed and extracted from the Raman measurements on each waveguide structure.

$$\omega_i^2 - \omega_0^2 = [pS_{12} + q(S_{11} + S_{12})](\sigma_{11} + \sigma_{12}) \qquad \text{Eq. 4.13}$$

A Raman peak shift from 300.84 cm^{-1} to 300.01 cm^{-1} is observed for the comparison between bulk Ge and 300 nm thick Ge epitaxial film on Si substrate. Utilizing the as-derived strain and Raman frequency correlation, the Ge epitaxial film's biaxial strain of ~0.2% tensile is obtained. The Raman spectrum for the Ge on Si waveguide structures under 1 GPa compressive stress or 0.6 GPa tensile stress are plotted in Figure 4.7 (c) and (d), respectively. The resultant signal to noise ratio for waveguides with widths of 400nm and 500nm is too weak to obtain used Raman peak information. The Raman spectrum is evaluated for waveguides with widths from 700nm to 4 um. The Raman peak is shifted from 301.54 cm^{-1} to 300.72cm^{-1}, comparing 0.7 um wide waveguide to 4 um wide waveguide with 1 GPa compressive stressor. The Raman peak is shifted from 299.92 cm^{-1} to 300.35cm^{-1}, comparing 0.7 um wide waveguide to 4 um wide waveguide with 0.6 GPa

tensile stressor. The tensile stressor shifts the Raman peak to lower wavenumbers, while the compressive stressor shifts the Raman peak to higher wavenumbers. Meanwhile, the narrower waveguides are more responsive to the stressor effect; therefore, the magnitude of the Raman peak shifts is larger.

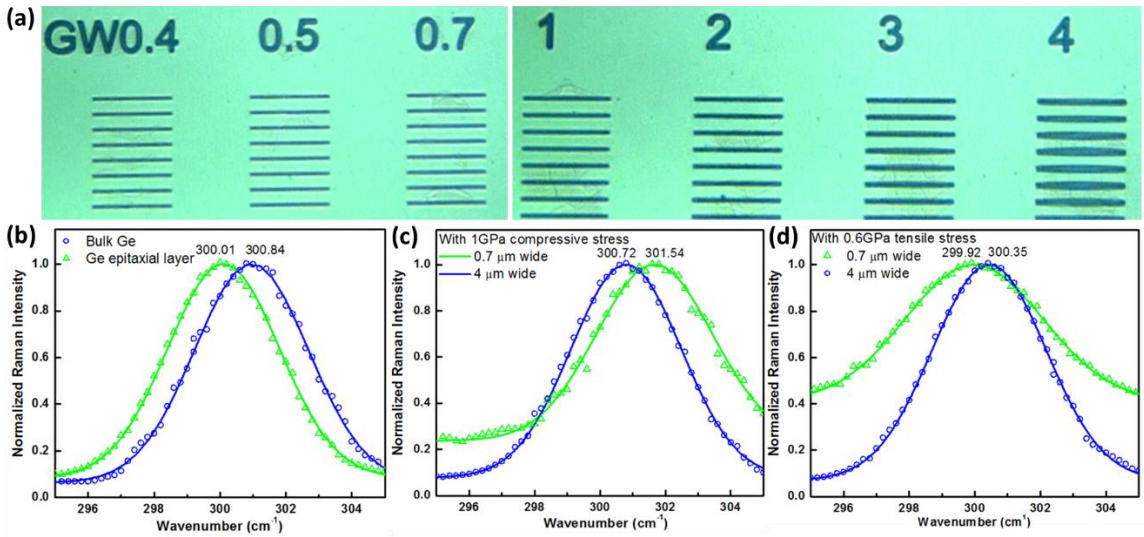

Figure 4.7 (a) Optical microscopic image of Ge waveguides with various widths and labels (e.g., GW0.4 means Ge Waveguide with a width of 0.4 um). The Raman spectroscopic measurements of (b) bulk Ge and 300 nm Ge epitaxial layer on Si substrate, (c) 0.7 um and 4 um wide Ge on Si waveguides with 1 GPa compressive SiN_x stressor, and (d) 0.7 um and 4 um wide Ge on Si waveguides with 0.6 GPa tensile SiN_x stressor.

The strain components in the waveguides are extracted from the measured Raman spectrum. The strain X (along the short axis of the waveguides) values are listed in Table 4.2 in comparison with the simulated Strain X values in the strain engineering model. The scatter plot of the strain X as a function of the waveguide width, and SiN_x stressor's intrinsic stress is plotted in Figure 4.8 for a better visual comparison between the expected strain effect from the strain engineering model

and the actual strain effect in the fabricated Ge on Si waveguides. This result experimentally demonstrates the impact of applying SiN_x stressors on the sides of the Ge waveguides could effectively induce strain in the modulator waveguides. It serves as the cross-check for the strain application in the real GeSi modulator devices.

Table 4.2 Comparison of the strain X values from the COMSOL strain engineering model and Raman Measurements as a function of Ge on Si waveguide width and stressor layer application.

	COMSOL Simulation for Strain X (%)		Raman Measurement for Strain X (%)	
Waveguide Width (nm)	1GPa compressive stressor	0.6GPa tensile stressor	1GPa compressive stressor	0.6GPa tensile stressor
400	-0.80	0.40	Too low Raman signal intensity due to narrow waveguides	
500	-0.78	0.39		
700	-0.74	0.37	-0.73	0.33
1000	-0.67	0.33	-0.65	0.27
2000	-0.53	0.27	-0.52	0.21
3000	-0.40	0.18	-0.36	0.12
4000	-0.26	0.12	-0.20	0.04

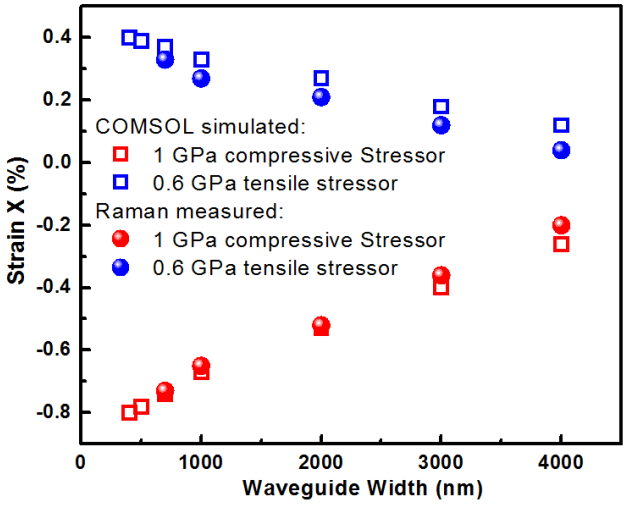

Figure 4.8 The strain X (strain along the short axis of the Ge on Si waveguide) values as a function of waveguide width and stressor layer application based on strain engineering model and Raman spectrum measurements.

Chapter 5 Electroabsorption modulation model for GeSi modulator arrays

The direct bandgap absorption in Ge can be effectively altered by an applied electric field, demonstrating a strong electroabsorption effect at the band edge. This strong effect could be due to the Franz-Keldysh effect in bulk or Ge films or the quantum-confined Stark effect in Ge quantum wells [54-61]. Both of these two effects have been demonstrated for individual modulators with specific optical windows. This chapter focuses on the theoretical simulation for the Ge and GeSi electroabsorption modulator performance. The chapter bridges the design components discussed in Chapters 3 and 4 with the actual modulator performance in later chapters via a comprehensive model on the modulator array based on the Franz-Kelydesh effect. The modulation model links the modulator material parameters, including strain and composition, and the modulator electrode design parameters, including applied voltage and effective electrical field. The resultant parameters are the absorption coefficient and extinction ratio of every modulator in the array. It is significant to have a real-case prediction on the devices to compare and validify the measured device performances, and to learn the impact of the factors in the design or fabrication of the performance of the Ge and GeSi modulator arrays.

5.1 Franz-Keldysh effect in the Ge and GeSi electroabsorption modulators

As briefly introduced in Chapter 1, the Franz-Keldysh effect plays a significant role in electroabsorption modulators using direct bandgap semiconductor materials. Although Ge is not a direct bandgap semiconductor, its energy difference between the direct and indirect bandgap is relatively small. The Franz-Kelysh effect is dominant at the direct bandgap of the Ge and GeSi thin films [90-95]. Figure 5.1 is an illustrative figure for the absorption coefficient with the Franz-Keldysh effect. Without the electric field, the absorption coefficient only increases when the

incident energy is higher than the direct bandgap of the material. The incident photons with an energy less than the semiconductor bandgap are not able to excite the electron transition from the top of the valence band to the bottom of the conduction band without the electric field. The absorption coefficient follows the square-root relation for direct gap transitions, that is, proportional to the joint density of states. With an applied field, the bands are tilted by the electric field, which assists the band-to-band tunneling under photon excitation. A photon with energy slightly less than the bandgap can excite an electron from the valence band to the conduction band through a cooperative tunneling process across the tilted energy barrier. Therefore, the absorption coefficient at the energy less than the bandgap increases significantly with the applied electric field. In the region where the incident energy is greater than bandgap, the absorption curve shows the Franz-Keldysh oscillation near the band edge.

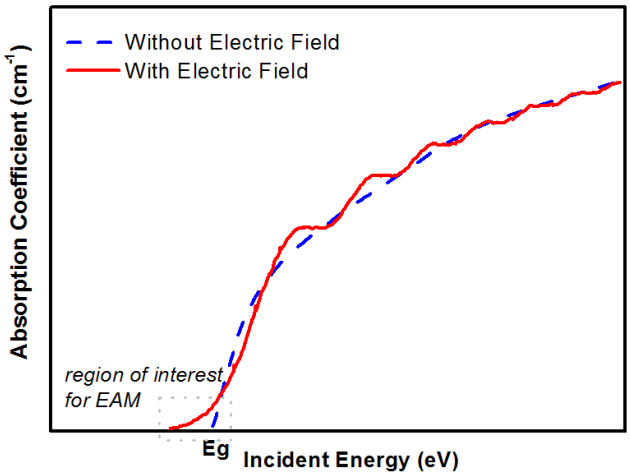

Figure 5.1 Illustration of the Franz-Keldysh effect in the absorption coefficient [52].

The Ge and GeSi modulation model can be built based on solving the fundamental Schrodinger equation of an electron-hole pair in the presence of an applied electric field, F, along the vertical z-direction. With the total energy expressed in Eq. 5.1, the solution to this Schrodinger equation is to describe the modulation as a function of an applied electric field.

$$\varphi(z)\left(-\frac{\hbar^2}{2m_r}\frac{d^2}{dz^2}+eFz\right)=E\varphi_{E_z}(z) \quad \text{Eq. 5.1}$$

$$E=\frac{\hbar^2}{2m_r}\left(k_x^2+k_y^2\right)+E_z \quad \text{Eq. 5.2}$$

$$\varphi_{E_z}(z)=(\frac{2m_r}{\hbar^2})^{\frac{1}{3}}[\frac{A_i}{(eF)^{\frac{1}{6}}}][\left(\frac{2m_r eF}{\hbar^2}\right)^{\frac{1}{3}}(z-\frac{E_z}{eF})] \quad \text{Eq. 5.3}$$

Where $A_i(z)$ is the airy function. With Fermi's Golden Rule and integration over the quantum states, the expressive correlation of the absorption coefficient of the direct bandgap transition with an applied electric field is obtained as Eq. 5.4.

$$\begin{aligned}&\alpha(hv,F)\\&=\left[\frac{e^2E_p}{24\pi n_r c\varepsilon_0 m_0 v}\right]\{(\frac{2m_{r,lh}}{\hbar^2})^{3/2}\sqrt{\hbar\theta_{F,lh}}\left[-\eta_{lh}Ai^2(\eta_{lh})+A_i'^2(\eta_{lh})\right]\\&+\{(\frac{2m_{r,hh}}{\hbar^2})^{3/2}\sqrt{\hbar\theta_{F,hh}}\left[-\eta_{hh}Ai^2(\eta_{hh})+A_i'^2(\eta_{hh})\right]\}\end{aligned} \quad \text{Eq. 5.4}$$

The parameters in this equation can be further expressed using basic material parameters, as shown in the following equations.

$$m_{r,lh}=m_e^{\Gamma}m_{lh}/(m_e+m_{lh}) \quad \text{Eq. 5.5}$$

$$m_{r,hh} = m_e^{\Gamma} m_{hh}/(m_e + m_{hh}) \quad \text{Eq. 5.6}$$

$$\hbar\theta_{F,lh} = [\frac{\hbar^2 e^2 F^2}{2m_{r,lh}}]^{1/3} \quad \text{Eq. 5.7}$$

$$\hbar\theta_{F,hh} = [\frac{\hbar^2 e^2 F^2}{2m_{r,hh}}]^{1/3} \quad \text{Eq. 5.8}$$

$$\eta_{lh} = \frac{E_g^{\Gamma,lh} - h\nu}{\hbar\theta_{F,lh}} \quad \text{Eq. 5.9}$$

$$\eta_{hh} = \frac{E_g^{\Gamma,hh} - h\nu}{\hbar\theta_{F,hh}} \quad \text{Eq. 5.10}$$

Eq. 5.4 can be seen as the comprehensive equation for the modulation model, which considers the transitions from both light hole and heavy hole band transitions. Those two transitions involve different effective masses and strain-induced bandgaps for Ge and GeSi waveguide materials with various widths. Although Ge and GeSi have both direct and indirect band transitions with the FK effect, it has been reported that the FK effect of the indirect bandgap is three orders of magnitude lower than that of the direct bandgap in Ge [91-93]. The effect of the indirect gap transition, therefore, is not included in this modulation model. The modulation wavelength of interest is from 1510 nm to 1610 nm in the model, which is consistent with the actual testing wavelength range for the device transmission characterization. The contribution of the indirect gap absorption to the overall absorption coefficients is not negligible and taken into consideration in the discussion of the experimental results in Chapter 6. The total absorption coefficient is a sum of the contributions from the direct and indirect band gaps of Ge or GeSi.

The composition of GeSi is considered in the modulation model. As introduced in Chapter 2, a few atomic percentages of Si inclusion can be alloyed with the Ge to shift the modulator's optimal operation wavelength to a lower wavelength. The material parameters used in the modulation model adapt the contribution of Si inclusion. Although the minimal direct gap of Si is 3.4 eV, the actual band position of interest is the cross-over of two conduction bands at crystal wave vector of k=0. Therefore, the fundamental direct gap of Si is $E_{k=0}$ = 4.06 eV. Therefore, the linearly interpolated direct bandgap of unstrained $Ge_{1-x}Si_x$ is $E_g(Ge_{1-x}Si_x)=0.8+3.26x$ [75]. These linear interpolations work well for GeSi mainly because Ge and Si form a complete solid solution, and the Si inclusion amount is relatively small [74,92]. The deformation potential theory has been introduced and discussed for the strain modeling in Chapter 4. The linear interpolations on the deformation potentials is applied to consider the GeSi strain effect on the direct bandgap transition with a small Si inclusion. The elastic constants and split-off energy are listed in the following equations.

$$a(Ge_{1-x}Si_x)=-8.97+3.87x \quad \text{Eq. 5.11}$$

$$b(Ge_{1-x}Si_x)=-1.88-0.32x \quad \text{Eq. 5.12}$$

$$d(Ge_{1-x}Si_x)=-4.7-0.1x \quad \text{Eq. 5.13}$$

$$C_{11}(Ge_{1-x}Si_x)=128.53+37.27x \quad \text{Eq. 5.14}$$

$$C_{12}(Ge_{1-x}Si_x)=48.26+15.64x \quad \text{Eq. 5.16}$$

$$C_{44}(Ge_{1-x}Si_x)=68.80+12.80x \quad \text{Eq. 5.17}$$

$$\Delta_0(Ge_{1-x}Si_x)=0.29-0.246x \quad \text{Eq. 5.18}$$

The energy difference between the direct and indirect gaps increases with the Si inclusion. That leads to a higher background absorption loss due to indirect band transition and a lower extinction ratio. The effective mass of electrons and holes of $Ge_{1-x}Si_x$ is almost the same as Ge for the Si inclusion less than 3%. Therefore, the electron and hole effective mass of Ge is applied in the simulation for $Ge_{1-x}Si_x$ with $x < 0.03$. The optical transition matrix element is expressed as a contribution of light hole, heavy hole, and split orbit energies.

$$E_p = 3\left(\frac{m_0}{m_e^{\Gamma}} + 1\right)\left(\frac{1}{E_g^{\Gamma,lh}} + \frac{1}{E_g^{\Gamma,hh}} + \frac{1}{E_g^{\Gamma,SO}}\right) \quad \text{Eq. 5.19}$$

5.2 Modulation model of GeSi modulator array

The modulation model of the GeSi modulator arrays was built to predict the device performance of all the modulators with various compositions, waveguide widths, and stressor layers. The model was built using Wolfram Mathematica. The parameters defined and used in the model are listed in Table 5.1.

Table 5.1 Parameters in the modulation model

Parameters	Definition	Unit
Independent Variables		
Fon	Electrid field at 0V with Ge on Si	V/m
Foff	Electrid field at off state, various voltage	V/m
Egl	bandgap of light hole at strained state	eV
Egh	bandgap of heavy hole at strained state	eV
Materials Constants		
e	electron charge	C
Ep	constant for transition matrix element of Ge	eV
nr	real part of refractive index	
c	speed of light	m/s
ε0	vacuum permitivity	F/m
m0	electron mass	kg
h_bar	planck constant	J*s
Dependent Variables		
mrl	reduced mass of light hole	kg
mrh	reduced mass of heavy hole	kg
lambda	incident wavelength	nm
ω	angular frequency	1/s
hFlon	transition energy for light hole at on state	J
hFhon	transition energy for heavy hole at on state	J
hFloff	transition energy for light hole at off state	J
hFhoff	transition energy for heavy hole at off state	J
ηlon		unitless
ηhon		unitless
ηloff		unitless
ηhoff		unitless
Alon	airy function for light hole transition at on state	unitless
Ahon	airy function for heavy hole transition at on state	unitless
Aloff	airy function for light hole transition at off state	unitless
Ahoff	airy function for heavy hole transition at off state	unitless
derivAlon	first derivative of airy function for light hole transition at on state	unitless
derivAhon	first derivative of airy function for heavy hole transition at on state	unitless
derivAloff	first derivative of airy function for light hole transition at off state	unitless
derivAhoff	first derivative of airy function for heavy hole transition at off state	unitless
AlphaOn	Absorption at on state	1/cm
AlphaOff	Absorption at off state	1/cm

Three kinds of parameters were classified in the model: (1) independent variables, (2) materials constants, and (3) dependent variables. The independent variables include the electric fields applied in the vertical direction of the modulator and the energy bandgap of the light hole and heavy hole bands. The light hole and heavy hole bandgap values are inputted from the strain engineering model and validified in the photoreflectance measurements for Ge and GeSi film composition and biaxial strain, and in the micro-Raman measurements on the Ge and GeSi waveguide structures for the strains along the waveguide axes as reported in Chapters 2 and 4. The electric field intensity values as a function of the applied voltage across the electrodes are inputted

from the electric field transient model in Chapter 3. As plotted in Figure 5.2, the Ge and $Ge_{0.99}Si_{0.01}$ modulators have the built-potential of about 10 kV/cm. The applied voltage linearly increases the electric field across the waveguide modulator in the vertical direction. The electrical field has a uniform distribution along the field direction, which is critical for high-performance electroabsorption modulators. The materials constants applied in the model include transition matrix elements, refractive indices, electron masses of Ge, and $Ge_{0.99}Si_{0.01}$ materials. These values are determined via the linear interpolation of the Ge and Si valuated reported in the literature. The dependent variables include terms, such as reduced masses of the light hole and the heavy hole, transition energies for the light hole, and the heavy hole at various modulation states and others. Those values are calculated based on the equations introduced in the first section. In the end, the absorption coefficients at different modulator states are obtained as a function of incident light wavelength.

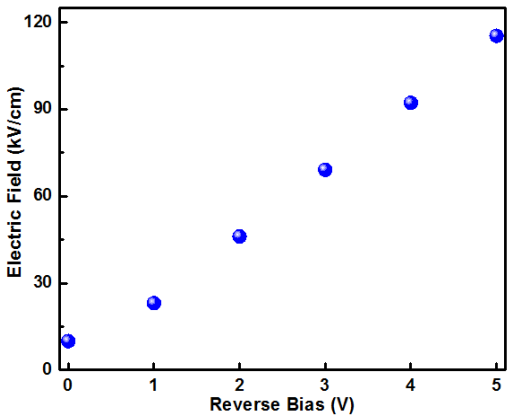

Figure 5.2 Electric field intensity as a function of reverse bias for Ge electroabsorption modulators with the electric field direction along the vertical z-direction.

The absorptions of the Ge and $Ge_{0.99}Si_{0.01}$ modulator arrays are modeled under various conditions. The extinction ratios are obtained as the difference between absorptions at modulators

on and off states. As a demonstration of the modulation performance, the extinction ratios are modeled based on the electric field difference between 40 kV/cm and 10 kV/cm. It corresponds to the applied voltage of less than 3 V. The actual electric field intensities and amplitudes of the extinction ratios would be limited by the actual device fabrications and materials electrical and optical qualities. Therefore, these modeled intensities and amplitudes serve as relative comparisons. It is more important to model and evaluate the positions of the ER peaks for various waveguides under the effect of a compressive/tensile stressor. As shown in Figure 5.3 (a), a Ge modulator array under 1 GPa compressive stressor shows a consistent shift of ER peaks toward higher modulation wavelength (from 1530 nm toward 1580 nm) as the modulator waveguide width increases from 400 nm toward 4 um. The effect of the compressive stressor expands the bandgap and shifts the modulation peak toward a lower wavelength. Meanwhile, the narrower waveguide shows a more distinctive strain effect in the modulator waveguides. The tensile stressor, on the other hand, applies the strain effect in the opposite direction. As shown in Figure 5.3 (b), the 0.6 GPa tensile stressor pushes the ER peaks toward higher modulation wavelength. Only 4 um and 2 um wide Ge waveguide modulators show the ER peaks in the modeled optical window from 1510 nm to 1610. Other waveguide modulators have the modeled ER peak too much toward higher wavelength beyond 1610 nm.

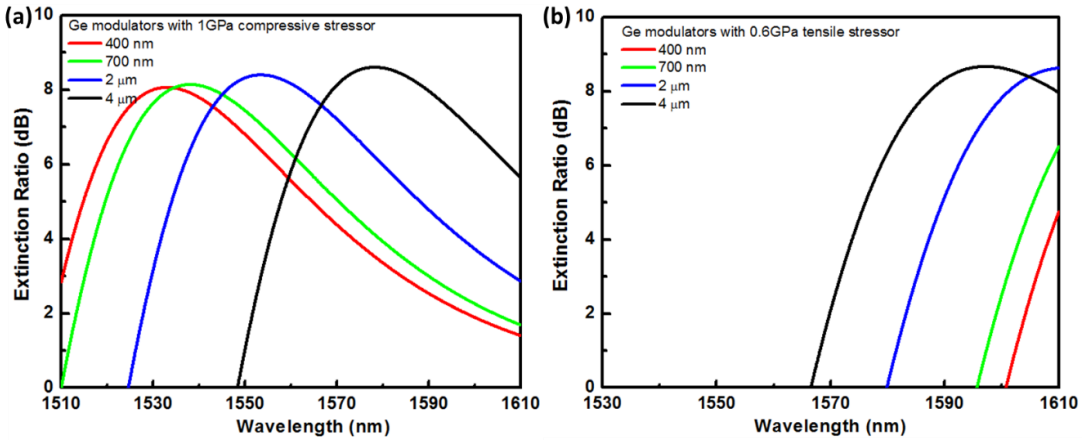

Figure 5.3 Simulated extinction ratio as a function of incident light wavelength for Ge electroabsorption modulator arrays under (a) 1 GPa compressive stressor, and (b) 0.6 GPa tensile stressor as a function of the waveguide modulator width.

A similar strain-coupled FK effect is observed in $Ge_{0.99}Si_{0.01}$ modulators. As shown in Figure 5.4 (a), a $Ge_{0.99}Si_{0.01}$ modulator array under 1 GPa compressive stressor shows the effect of the compressive stressor to expand the bandgap and shift the modulation peak toward lower wavelength. The inclusion of 1% Si already shifts the modulator ER peak toward a lower wavelength. Further reduction of the modulator waveguide width shifts the modulator ER peaks too much toward the wavelength region lower than 1510 nm. Hence, the modeled optical window is shifted to be 1450nm-1550nm to capture the ER peaks for compressively strained $Ge_{0.99}Si_{0.01}$ modulators. The tensile stressor, on the other hand, applies the strain effect in the opposite direction. The application of a 0.6 GPa tensile stressor shows a consistent shift of the modulation ER peaks for $Ge_{0.99}Si_{0.01}$ waveguide modulators from 400 nm width toward 4 um width.

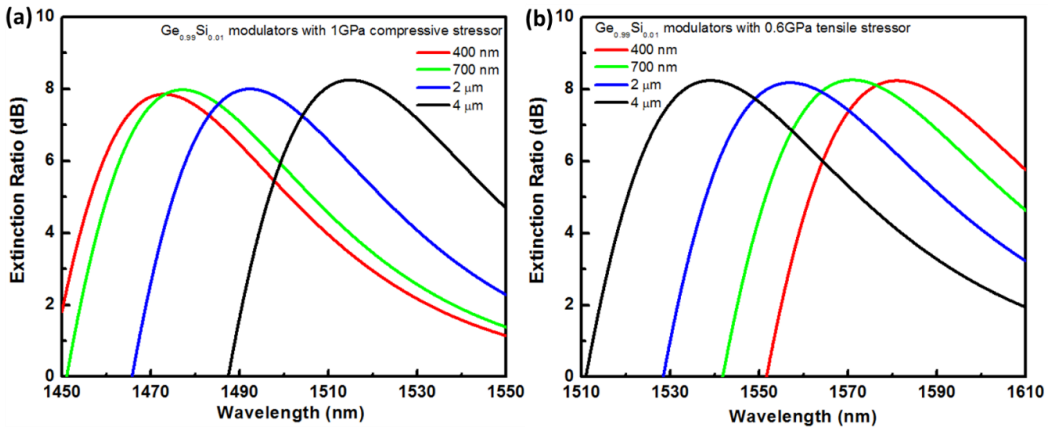

Figure 5.4 Simulated extinction ratio as a function of incident light wavelength for $Ge_{0.99}Si_{0.01}$ electroabsorption modulator array under (a) 1 GPa compressive stressor, and (b) 0.6 GPa tensile stressor as a funcition of the waveguide modulator width.

Based on the modulation model results for the Ge and $Ge_{0.99}Si_{0.01}$ modulator arrays with stressor layers, the Ge modulator array with 1 GPa compressive stressor, and the $Ge_{0.99}Si_{0.01}$ modulator array with 0.6 GPa tensile stressor, show the modulation ER peaks in the optical window from 1510 nm to 1610 nm for all waveguide modulators. Both compressively and tensile strained modulator arrays have shown significant optical window broadening to ~100 nm based in the simulation results. That successfully demonstrates the innovation of Ge and GeSi electroabsorption modulator arrays with a simplified design layout for modulators to cover a broad optical range. Although each waveguide modulator experiences different induced strain, the modulator array is designed with one layout, and various waveguide dimensions are fabricated at the same time. The devices of the Ge electroabsorption modulator array with 1 GPa compressive stressor and the $Ge_{0.99}Si_{0.01}$ modulator array with 0.6 GPa tensile stressor were fabricated and tested to compare the modulation model results and experimental results from the device performance characterization in the later chapters.

Chapter 6 Process Flow Development

6.1 Process flow development of Ge and GeSi modulator arrays

The strained Ge and GeSi modulator arrays were fabricated using the tools in MIT Nano, the MIT Substrate Engineering Lab, and the Harvard Center for Nanoscale System Cleanroom Facilities. The detailed process flow development is discussed in this Chapter, as shown in the process flow chart. Multiple waveguide modulators are simultaneously fabricated in the same process flow to achieve the modulator array. The fabrication steps are CMOS-compatible and can be readily implemented into a foundry fabrication.

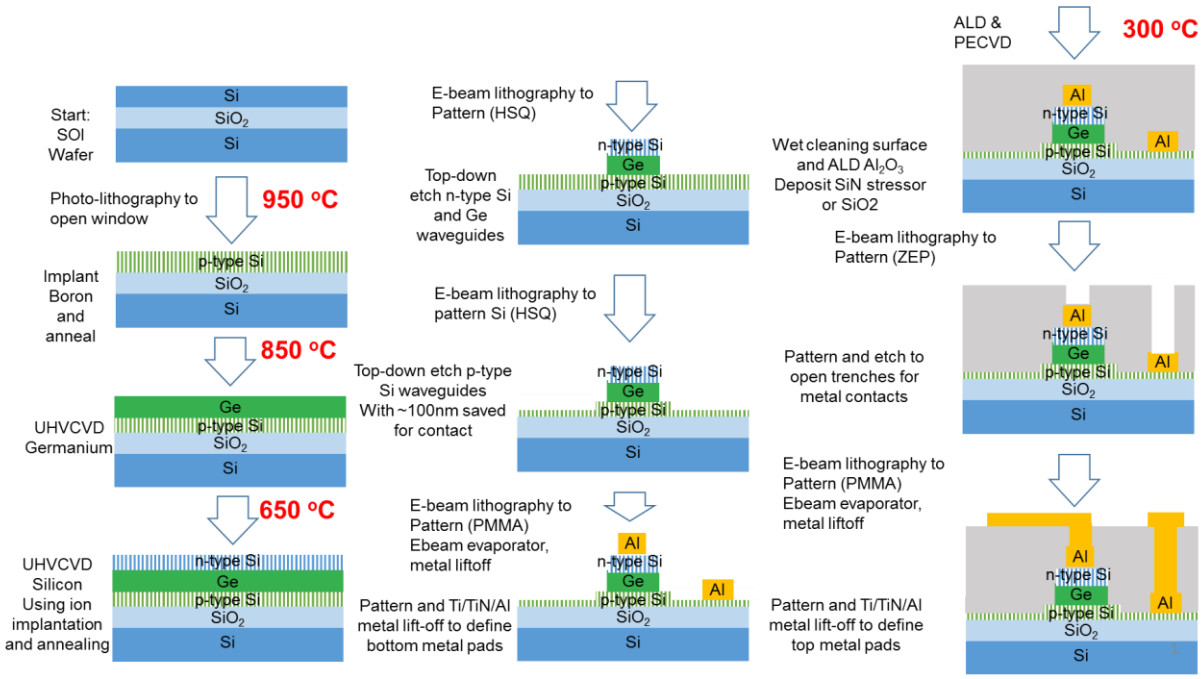

Figure 6.1 Complete process flow for Ge and GeSi electroabsorption modulator arrays

Prime 250nm Si on 3μm SiO_2 insulator wafers were cleaned via RCA at the beginning of the process. Boron implantation was performed on the SOI wafers using the implantation conditions

as simulated in Chapter 3 to achieve a dopant concentration of ~ 10^{20} cm^{-3}. A post-implantation annealing was performed to activate all the dopants in the Si layer of the SOI wafers. The top shadow oxide was used only to control the doping depth into the layer, and was removed by soaking in the buffered oxide etchant (BOE) for 3 minutes. A standard RCA cleaning was performed on the wafers with an extra 1 minute soaking in the dilute HF (50:1 of HF:H_2O) for the Si surface passivation, followed by the spin-drying. The wafers were immediately loaded in the UHVCVD system for the epitaxial growth of Ge or $Ge_{0.99}Si_{0.01}$ on the SOI substrates. Details on the growth mechanisms and conditions are discussed in Chapter 2. Cyclic annealing was performed at the end of the epitaxial growth process to reduce the threading dislocation density. The top Si layer was grown on the Ge or $Ge_{0.99}Si_{0.01}$ on the SOI layers in the same UHVCVD system without breaking the vacuum in between the growth steps to ensure the intact interface between the layers. The top Si layer was not doped during the growth. The phosphorous was implanted with subsequent thermal annealing to provide an n-type Si top contact layer. The as-grown wafers with the top 100 nm shadow oxide were then die-sawed into 1.5 by 2.0 cm dies with the surface protection of 1 um thick post-based SPR photoresist. The dies were soaked and sonicated in the acetone solution for 5 minutes and then in isopropyl alcohol (IPA) solution for 5 minutes to remove the polymer-based surface protection layer in the MTL solvent benches. The cleaned dies were stored in cleanrooms for further processing. The top oxide layer was removed via soaking in BOE for 3 minutes only before the chip processing to prevent surface degradation.

Table 6.1 Processing and characterization steps in the modulator array fabrication

Step #	**Process details**
1	Start with SOI wafers, RCA wafer cleaning
2	Shadow oxide deposition in PECVD
3	Boron ion implantation
4	Boron ion activation in annealing tube
5	Shadow oxide removal in BOE, and RCA wafer cleaning
6	Ge or GeSi epitaxial growth in UHVCVD
7	Cyclic annealing in UHVCVD
8	top Si undoped layer growth in UHVCVD
9	Shadown oxide deposition in PECVD
10	Phosphorous ion implantation
11	Phosphorous ion activation in annealing tube
12	Die-saw the wafers
13	Remove SPR diesaw protective layer in organic solvents
14	Romove top oxide layer in BOE
15	Coat HSQ ebeam resist on chips
16	E Beam lithography for Ge and GeSi waveguide fabrication
17	Develop HSQ patterns
18	Inspect HSQ pattern dimensions and thickness
19	Conditioning RIE chamber via O2 plama cleaning
20	Ge waveguides etching in RIE via HBr chemistry
21	Confirm etching depth in AFM, Ge and Si etched interface in FIB
22	Keep etched HSQ patterns on the waveguides

23	Coat a new HSQ on chips
24	E Beam lithography for Si waveguide alignment and fabrication
25	Develop HSQ patterns
26	Inspect HSQ patterns dimensions, alignments, and thickness
27	Conditioning RIE chamber via O2 plama cleaning
28	Si ridge waveguides etching in RIE via HBr chemistry
29	Confirm etching depth in AFM, ensure 80nm Si unetched
30	Remove HSQ patterns in BOE
31	Electrical characterization on the doped Si contacts
32	Coat PMMA ebeam resist on chips
33	E Beam lithography for first metal lift-off
34	Develop PMMA patterns
35	Inspect PMMA patterns dimensions, alignments, and thickness
36	Remove organic residue via asher in oxygen
37	Deposit metals in Ebeam evaporator
38	Lift off metal pads in hot NMP solvent
39	Inspect the first metal patterns and alignment in microscopes and SEM
40	Remove organic residue via asher in oxygen
41	Deposit Al2O3 in ALD
42	Deposite stressor layers
43	Chip surface cleaning in solvents
44	Coat ZEP ebeam resist on chips
45	E Beam lithography for contact trench opening
46	Develop ZEP patterns in ZED

47	Inspect ZEP pattern dimensions, alignments, and thickness
48	Conditioning RIE chamber via O2 plama cleaning
49	Contact trenching etching in RIE via CHF3 and CF4 chemistry
50	Confirm etching depth in AFM and FIB
51	Remove ZEP patterns in hot NMP
52	Coat PMMA ebeam resist on chips
53	E Beam lithography for second metal lift-off
54	Develop PMMA patterns
55	Inspect PMMA patterns dimensions, alignments, and thickness
56	Remove organic residue via asher in oxygen
57	Deposit metals in Ebeam evaporator
58	Lift off metal pads in hot NMP solvent
59	Inspect the second metal patterns and alignment in microscopes and SEM
60	Electrical characterization on the metal contacts
61	Cleave at tapered position
62	Mount the chip on testing stage

Several rounds of lithography, alignment, and patterning were performed in the device fabrication flow. The top Si waveguides and Ge and GeSi modulator waveguides were processed first. An H-SiO_x (HSQ) electron-beam photoresist was used in the electron beam lithography. The photoresist was spin-coated and maintained a layer thickness of 120nm. The electron dosage was optimized for the minimal lithography feature size of less than 100 nm within a reasonable pattern writing time. The HSQ patterns were developed in a 24% Tetramethylammonium hydroxide

(TMAH) solution for 1 minute and 15 seconds. The development time is critical and closely related to the target feature sizes of the device. The developed features were evaluated under the microscope to ensure the successful development of the patterns before the etch step. The reactive ion etching was performed using a Hydrogen Bromide (HBr) etching chemistry. Due to the chemical and crystallin similarity of Ge and Si, there was no etch stops between the Si and Ge layers. Therefore, the timed etching and controlled etching profiles were monitored via AFM characterization. The etch rates were about 3 nm/sec and 4 nm/sec for Si and Ge layers, respectively. The 400nm top Si and 300 nm Ge or GeSi layers were etched down, with the total etching time of ~ 3 minutes and 20 seconds. The dry etching tool chamber condition varied for each etch, even with a standard pre-etching chamber cleaning step using oxygen plasma etching for 20 minutes. Therefore, the etched step height was monitored using AFM each time on every chip. The AFM characterization gives a height precision of several nanometers. The cross-sectional SEM characterization with Focused Ion Beam (FIB) milling was also used to check one of the chips in each batch to ensure the etching profile shown in Figure 6.2 (a).

Similar alignment, lithography, and patterning round were done for the bottom Si ridge waveguide fabrication. The only difference in this round was the etching depth of the Si waveguide, which was 170 nm down into the bottom Si layer and left 80 nm un-etched as the bottom contacting layer for the electrodes. As shown in Figure 6.2 (b), the alignment of the Ge or GeSi waveguide on the Si waveguide has an accuracy of ~ 20 nm, which is acceptable based on the optical transmission model discussed in Chapter 3. Spin coating of the HSQ on the etched Si on Ge waveguides was challenging. Coating sufficiently thick HSQ on top of the 700nm tall, sub-micrometers wide waveguides does not have a high yield. Therefore, the as-etched top HSQ from the first round of patterning was saved to ensure a sufficiently thick HSQ pattern, which prevented etching of the top

waveguides during the second round of the etching. One more layer of HSQ was spin-coated on the chip and developed to form the surface pattern for the Si ridge waveguides. The modulator waveguide tapers were fabricated and aligned on the underneath Si waveguides for efficiently light coupling, as shown in Figure 6.2 (c).

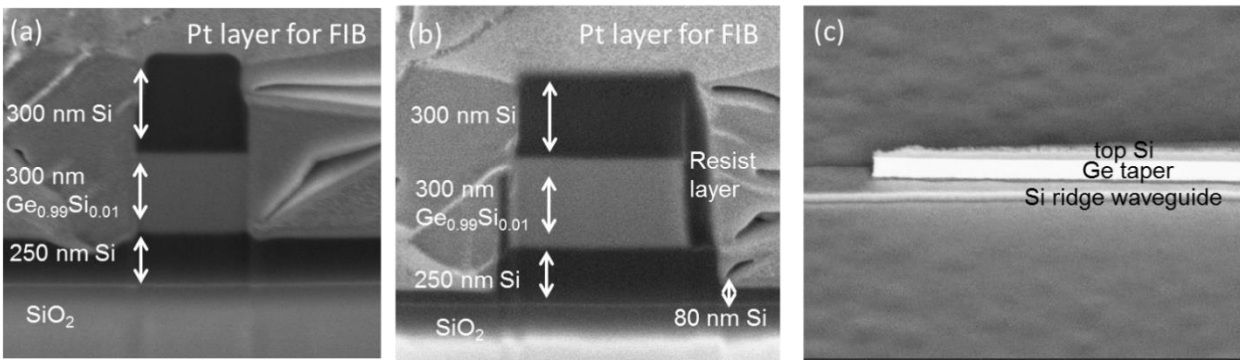

Figure 6.2 Cross-sectional SEM images of (a) etched GeSi waveguide, (b) etched and aligned GeSi waveguide on Si ridge waveguide, and (c) modulator waveguide taper with tilted side view.

After the first two rounds of patterning, the chips were cleaned via soaking in BOE for 3 minutes to thoroughly remove the SiO_2 based ebeam photoresist. Oxygen plasma etching was performed to remove the organic residues on the chip. The third round of the alignment, lithography, and patterning involves the usage of a negative polymer-based photoresist to conduct the metal lift-off process for the first layer of the metal contacts. Polymethyl Methacrylate (PMMA) photoresist was spin-coated on the chip and patterned via the ebeam lithography. The solution of Methyl Isobutyl Ketone (MIBK) and IPA was applied to develop the features, which were open windows for the metal contacts. 20 nm Titanium (Ti), 20 nm Titanium Nitride (TiN), and 180 nm Aluminum (Al) were deposited in sequence via the electron beam evaporator. The chips were continuously rotated planarly to ensure the uniform deposition of the metals. The Al metal deposition rate was

set to be 2 A/sec. A lift-off process was performed by soaking the chips in the 80 ^{o}C hot N-Methyl-2-pyrrolidone (NMP) solvent for 10 minutes and gently stir the hot solution until the dissolution of the PMMA layer and peeling off of the un-patterned metal layer. As shown in Figure 6.3, the patterned metals were well aligned on top of the Si contact for the top contact region, and on the bottom Si layer with the controlled gap between the edge of the waveguide modulator and the bottom metal electrodes, as compared to the electrode design in Chapter 3.

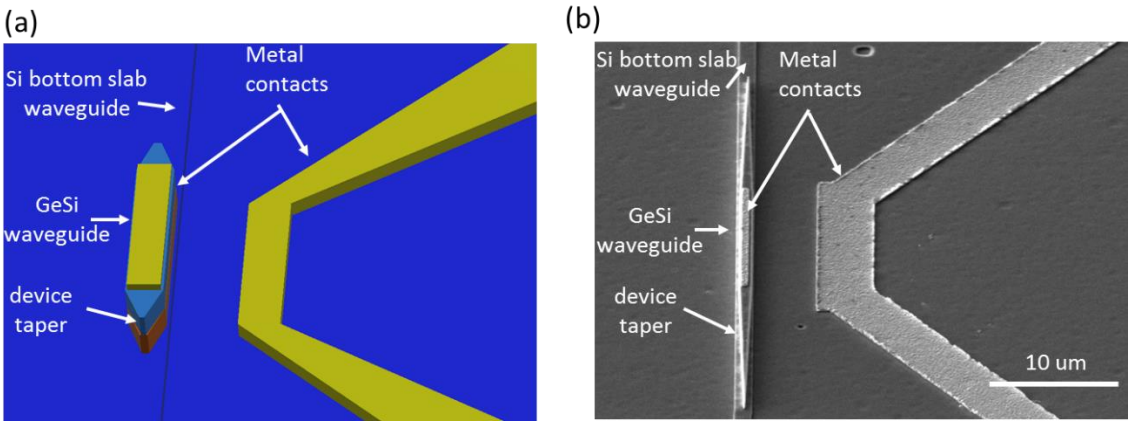

Figure 6.3 (a) schematic of metal contacts design, (b) SEM view of the fabricated metal contacts.

The modulator waveguide structures were fabricated after the three rounds of the alignment, lithography, and patterning. The SiN_x stressor layer was deposited to apply strain in the modulators. A dual-frequency PECVD process was used to control the intrinsic stress of the deposited layer. X-ray reflectance measurements were performed to monitor the deposited films with the processed chips. Before each PECVD deposition, the chips were surface cleaned via the oxygen plasma ashing for 5 minutes, followed by a 5 nm Al_2O_3 conformal layer deposition using an Atomic Layer Deposition (ALD) tool. Two sets of samples were prepared on Ge and GeSi modulator array. One batch had a 1 GPa compressive stressor, and the other one had a 0.6 GPa tensile stressor. The challenge and solution to the stressor adhesion are discussed in section 6.3.

After the stressor deposition, the trenches were opened on top of the metal contact and next to the modulators to provide windows for the linkage of the electrodes and metal pads High-resolution ZEP ebeam photoresist was spin-coated on the chip to form the resist thickness of 400nm. ebeam lithography was conducted, followed by the pattern development in the ZED. The trench etching was performed in the same RIE tool with the etch chemistry of Carbon Tetrafluoride (CF4) and Trifluoromethan (CHF3). AFM characterization was used to ensure the complete etching through of the stressor layer. The nitride stressor layer etching rate was ~ 3 nm/sec. Finally, the last round of alignment, lithography, and patterning was performed on the second metal electrode layer fabrication to connect the modulator contacts to the GSG electrode pads on the chip. The process was similar to the first metal layer fabrication using the PMMA photoresist, eBeam evaporation of the metals, and metal lift-off procedure. The metal contacts were linked with the GSG pads, as shown in Figure 6.4 (a) & (b). It was observed that the second metal layer lift-off process had a low yield due to the large aspect ratio between the trench depth and width. In the standard foundry process, tungsten vias are commonly used to contact the different metal layers with a large trench depth to trench width ratio. Unfortunately, the tungsten via deposition was not available in the MIT cleanroom facilities. For the samples with a loose connection at the top metal contact regions on the modulators, the Pt patterning and deposition process was performed in the FIB tool to intentionally deposit and fill metal into the trenches. That ensured the successful electrical connection between the top metal pads and modulators' top contacts. The metal contacts were sintered at 400 ^{o}C for 30 seconds via Rapid Thermal Annealing (RTA). The electrical current and voltage measurements were done on the modulators' contact pads to ensure the good electrical quality of the contacts.

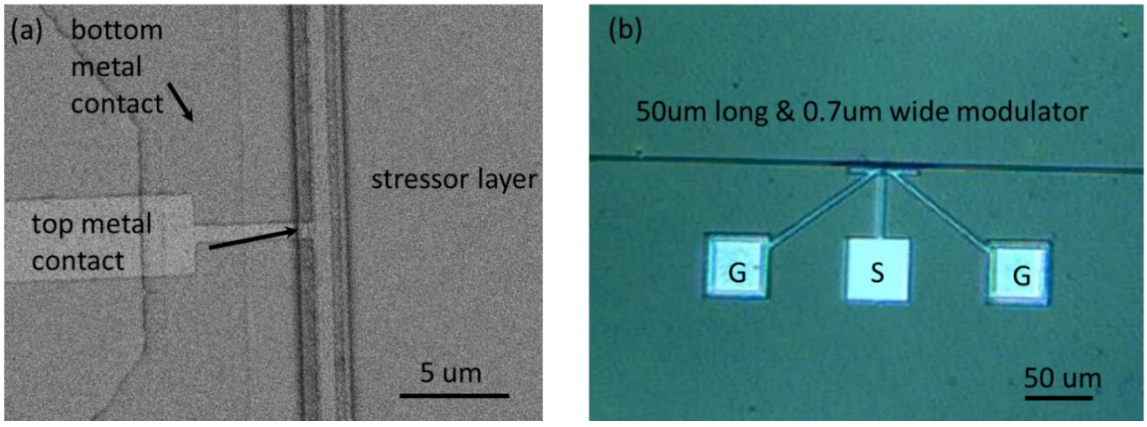

Figure 6.4 (a) The FIB of one of the contact pad with the titled view, (b) opical image of the top view of the GSG pads.

6.2 Thermal constraints in the processing

The thermal constraints in the device fabrication are prioritized in the process flow design. A thermal budget evaluation is conducted in the process flow design, as shown in the red highlights in Figure 6.1. The guideline of the thermal budgeting is to keep the high-temperature processing at the front end of the line. The high-temperature processing steps on (1) Ge and GeSi epitaxial growth, (2) Si growth on Ge or GeSi epitaxial layer, (3) implanted dopants activation. The concerns related to these steps are unwanted alloying at the Si and Ge interface and dopant interdiffusion across the epitaxial layers. The highest temperature in these steps is the boron dopants activation at 1000 ^{o}C for 30 minutes on the SOI wafers. After that, the following high-temperature step is the cyclic annealing up to 850 ^{o}C. The growth temperature of the top Si layer is constrained by the Ge and Si alloying limitation. That growth temperature is set to be 650 ^{o}C with the low-temperature buffer growth at 500^{o}C taking into account the higher decomposition temperature of the reactive silane gas compared to that of the germane reactive gas, as shown in Figure 6.5 of the comparison between the 650^{o}C growth and 800^{o}C growth of the top Si layer. The phosphorous dopant activation

is carried out at 650°C for 30 minutes, which fully activates the dopants and causes minimal interdiffusion of the n-type and p-type dopants across the layers. The low-temperature processing steps on the back-end-of-line are the stressor deposition at 300°C via PECVD, and the Al_2O_3 deposition at 250°C via ALD, and the metal contact rapid annealing at 400^0C via RTA. The device structures, electrical properties, and optical properties are characterized during processes and on the final devices to validify the process flow.

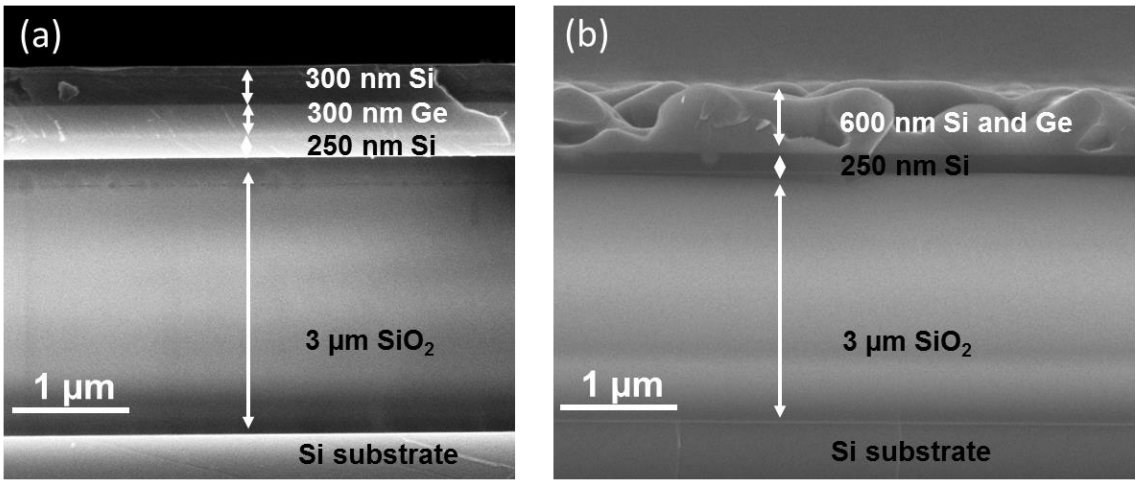

Figure 6.5 As-grown Si on Ge layers at the top Si growth temperature of (a) 650°C and (b) 800°C. The unwanted Ge/Si alloying was observed for the 800°C grown sample.

6.3 Treatment for stressor layer adhesion improvement

It is essential to perform the ALD treatment to enhance the surface passivation for the electrical performance of the modulators and, more importantly, for the adhesion improvement of the stressor layers. It is observed in the early samples, also with the samples done by Dr. Yiding Lin for his strained Ge on insulator photodetectors. The stressor layer detaches from the modulator sidewall due to the high tensile stress (0.6GPa). That challenge is resolved by applying a thin ALD aluminum oxide layer as an adhesion layer to attach the stressor in place. Meanwhile, small

windows are opened on top of the waveguide structures to link the top electrodes, instead of using planarization via Chemical and Mechanical Planarization (CMP), which causes extra vibration and stress at the SiN_x and modulator sidewall interface and degrades the stressor effect. The modulators show a stable and sufficient strain effect in the modulator waveguide, as shown in the cross-sectional SEM image in Figure 6.6.

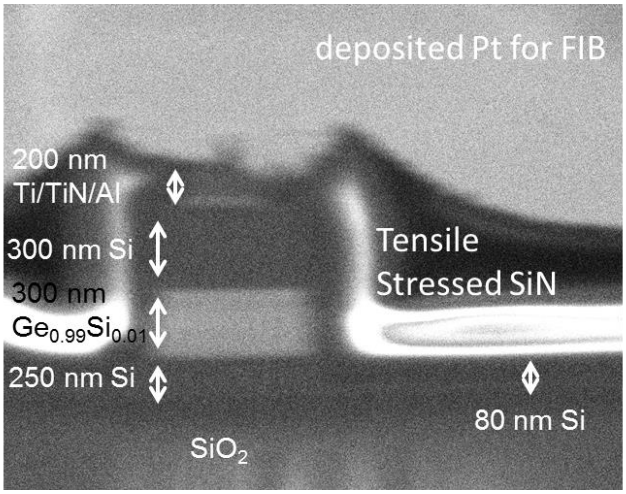

Figure 6.6 Cross-sectional SEM image of the $Ge_{0.99}Si_{0.01}$ tensile strained modulator with the successfully adhesive stressor at 0.6 GPa tensile.

Chapter 7 Optical transmission without DC bias in Ge and GeSi modulator arrays

This Chapter discusses the experimental results on the optical transmission measurements without the applied electric field. The optical transmission characterization was conducted on the Ge, $Ge_{0.99}Si_{0.01}$, and $Ge_{0.97}Si_{0.03}$ modulator arrays with and without stressors. The modulator absorption edge is correlated with the materials composition, waveguide dimensions, and stressors. Absorption edge values are extracted through fitting the optical transmission spectra using the model developed in Chapter 6. It is noteworthy to mention that the evaluated Ge and $Ge_{0.97}Si_{0.03}$ modulators do not have the last metal layer deposited on top of the Si contact due to fabrication limitation. The top metal layer is completed in all the $Ge_{0.99}Si_{0.01}$ modulators. Loss mechanisms are analyzed to distinguish the loss contributions among the device design and fabrication. Solutions are proposed for device optical transmission improvements.

7.1 Experimental procedure and setup

Optical transmission measurements at the modulator on-states (0V bias) are conducted using a tunable laser and detector for a wavelength range from 1510 to 1610 nm, as shown in the testing stage schematic in Figure 7.1. The edge coupling stage with lensed fiber on both sides is used to align and couple light in and out of the waveguide modulator. During the coupling alignment, an infrared (IR) camera is used to align the input fiber with the input waveguide. Once the bright mode spot is observed on the IR camera, the input end alignment is completed. The output end is aligned via monitoring the output signal power using the power meter connected to the output fiber. The overall alignment is optimized by maximizing the output power. Reference waveguides, Si ridge waveguides (250nm tall with 80nm unetched) on SiO_2 substrate with the same width of the sampled waveguide modulators, which are identical with the ones used for the modulators. The waveguide

loss is then measured. The transmission measurements are then conducted for all modulators. The difference of the transmission is taken to evaluate the optical insertion loss of the strained modulator arrays. The 400nm width waveguide Ge modulator shows a low insertion loss of less than 1dB. The wider waveguides show more considerable insertion loss, which is expected because the taper dimensions are optimized for narrow waveguides. More optimization is needed via design and experimental result correlation to further reduce the insertion loss of the wide waveguide modulators.

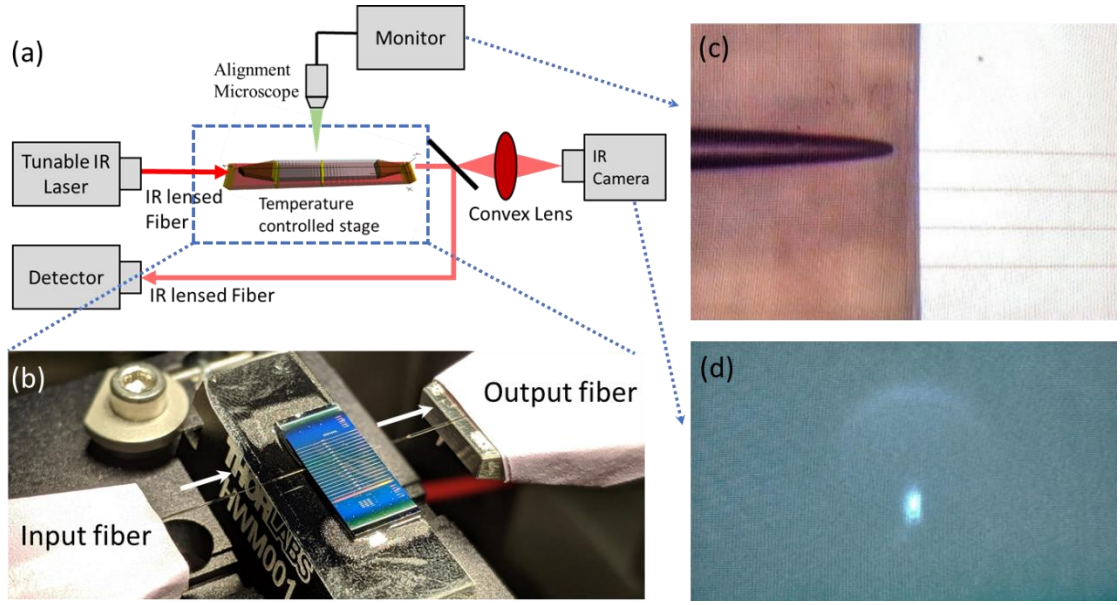

Figure 7.1 (a) schematic of edge coupling stage for optical transmission measurement. (b) close up view of the lensed fiber and chip alignment. (c) microscopic view of the fiber and waveguide edge alignment. (d) optical mode image on the IR camera for alignment.

7.2 Optical transmission spectra without DC bias

The optical transmission characterization is an essential step to evaluate the device's optical transmissive quality in terms of its insertion loss and optical bandwidth. Without a DC bias application, a spectrum shows an optical transmission edge. That indicates the region of interest for an electroabsorption modulation. A shift in the optical transmission spectra indicates a change in the waveguide modulator absorption edge in response to the composition and strain engineering, which is critical to evaluate and compare the strain effect in simulation and actual device performance. The Ge, $Ge_{0.99}Si_{0.01}$, and $Ge_{0.97}Si_{0.03}$ modulators are evaluated with various waveguide widths from 0.4nm to 4um, and with three sets of stressor layers: (1) 1.0 GPa compressive stressor, (2) 0.6 GPa tensile stressor, (3) no stressor, as plotted in Figure 7.2. In the case of the 1.0 GPa compressive stressor, the compressive strain induced in the waveguide modulator expands the direct bandgap as simulated in the strain engineering model. It hence shifts the absorption edge to the lower wavelength region. The fabricated waveguide modulators show various optical transmission spectra with the same 1.0 GPa compressive stressor. The narrower waveguide modulator shifts the absorption edge to the lowest wavelength, compared to the wider waveguide modulator with the same compressive stressor. That makes sense since the wider waveguide is less responsive to the external stressor effect. In the case of the 0.6 GPa tensile stress, the tensile strain induced in the waveguide modulator shrinks the direct bandgap as observed in the strain engineering model; therefore, it shifts the absorption edge to a higher wavelength range. The similar difference between the narrow and wide waveguide modulators is obtained to indicate a larger strain effect in the narrower waveguide. As for the case without the stressor layer, the absorption edge was not shifted to either direction. There is a change in the insertion loss for the waveguide modulators with different widths. The general trend observed is that the wider

waveguide is lossier compared to the narrower waveguide. This might be due to multiple reasons, which are discussed in a later section of this Chapter. The optical measurement window is limited from 1510nm to 1610nm due to to the available testing setup. Some optical transmission spectra do not cover the full absorption edge because it is in the wavelength range higher than 1610nm or lower than 1510nm. Detailed absorption edge information is extracted and analyzed in the next section using the generalized FK model.

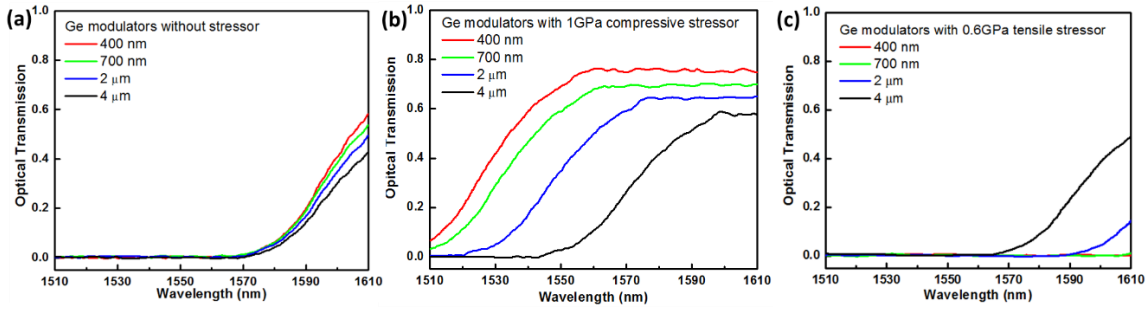

Figure 7.2 Ge waveguide modulators with (a) no stressor, (b) 1.0 GPa compressive stressor, (c) 0.6 GPa tensile stressor.

The device structure difference between the Ge and $Ge_{0.99}Si_{0.01}$ modulators is the presence of the top metal contacts in the $Ge_{0.99}Si_{0.01}$ modulators, while Ge modulators only have top Si contacts. The presence of the top metal contacts should have minimal effect in the optical transmission spectra as simulated in the mode solution for the device contact design. The top Si layer should be thick enough to minimize the metal absorption from the top metal contact. However, the measured optical transmission of the $Ge_{0.99}Si_{0.01}$ modulators shows much lower optical transmission values (larger insertion loss) compared to the Ge modulators. That indicates an insufficient top Si thickness to prevent metal absorption. The amount of metal-induced absorption is analyzed in the later section of this Chapter.

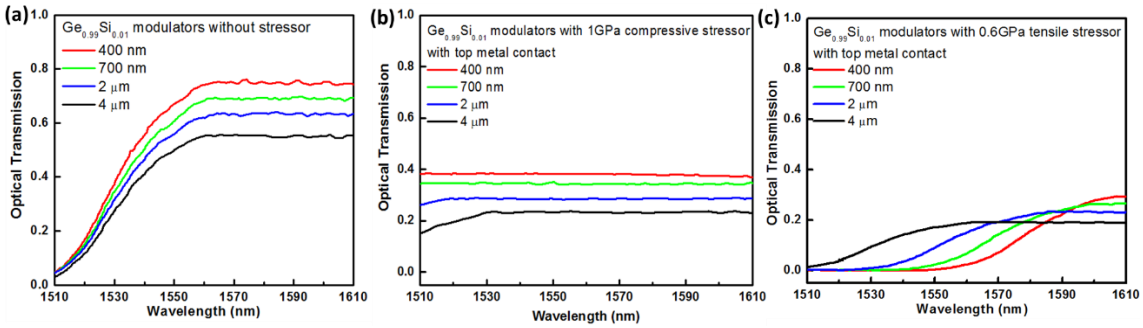

Figure 7.3 $Ge_{0.99}Si_{0.01}$ waveguide modulators with (a) no stressor, (b) 1.0 GPa compressive stressor, (c) 0.6 GPa tensile stressor.

For the GeSi modulators with 3% Si inclusion, the relatively high Si concentration expands the bandgap and shifts the absorption edge below the 1510nm measurement limit. Therefore, the spectra measured for $Ge_{0.97}Si_{0.03}$ show no absorption edge in the optical testing window for all $Ge_{0.97}Si_{0.03}$ modulators with various stressors. That makes it challenging to extract useful band information from the optical transmission curves without the DC bias. More band information for the $Ge_{0.97}Si_{0.03}$ waveguide modulators is extracted by analyzing their optical transmission curves with the DC bias in Chapter 9.

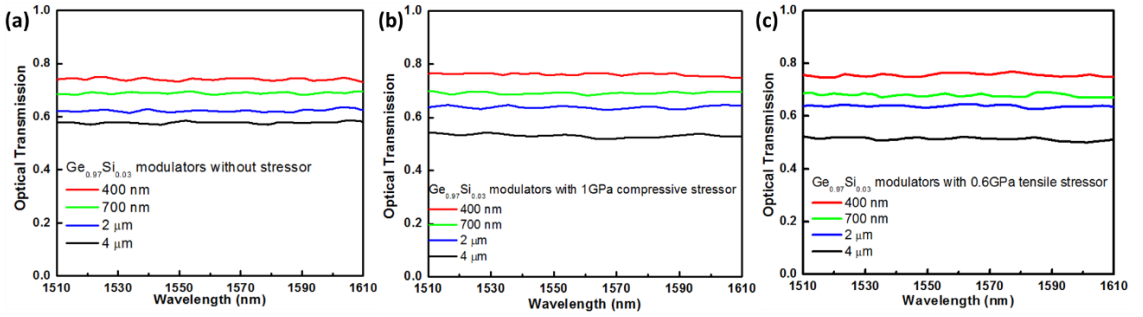

Figure 7.4 $Ge_{0.97}Si_{0.03}$ waveguide modulators with (a) no stressor, (b) 1.0 GPa compressive stressor, (c) 0.6 GPa tensile stressor.

7.3 Bandgap and strain extraction from optical transmission spectrum

The modulation model based on the generalized Franz-Keldysh formulas is applied to fit the optical transmission curves for all Ge and GeSi modulators. The majority of the curves are successfully fitted. Some of the transmission curves are not able to be fitted due to the limited optical testing window. As shown in Figure 7.5, the optical transmissions curves are fitted for waveguide modulators with various dimensions. The absorption spectra can be constructed from the transmission spectra and show a similar FK model fitting of the absorption of the modulators without DC bias.

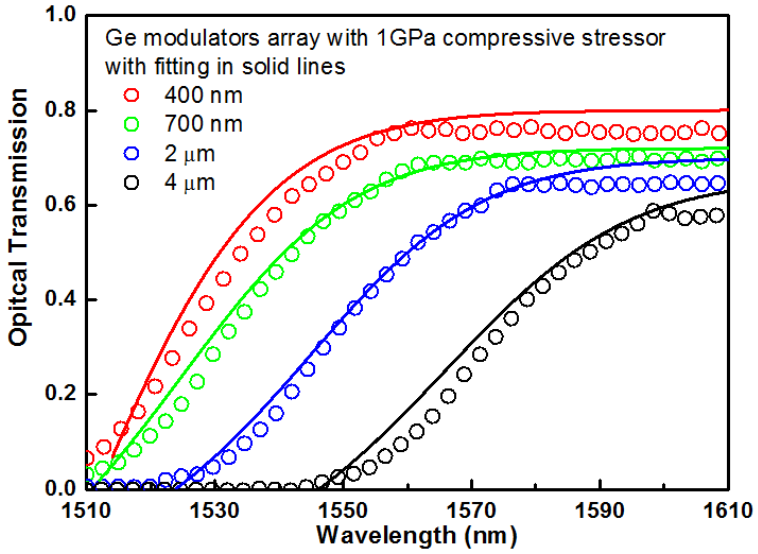

Figure 7.5 Measured and fitted transmission spectra of Ge modulators with 1.0 GPa compressive stressor.

The optical absorption edge values are extracted and compared with the simulated values from the strain engineering model. The compressively strained Ge modulator array shows the absorption edge shift from 1520 nm to 1564 nm. The tensile strained Ge modulator array shows the absorption edges shift from 1585 nm to 1611nm. The compressively strained $Ge_{0.99}Si_{0.01}$ modulator

array shows the absorption edges shift from 1461 nm to 1502 nm. The tensile strained $Ge_{0.99}Si_{0.01}$ modulator array shows the absorption edge shift from 1522 nm to 1571 nm. This wide variation of the absorption edges in Ge and $Ge_{0.99}Si_{0.01}$ strained modulator arrays successfully demonstrates the concept of the one-for-all strained modulator array using the simplified design layout and strain engineering. The tensile strained Ge modulator array is then expected to cover the optical bandwidth from 1570 nm to 1626 nm. The compressively strained Ge modulator array is expected to cover the optical bandwidth from 1505 nm to 1579 nm. The tensile strained $Ge_{0.99}Si_{0.01}$ modulator array will cover the optical bandwidth from 1507 nm to 1586 nm. The compressively strained $Ge_{0.99}Si_{0.01}$ modulator array will cover the optical bandwidth from 1446 nm to 1517 nm. That is the first time reported for the tensile or compressively strained Ge and GeSi modulator arrays to be achieved to wide optical bandwidth beyond 80 nm.

Table 7.1 The comparison between the extracted optical band-edge values and the simulated values in strained Ge and GeSi waveguide modulators.

GeSi composition	Modulator Width (nm)	SiN Stressor (GPa)	Eg_LH (eV)	Eg_HH (eV)	Extracted Absorption Edge (nm)	Simulated Absorption Edge (nm)
Ge	400 - 4000	0.0	0.780	0.780	1590	1580
Ge	400	-1.0	0.853	0.816	1520	1520
Ge	500	-1.0	0.850	0.814	1523	1521
Ge	700	-1.0	0.846	0.813	1525	1524
Ge	1000	-1.0	0.831	0.810	1531	1530
Ge	2000	-1.0	0.823	0.805	1540	1539
Ge	3000	-1.0	0.810	0.799	1552	1549
Ge	4000	-1.0	0.799	0.793	1564	1559
Ge	400	0.6	NA	NA	NA	1641
Ge	500	0.6	NA	NA	NA	1640
Ge	700	0.6	NA	NA	NA	1637
Ge	1000	0.6	NA	NA	NA	1630
Ge	2000	0.6	0.770	0.777	1611	1620
Ge	3000	0.6	0.776	0.780	1598	1607
Ge	4000	0.6	0.782	0.784	1585	1598
$Ge_{0.99}Si_{0.01}$	400 - 4000	0.0	0.815	0.815	1522	1517
$Ge_{0.99}Si_{0.01}$	400	-1.0	0.877	0.849	1461	1460
$Ge_{0.99}Si_{0.01}$	500	-1.0	0.873	0.848	1463	1461
$Ge_{0.99}Si_{0.01}$	700	-1.0	0.865	0.846	1465	1464
$Ge_{0.99}Si_{0.01}$	1000	-1.0	0.871	0.844	1470	1469
$Ge_{0.99}Si_{0.01}$	2000	-1.0	0.862	0.838	1480	1479
$Ge_{0.99}Si_{0.01}$	3000	-1.0	0.849	0.833	1488	1488
$Ge_{0.99}Si_{0.01}$	4000	-1.0	0.836	0.826	1502	1498
$Ge_{0.99}Si_{0.01}$	400	0.6	0.789	0.802	1571	1574
$Ge_{0.99}Si_{0.01}$	500	0.6	0.792	0.804	1566	1572
$Ge_{0.99}Si_{0.01}$	700	0.6	0.793	0.804	1563	1569
$Ge_{0.99}Si_{0.01}$	1000	0.6	0.797	0.807	1555	1563
$Ge_{0.99}Si_{0.01}$	2000	0.6	0.802	0.813	1546	1554
$Ge_{0.99}Si_{0.01}$	3000	0.6	0.809	0.816	1533	1542
$Ge_{0.99}Si_{0.01}$	4000	0.6	0.815	0.820	1522	1533

7.4 Modulator optical loss analysis with design improvements

The optical transmission loss of the waveguide modulator is attributed by serval causes: (1) the material's absorption due to the free carrier absorption and indirect bandgap contributions, (2) the light scattering due to the interfaces, or refractive index inhomogeneity along with the propagation, and (3) the coupling loss. The major causes are proposed as the waveguide material absorption loss due to free carrier absorption, sidewall scattering loss, the modulator device coupling, and the metal contact-induced absorption loss. The optical transmission curves are

converted into the transmission loss plots for the analysis of the insertion loss of various Ge and GeSi waveguide modulators. The stressor application mainly shifted the position of the absorption edge in the transmission curves. The loss components are extracted and listed in Table 7.2.

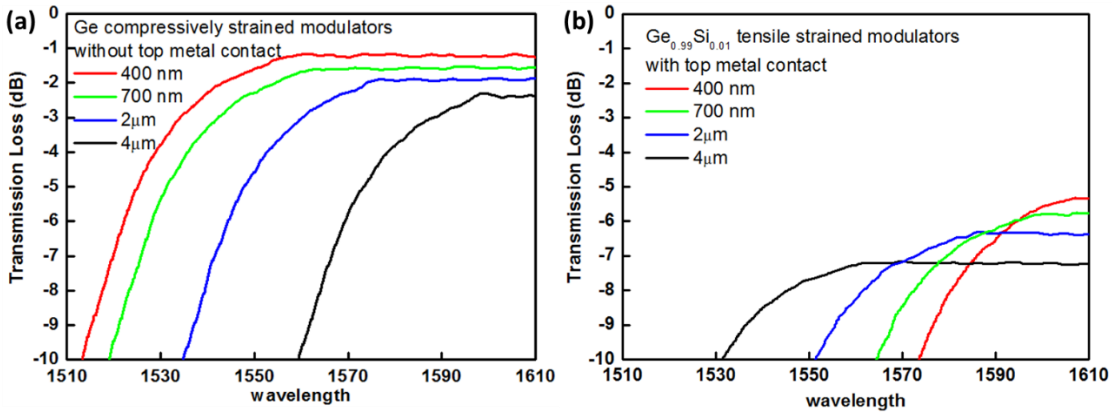

Figure 7.6 Transmission loss in (a) compressively strained Ge modulators, and (b) tensile strained $Ge_{0.99}Si_{0.01}$ modulators.

Table 7.2 Insertion loss values for Ge and GeSi modulators at modulator off-state without DC bias.

GeSi Composition	Modulator Width (nm)	Top metal (Y/N)	Insertion Loss (dB)
Ge	400	N	-1.26
Ge	500	N	-1.49
Ge	700	N	-1.55
Ge	1000	N	-1.82
Ge	2000	N	-1.87
Ge	3000	N	-2.02
Ge	4000	N	-2.39
$Ge_{0.99}Si_{0.01}$	400	Y	-5.34
$Ge_{0.99}Si_{0.01}$	500	Y	-5.49
$Ge_{0.99}Si_{0.01}$	700	Y	-5.77
$Ge_{0.99}Si_{0.01}$	1000	Y	-6.04
$Ge_{0.99}Si_{0.01}$	2000	Y	-6.35
$Ge_{0.99}Si_{0.01}$	3000	Y	-6.83
$Ge_{0.99}Si_{0.01}$	4000	Y	-7.23
$Ge_{0.97}Si_{0.03}$	400	N	-1.26
$Ge_{0.97}Si_{0.03}$	500	N	-1.51
$Ge_{0.97}Si_{0.03}$	700	N	-1.74
$Ge_{0.97}Si_{0.03}$	1000	N	-1.81
$Ge_{0.97}Si_{0.03}$	2000	N	-1.97
$Ge_{0.97}Si_{0.03}$	3000	N	-2.27
$Ge_{0.97}Si_{0.03}$	4000	N	-2.91

The optical transmission spectra of the Ge modulators with the same waveguide width but the various waveguide lengths are analyzed. The contribution of the coupling loss is subtracted by comparing the same tapered waveguide modulators with different device lengths. The width of these waveguides is 400nm. The waveguide loss is extracted to be 225 dB/cm. The coupling loss is obtained to be 0.13 dB for the 400nm wide waveguide modulator. The free carrier induced absorption loss and the waveguide sidewall scattering loss are estimated by evaluating the optical mode distribution at the middle section of the waveguide modulator showing the mode intensity in top Si, middle Ge, and bottom Si sections. The top Si, middle Ge, and bottom Si sections have the optical intensity of 12%, 75%, and 10%, respectively, based on the mode distribution mapping on the cross section of the waveguide modulator structure. The waveguide material free-carrier induced absorption loss is calculated using the free carrier absorption model as Eq. 7.1. The free carrier absorption happens when the free carriers absorb the photon energy in the semiconductor materials.

$$\alpha = \frac{q^3 \lambda^2 p}{4\pi^2 \epsilon_0 c^3 n m^{*2} \mu} \qquad \text{Eq. 7.1}$$

where λ is the wavelength, p is the free carrier density for either electrons or holes, n is the refractive index, m^* is the effective mass, and μ is the carrier mobility. Si has electron mobility of 1400 $cm^2/s/V$ and hole mobility of 450 $cm^2/s/V$. Ge has electron mobility of 3900 $cm^2/s/V$ and hole mobility of 1900 $cm^2/s/V$. Effective mass of electron is 0.041 for Ge, and 0.2 for Si.

For the free carrier absorption in the bottom Si waveguide, which has a hole density of 10^{20} cm^{-3}, the absorption is 190 cm^{-1}. For the free carrier absorption in the Ge or GeSi waveguide, which has electron density of ~10^{18} cm^{-3}, the absorption is 5 cm^{-1}. The top Si contact has electron density

of 10^{20} cm^{-3}, in which the absorption is 60 cm^{-1}. The overall absorption is estimated to be 30 cm^{-1}. The waveguide loss due to the free carrier absorption is -130 dB/cm. Besides the free carrier induced loss, there is a loss at waveguide sidewalls. The loss at the waveguide sidewall could be due to the scattering loss because of the sidewall roughness and the abrupt change of the refractive index at the heterointerfaces. Assuming the waveguide loss has the two major causes of the free carrier absorption and the sidewall scattering loss. The sidewall loss is extracted by subtracting the free carrier absorption loss from the overall waveguide loss, to be -95 dB/cm for the narrow waveguides. As the waveguide width increases, the mode is more confined in the waveguides, and hence the sidewall roughness contribution on the waveguide loss decreases. However, the wide waveguides need to be optimized with the taper structure to reduce their coupling loss.

The waveguide integrated modulator coupling loss is also considered in the loss analysis. As simulated in the optical transmission and device taper designs in Chapter 3, the width of the waveguide is related to the optical coupling loss for the modulators. The simulated coupling loss as a function of the waveguide modulator width is plotted in Figure 7.7. The 400 nm wide waveguides show the lowest coupling loss. The waveguides with the widths above 700nm utilized the gradual two-step tapers, as suggested in the coupling design. The waveguide coupling loss from the measurements could be decoupled by subtracting the waveguide loss from the total device loss. The coupling loss via the tapers could be lowered to 0.14 dB.. The wider waveguide modulators show a higher coupling loss toward 1.79 dB. Compared to the simulated values of coupling loss varied from 0.32dB to 0.70 dB for waveguide modulators varied from 1um to 4um wide, the fabricated modulators show the excess loss increased from 0.3 dB to 0.8dB for the change of waveguide width from 1um to 4um. The design of the taper structure for wider modulators is discussed in Chapter 10 to improve device transmission and coupling.

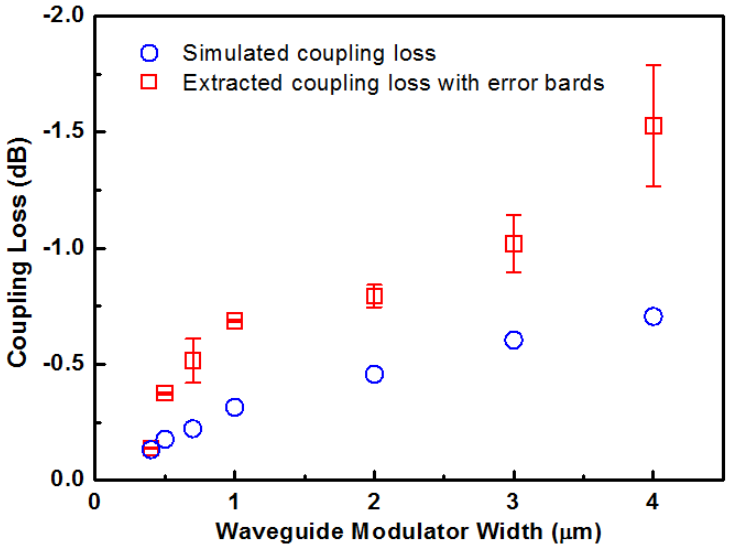

Figure 7.7 The comparison of the simulated coupling loss and extracted coupling loss as a function of the waveguide modulator width without the applied DC bias.

The overall transmission spectra of the $Ge_{0.99}Si_{0.01}$ modulators are much lower than those of the Ge and $Ge_{0.97}Si_{0.03}$ modulators. The difference among those modulators is due to the presence of the metal contacts on top of the $Ge_{0.99}Si_{0.01}$ waveguide modulators. The metal-induced absorption is extracted by subtracting the transmission spectra of the strained Ge modulators from the strained $Ge_{0.99}Si_{0.01}$ modulators. The metal-induced loss is obtained to be -4.38 ± 0.31 dB for the 50um long modulators based on the optical transmission measurements. Better light confinement in the Ge and GeSi waveguide is preferred in the design to minimize the mode interaction with any sections outside of the modulator waveguides, as proposed in Chapter 10.

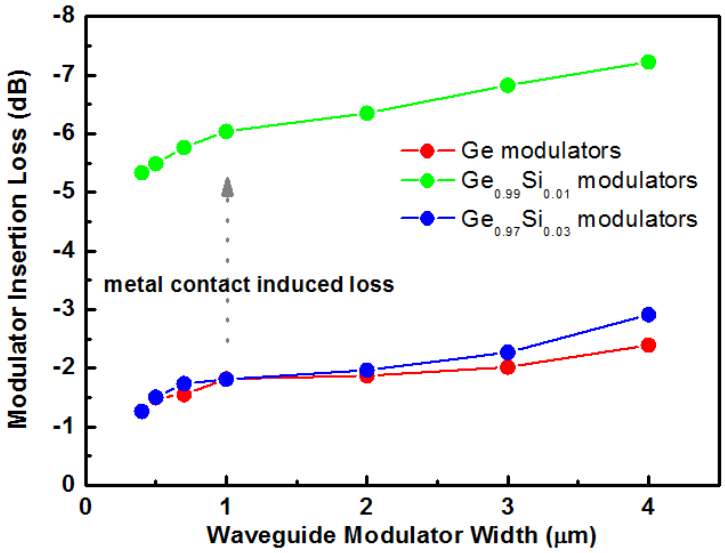

Figure 7.8 The insertion losses as a function of waveguide width for Ge, $Ge_{0.99}Si_{0.01}$, and $Ge_{0.97}Si_{0.03}$ modulators.

Chapter 8 Electrical contacts characterization

8.1 IV measurement on modulator arrays

IV measurements were conducted to characterize the electrical contacts of the modulators. An electrical probe station was set up in parallel with the optical alignment stage. Two electrical probes are connected to the source meter, and a Labview graphic user interface is used to control the voltage sweep range and step size of the IV measurements. The measurements were done on Ge and GeSi modulators with two GeSi compositions, several modulator dimensions, and different stressors. The IV curves of the modulators with various waveguide widths and lengths, as shown in Figure 8.2, are compared in ordor to investigate the dependence on the waveguide dimensions. The IV measurement probes the p-Si/i-Ge/n-Si diode behavior. Although the Ge or GeSi section is not intentionally doped, the phosphorous ion implantation on the top Si layer causes the minor n-type doping of $<10^{18}$ cm^{-3} in the Ge or GeSi region. The leakage current model is built to analyze the effects of materials quality and diode structures.

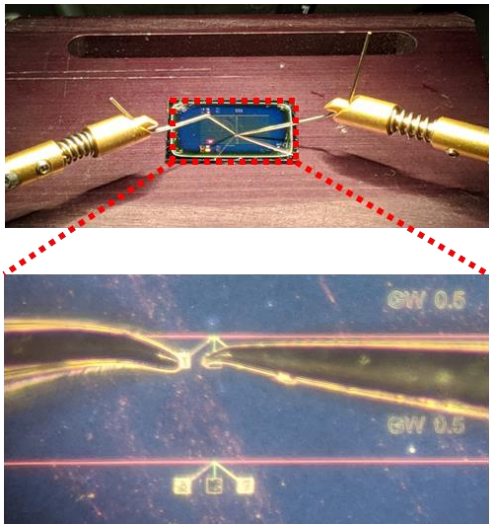

Figure 8.1. The electrical probe station for the modulators' electrical contacts characterization.

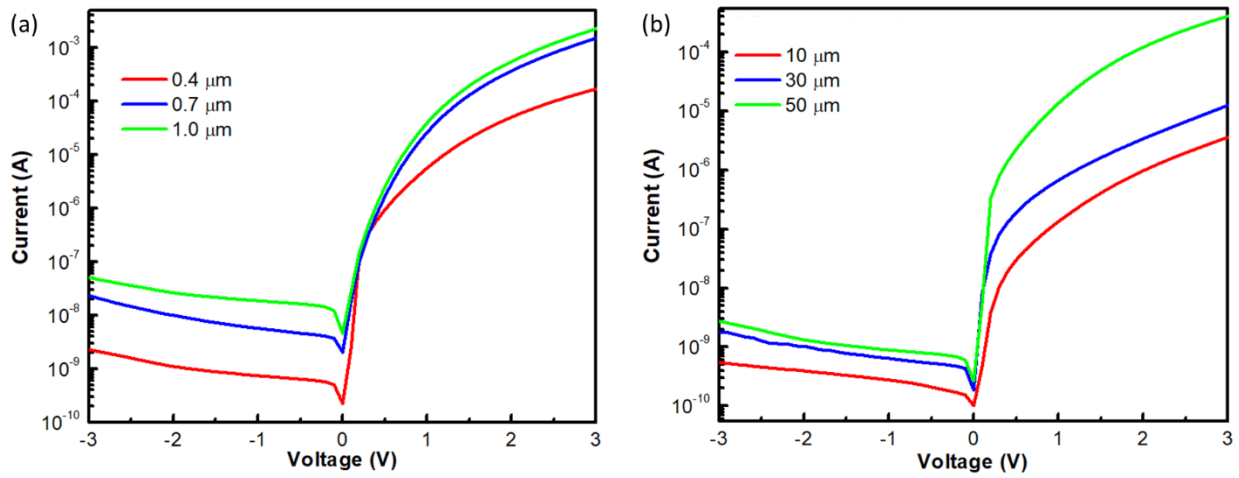

Figure 8.2. The IV measurements of the Ge waveguide modulators (a) as a function of the modulator width with a fixed modulator length of 50 um and (b) as a function of the modulator length with a fixed modulator width of 0.4um.

8.2 Leakage current model

The leakage current measured in Ge and GeSi modulators is further analyzed considering its dependence on the diode perimeter and area, which is expressed using the following equations:

$$I_D = J_P(V) * Perimeter + J_A(V) * Area \quad \text{Eq. 8.1}$$

$$J_D = J_P(V) * \frac{Perimeter}{Area} + J_A(V) \quad \text{Eq. 8.2}$$

where J_A is the area-dependent leakage current density per diode area, and J_P represents the perimeter-dependent leakage current density per diode perimeter. The two leakage current density terms are assumed independent of each other. The IV measurement results are replotted, as shown in Figure 8.3, with a fitting for the extraction of the area-dependent leakage current density and perimeter-dependent leakage current density values. The dark current in the modulator diodes has

a dominantly area-dependent behavior. The area-dependent leakage current density is 0.03 A/cm^2 at -1V, and is 0.06 A/cm^2 at -3V. The leakage current is higher at higher reverse voltage. The perimeter-dependent leakage current density is 1x10^{-7}A/cm for both -1V and -3V conditions. That indicates a good surface and sidewall passivation for the devices. One of the fabrication advantages in the process flow is the usage of H-SiO$_x$ (HSQ) ebeam photoresist. Instead of the commonly used polymer-based photoresist, which tends to form the polymer residual on the etched waveguide sidewalls, the HSQ forms a SiO_2 hard mask after lithography and development. That ensures smooth waveguide sidewalls and pristine interfaces between the waveguide sidewalls and stressor layers, which is key to achieving a low leakage current under reversed bias.

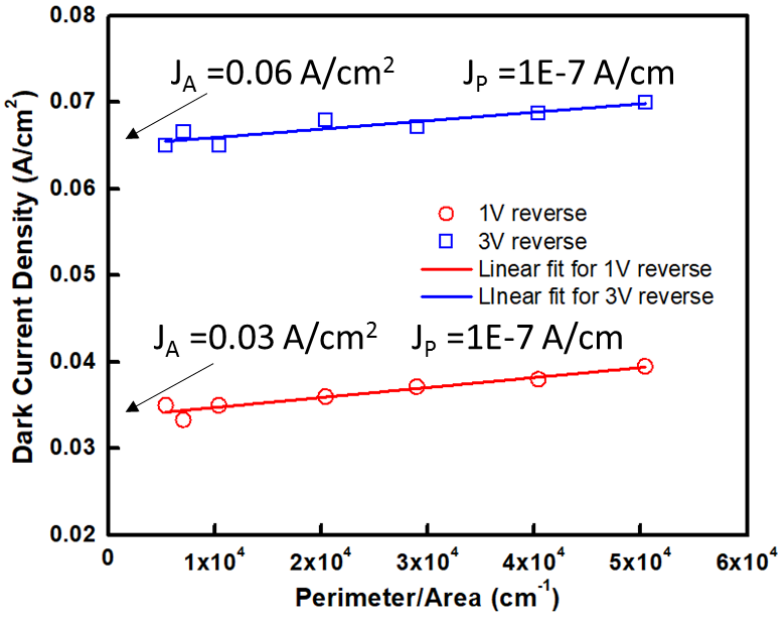

Figure 8.3. The current density plot as a function of perimeter over the area.

The p-Si/i-Ge/n-Si diode model is built using COMSOL Multiphysics. The model utilizes the actual geometry and dimensions of the waveguide modulator for the IV simulation. The model takes into account Maxwell's equations, Boltzmann transport theory, and Neumann boundary

conditions to obtain the stationary results at the heterojunctions in the diode. The basic equations in the model are the following:

$$-\nabla(\varepsilon\nabla\psi) = q(p - n + N) \quad \text{Eq.8.3}$$

$$-\nabla J_n = -qR_{SRH} \quad \text{Eq.8.4}$$

$$-\nabla J_p = qR_{SRH} \quad \text{Eq.8.5}$$

where ψ is the electrostatic potential, q is the elementary charge, n and p are the electron and hole concentrations, respectively, and N is the fixed charge associated with ionized donors.

The electron and hole current densities, J_n and J_p, can then be expressed in terms of ψ, n and p as shown in Eq. 8.6 and Eq. 8.7. μ_n and μ_p are the carrier mobilities, D_n and D_p are the carrier diffusivities. Shockley-Read-Hall recombination is represented by the term R_{SRH}, which is a general recombination process using traps in the bandgap of the semiconductor, where n_i is the intrinsic carrier concentration, τ_n and τ_p are the carrier lifetimes, and n_1 and p_1 are equal to n_i. The boundary conditions are included for the computation, where V_a is the applied voltage, which is going to be varied with a small voltage sweep step in the IV simulation.

$$J_n = -qn\mu_n\nabla\psi + qD_n\nabla_n \quad \text{Eq.8.6}$$

$$J_p = -qn\mu_p\nabla\psi - qD_p\nabla_p \quad \text{Eq.8.7}$$

$$R_{SRH} = \frac{np - n_i^2}{\tau_p(n + n_1) + \tau_n(p + p_1)} \quad \text{Eq.8.8}$$

$$\psi = V_a + \frac{kT}{q}\ln\left(\frac{\frac{N}{2} + \sqrt{(\frac{N}{2})^2 + n_i^2}}{n_i}\right) \quad \text{Eq.8.9}$$

$$n = \frac{N}{2} + \sqrt{(\frac{N}{2})^2 + n_i^2} \quad \text{Eq.8.10}$$

$$p = -\frac{N}{2} + \sqrt{(\frac{N}{2})^2 + n_i^2} \quad \text{Eq.8.11}$$

$$n_i^2 = np \quad \text{Eq.8.12}$$

At each value of V_a, the current density is calculated using the Lagrange multipliers in COMSOL. Two metal contacts are applied on the top and bottom of the p-Si/i-Ge/n-Si diode and defined as ideal ohmic contacts in the interface setting. The model is built on the 2D plane of X-Y coordinates and the Z plane (out-of-plane direction) to have a length of 50um. The real device dimensions are applied to have the layer thickness and width correspond well with the device structure. The applied voltage V_a is applied to the anode, and the cathode is grounded. A small initial value (typically zero) and a small sweep step ΔV (typically of order 10^{-2}V) are carefully set to avoid non-convergence of the model. The materials properties of Ge and Si are inputted from the COMSOL library and modified based on the actual properties of the Ge or GeSi materials and their doping profiles. The diode geometry meshes with the focus on finer meshing near the heterojunctions and the metal contacts.

The simulated IV results are plotted in Figure 8.4. For the case with a carrier lifetime of 0.01 μs, the leakage current at -1V is simulated to be 0.02 A/cm^2, which is consistent with the measured value of 0.03 A/cm^2. For the case with a carrier lifetime of 0.1 μs, the leakage current at

-1 V is 0.006 A/cm^2. That estimates the epiaxial Ge carrier lifetime to be ~ 0.01 us. The simulated dark current density is on the same order of magnitude as J_A values measured in the modulator diodes. The shape of the IV curves is different between the simulated and measured cases. Under reverse bias, the simulated curve is nearly flat, as is expected in an ideal diode case. The measured diode shows the leakage current increased with reverse bias. This leakage current increasing with reverse voltage might be due to trap-assisted tunneling. Compared to the other Ge carrier lifetime and dopant concentration values reported in the literature for Ge with various growth conditions, the quality of our epitaxial Ge on SOI substrate is comparable with Cz Ge wafers, as indicated in Figure 8.5. The carrier lifetime value derived from simulation and materials characterizations is consistent.

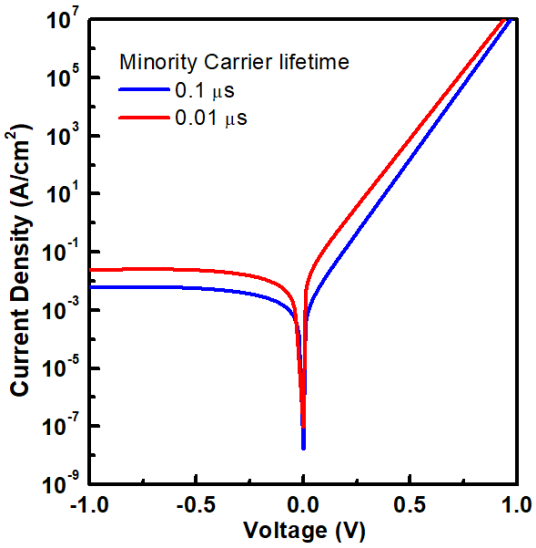

Figure 8.4. Simulated IV plot for p-Si/i-Ge/n-Si the diode with different minor carrier lifetime.

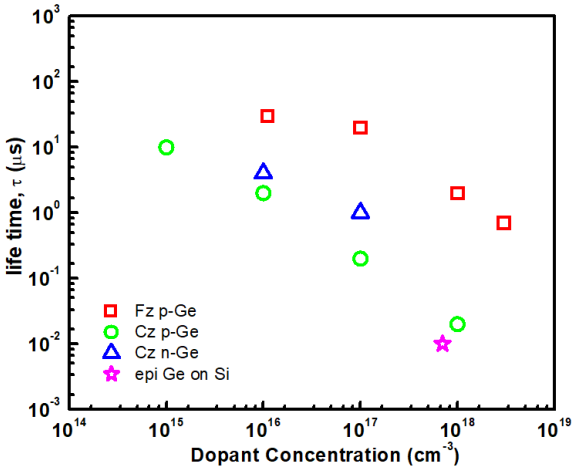

Figure 8.5. Comparision of the Ge lifetime and dopant concentration values for the Ge under various growth conditions.

Chapter 9 Optical transmission with DC Bias in strained GeSi modulator arrays

9.1 Experimental setup for optical transmission measurements with applied electric fields

The width of $Ge_{0.99}Si_{0.01}$ waveguide modulators is a unique design parameter to vary the modulator materials bandgap as a response to an identical stressor. The strain model developed in Chapter 4 shows uniform strain distributions in $Ge_{0.99}Si_{0.01}$ modulators with various waveguide widths and an identical 0.6GPa tensile stressor. The narrower waveguide modulator such as 400nm wide modulator has a larger induced tensile strain of ~0.5% compared to the wider modulator such as 4 μm wide modulator with an induced tensile strain of ~0.2%. As a demonstration of this concept, both the tensile and compressively strained $Ge_{0.99}Si_{0.01}$ modulator arrays have been fabricated and tested for optical transmission measurements with applied electric fields. The electrical probe station is connected with the optical edge coupling stage to apply a constant bias voltage at each optical transmission measurement. The bias voltage is varied from 0V to 6V. The extinction ratio is calculated based on the optical transmission data collected between different voltages. Individual modulator performance is evaluated through its extinction ratio spectrum and insertion loss spectrum, which demonstrates the modulation wavelength tuning via strain engineering. Strained modulator arrays are evaluated to a broad optical bandwidth coverage, which highlights the advantages of strained GeSi modulator array over other modulators.

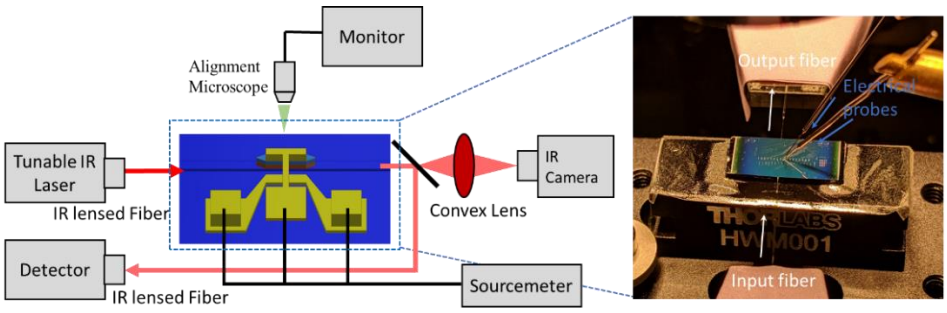

Figure 9.1. Schematic of the optical transmission measurement stage with the electrical probe station in parallel for the reverse bias application.

9.2 Optical transmission spectra of strained $Ge_{0.99}Si_{0.01}$ modulator arrays

The optical transmission spectra without external electric fields for the strained Ge and $Ge_{0.99}Si_{0.01}$ modulators have been analyzed to show absorption band edge tuning as a function of modulator strain. Through the fittings of the optical transmission curves, the absorption edge values are extracted and used to predict a ~100nm wide optical bandwidth of the strained Ge or $Ge_{0.99}Si_{0.01}$ modulator arrays. The strained $Ge_{0.99}Si_{0.01}$ modulators are evaluated by applying electrical fields and investigating the change in the optical transmission spectra as a function of bias voltage. As shown in Figure 9.2 (a) and (b), the modulators show the consistent change in the optical transmission curves in response to the applied voltage for both tensile and compressively strained $Ge_{0.99}Si_{0.01}$ modulators. As the reverse voltage increases, the optical absorption increases significantly near the modulator absorption edge. The compressive stressor shifts the optical absorption edge to the wavelength range lower than 1510nm.

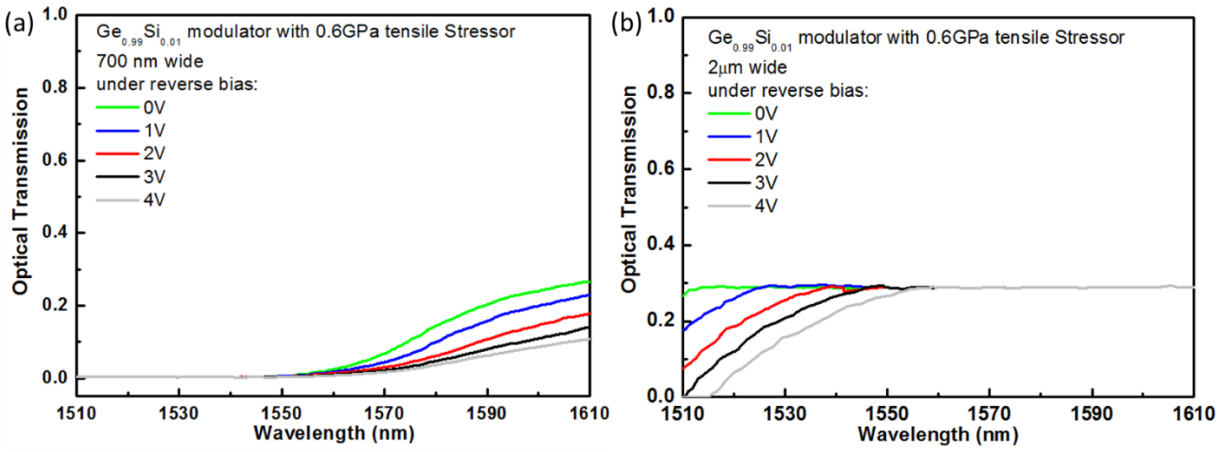

Figure 9.2. (a) the optical transmission spectra with a various applied voltage of (a) the 700nm wide $Ge_{0.99}Si_{0.01}$ waveguide modulator with 0.6GPa tensile stressor, and (c) the 2 um wide $Ge_{0.99}Si_{0.01}$ waveguide modulator with 1.0GPa compressive stressor

9.3 Extinction ratio evaluation of strained $Ge_{0.99}Si_{0.01}$ modulator arrays

Extinction ratio spectra are calculated based on the difference in the optical transmission at two different reverse bias voltages. For the tensile strained $Ge_{0.99}Si_{0.01}$ waveguide modulator array, the extinction ratio peaks are determined for all the modulators with waveguide widths from 400nm to 4μm in the optical testing window. The modulator absorption edge shifts from 1520nm to 1570nm when the modulator width is reduced from 4μm to 400nm. Although the extinction ratio peak position shifts in the same direction as the absorption edge, the peak positions are at slightly longer wavelength, as shown in Figure 9.4. The difference between the extracted bandgap and the ER peak is about 10.7 nm ± 0.7 nm. That is consistent with the electroabsorption modulation model, where an electric field induced absorption begins at a direct band edge and reaches its maxima at energy slightly lower than the band edge. Absorption edge shift as a function of waveguide width is due to a variation of induced waveguide strain with a fixed external stressor. This waveguide

strain variation with various waveguide width and a fixed stressor has been demonstrated in micro-Raman characterization in Figure 4.8 in Chapter 4. The extinction ratio values are modeled using the electroabsorption modulation model. The extinction ratio values are simulated between two electrical field strengths of 10 kV/cm and 40 kV/cm. The electrical field of 40 kV/cm is close to the actual electrical field applied at 3V reverse bias. The simulated extinction ratio peak value is 8.2dB ±0.1dB for the tensile strained $Ge_{0.99}Si_{0.01}$ modulators, while the measured extinction ratio peak is 4.7dB ±0.4dB. Since the compressive strain in the $Ge_{0.99}Si_{0.01}$ modulators enlarges the bandgap and shifts the modulation wavelength toward 1460nm, only the 4μm wide compressively strained $Ge_{0.99}Si_{0.01}$ modulator shows the extinction ratio peak in the optical testing window. The low extinction ratio values compared to the simulated results could be related to the metal-contact-induced absorption, as analyzed in the loss mechanisms in Chapter 7. That causes the modulator on-state (0V) to be less transmissive and reduces the contrast in the optical transmission spectrum when an electric field is applied. The extinction ratio performance of the strained $Ge_{0.99}Si_{0.01}$ modulator arrays could be improved with an improved top Si contact layer design and a more efficient coupling taper design to further lower the insertion loss. The lower loss would, therefore, enhance the transmission difference between the modulator on-state and off-state.

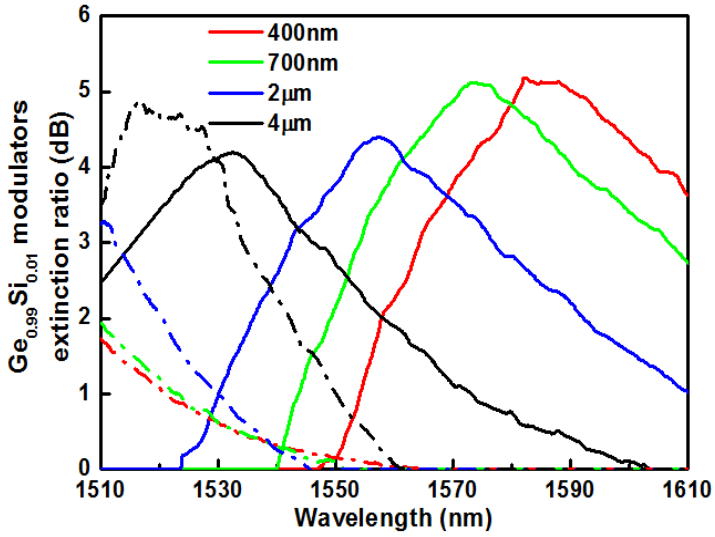

Figure 9.3. Extinction ratio evaluations between 0V and 3V states of tensile strained $Ge_{0.99}Si_{0.01}$ waveguide modulators (solid lines), and compressively strained $Ge_{0.99}Si_{0.01}$ waveguide modulators (dash-dot lines).

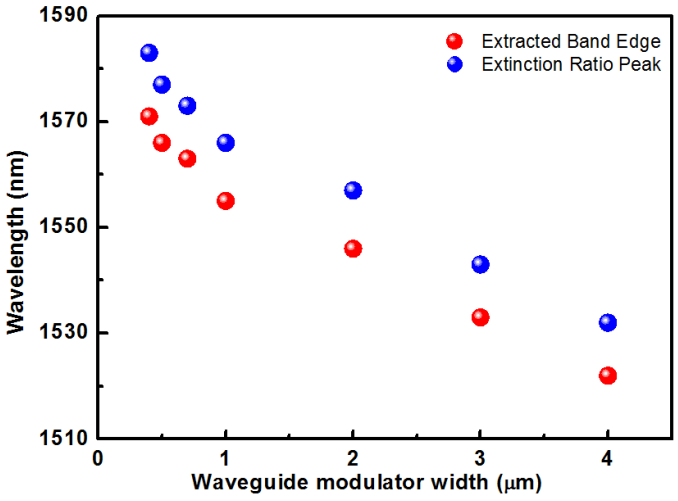

Figure 9.4. the extinction ratio peak positions as a function of the modulators width for the $Ge_{0.99}Si_{0.01}$ modulator array with the 0.6GPa tensile stressor.

Optical transmission measurements with higher reverse bias voltages from 4V to 6V have also been performed, as shown in Figure 9.5. The extinction ratio peaks shift toward higher

wavelengths with the reverse bias. That correlates with the tilting of the bandgap by an electric field. The higher the applied electric field, the more titled the bandgap; therefore, the larger the reduction in the tunneling energy for electron transition from valence band to conduction band. The redshift of the extinction ratios with the increase in the reverse bias illustrates such an effect in the reduction of the tunneling energy. The dynamic power follows the expression of $\frac{1}{2}(CV^2)$. The capacitance is considered as a total capacitance from a waveguide modulator and electrical contact pads. The relationship between the peak extinction ratio and the dynamic energy consumption are summarized in Figure 9.6. As the extinction ratio value is further increased with the applied voltage, the power consumption increases more dramatically as it is proportional to the square of the voltage.

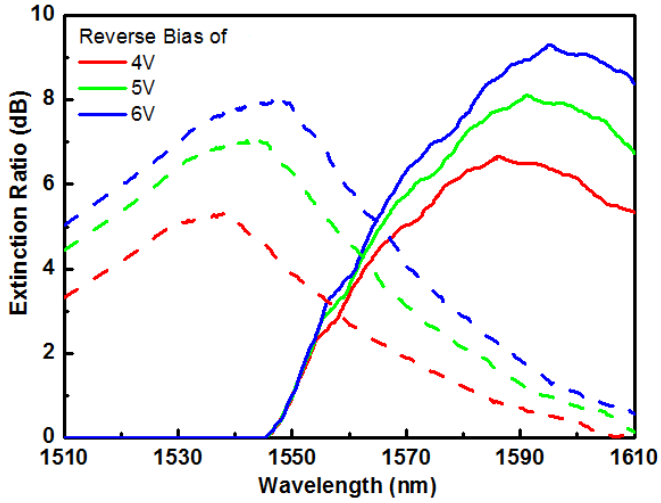

Figure 9.5. Measured extinction ratio as a function of the optical wavelength for the 400nm wide (solid lines) and 4um wide (dash lines) tensile strained $Ge_{0.99}Si_{0.01}$ modulators with the reverse bias from 4V to 6V.

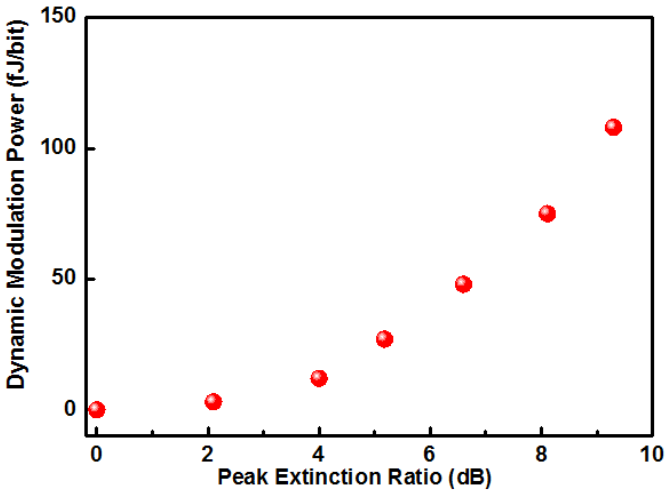

Figure 9.6. The correlation between the dynamic modulation power and the extinction ratio peak for the tensile strained 400nm wide $Ge_{0.99}Si_{0.01}$ waveguide modulator.

9.4 Demonstration of a broad optical-band modulation via strained $Ge_{0.99}Si_{0.01}$ modulator arrays

Both extinction ratio and insertion loss determine the operational wavelength range of a modulator. The metal-contact-induced absorption causes the $Ge_{0.99}Si_{0.01}$ modulators to have a larger insertion loss of ~5dB compared to the insertion loss of ~2dB in Ge and $Ge_{0.97}Si_{0.03}$ modulators, as shown in Chapter 7. Elimination of metal contact absorption can be achieved via increasing top Si electrode thickness, which will be addressed in Chapter 10. As for the current $Ge_{0.99}Si_{0.01}$ modulators, a high extinction ratio is required to obtain an ER/IL value > 1.3. Hence, the ER spectra at -6V are used to determine the modulators' operational wavelength ranges, as illustrated in Figure 9.7. As an example, an insertion loss of the 50 μm long and 700 nm wide tensile strained $Ge_{0.99}Si_{0.01}$ modulator is < 6.8 dB with an operating wavelength range from 1580 nm to 1610 nm, in which its extinction ratio is 1.3 times greater than the insertion loss at any given wavelength. Although strain and composition contributions tune the modulator absorption edge, the individual modulator operational range is generalized to be 27.5 nm ± 3.5 nm. A minimal operational wavelength occurs

at ~5 nm below the extinction ratio peak wavelength, and a maximal operational wavelength occurs at ~25 nm above the extinction ratio peak wavelength. When a wavelength is below an operational optical window, the direct bandgap absorption increases; hence, the insertion loss increase. When a wavelength is above an operational optical window, the field-induced Franz-Kelydsh effect reduces; hence, the extinction ratio reduces. A modulator operational window is set to be at the wavelength region with a high extinction ratio and low insertion loss. The improved insertion loss spectrum is also plotted in Figure 9.7, where the metal-induced-absorption is substracted from the original insertion loss spectrum. This allows the lower end of the operational wavelength range to be expended from 1580nm to to 1565nm. The wavelength coverage is enhanced from 30nm to 45nm. The reduction of insertion loss would also increase the extinction ratio. Therefore the actual improved wavelength coverage is > 45nm.

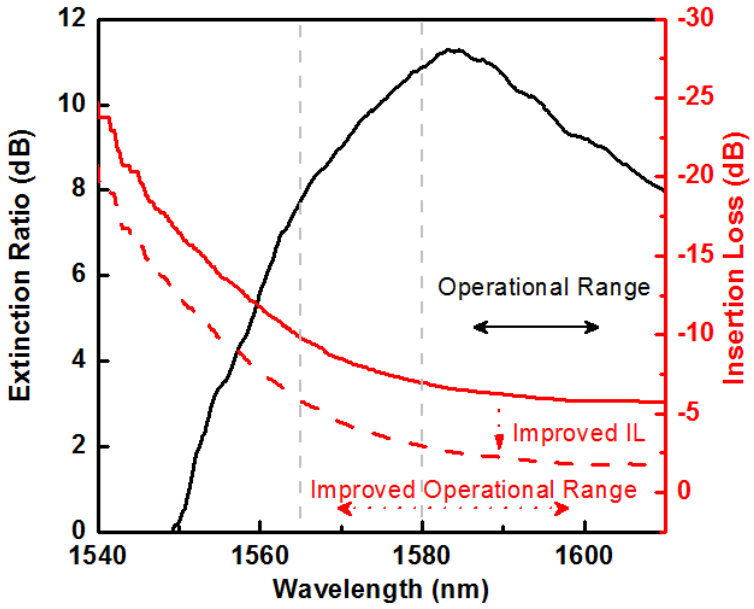

Figure 9.7. Extinction ratio (solid black) and insertion loss (solid red) spectrum for 700nm wide tensile strained $Ge_{0.99}Si_{0.01}$ modulator with a prediction of improved insertion loss (dash red) spectrum.

Broad optical bandwidth is successfully demonstrated for the tensile strained $Ge_{0.99}Si_{0.01}$ modulator array. The overall modulators operational window covers from 1525 nm to 1610 nm at -6V, as illustrated in Figure 9.8. A compressively strained $Ge_{0.99}Si_{0.01}$ modulator array is also demonstrated. The compressively strained $Ge_{0.99}Si_{0.01}$ electroabsorption modulators array covers the optical window from 1450 nm to 1540 nm at -6V. It is noteworthy that with the same modulator material composition of $Ge_{0.99}Si_{0.01}$, the modulators are able to operate from 1450nm to 1615nm wavelength via strain engineering. This is the largest GeSi modulator wavelength tuning via strain engineering reported up to date.

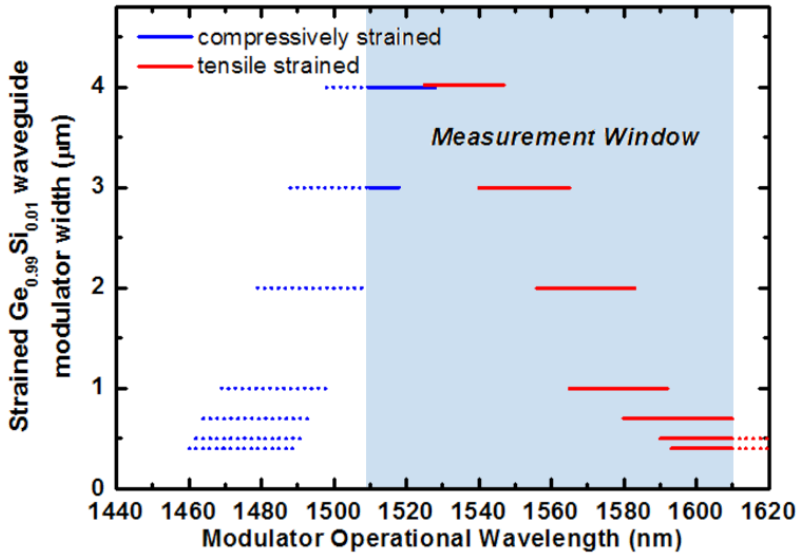

Figure 9.8. The modulator operational wavelength range as a function of the $Ge_{0.99}Si_{0.01}$ waveguide modulator at -6V width under the 0.6GPa tensile stressor (solid red) or 1.0GPa compressive stressor (solid blue) based on the ER measurements, and the simulated modulation ranges (dot lines) based on the optical transmission fitting for those beyond the measurement window.

The strained Ge and $Ge_{0.99}Si_{0.01}$ modulator arrays have been demonstrated with an optical bandwidth of ~100nm. Compared to unstrained modulators, a compressive stressor makes the

operational optical window to shift to a shorter wavelength range, and a tensile stressor makes the optical window shift to a longer wavelength range. A 1.0 GPa compressive stressor and a 0.6 GPa tensile stressor are used in this thesis work to demonstrate the strain effect on modulators. Those two stressors are selected based on the maximal achievable stress in both tensile and compressive cases available in the PECVD tool at the MIT cleanroom facility. Stressor layers applied to modulators are generally not limited to 1.0 GPa compressive and 0.6 GPa tensile stress. A stressor layer with more substantial intrinsic stress could further expand an optical bandwidth of a GeSi modulator array. With the silicon nitride stressors applied in the Ge modulator arrays, the compressively strained array covers an optical wavelength range from 1520nm to 1580nm, and the tensile strained array covers an optical wavelength range from 1580nm to 1680. As the Si composition increases from 0% to 1%, the unstrained $Ge_{0.99}Si_{0.01}$ is shifted to1550nm. Therefore, it has been demonstrated that the compressively strained array covers an optical wavelength range from 1450nm to 1510nm, and the tensile strained array covers an optical wavelength range from 1520nm to 1620nm, as shown in Figure 9.10. The Si composition can be further increased up to 4%, which shifts the unstrained $Ge_{0.96}Si_{0.04}$ modulators to1370nm, and the strained $Ge_{0.96}Si_{0.04}$ modulators can cover the optical wavelength from 1300nm to 1450nm. The GeSi bandgaps are estimated according to the linear interpolation of Ge and Si's L, Γ, and X bandgaps, as shown in Figure 9.9. For GeSi with Si compositions less than 10%, its bandgaps are more similar to that of Ge with increases in direct bandgap Eg^{Γ} and indirect bandgap Eg^{L}, and decrease in indirect bandgap Eg^{X} [75]. As the Si composition further increases, the indirect bandgap X valley crosses over with the direct bandgap Γ valley, and the possibility for indirect band transition increases and the direct bandgap Franz-Keldysh effect is reduced. As for the coverage of the entire telecommunication bands from the O band to the U band, the Si composition only needs to be

increased to 4%, where modulator insertion loss can still be kept low. This composition engineering makes it feasible and exciting to apply the strained GeSi modulator arrays to cover the entire telecommunication bands, as illustrated in Figure 9.10. Besides the strained modulator arrays, tensile strained GeSi could be used to fabricate waveguide integrated photodetectors. The same strain engineering has been demonstrated by my collaborator Dr. Yiding Lin, to show the tensile stressor application to enhance the detector performance at a higher wavelength range. The strained GeSi modulators and detectors can be fabricated in the same process flow with stressors to achieve an integration of the detector array and modulator array with a simplified design layout and fabrication procedure, which has not been proposed or demonstrated previously. This thesis work has served as a proof of concept to provide a promising and cost-effective platform using one-for-all strained modulator and detector arrays.

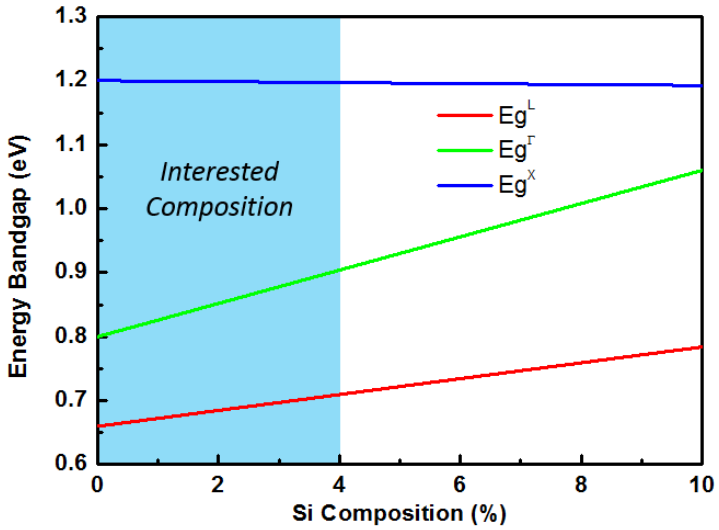

Figure 9.9. GeSi energy bandgaps as a function of Si composition.

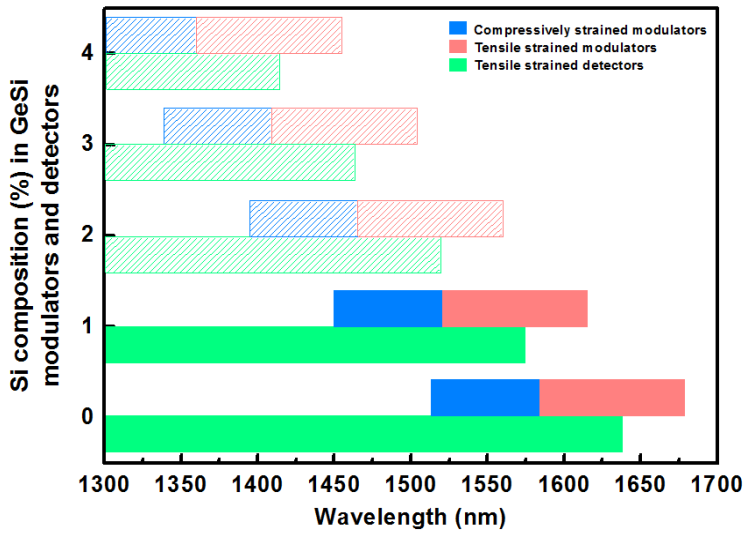

Figure 9.10. Optical wavelength coverage of strained modulator arrays and photodetectors as a function of GeSi composition. 1.0GPa compressive stressor and 0.6GPa tensile stressor are applied in the strained devices.

Chapter 10 Electrical bandwidth estimation and improvements for the strained GeSi modulator arrays

10.1 Electrical bandwidth estimation for current devices

The GeSi electroabsorption modulators have a small waveguide length of 50um due to its high extinction compared to Si MZI modulators. The GeSi modulator length is much shorter than the electrical signal wavelength during a high-speed RF modulation. Therefore, the modulator is considered as a lumped element in a driver electrical circuit. The optical signal propagates at speed much faster than the alternating speed of the electrical control signal for switching the modulator between on- and off-states. This lumped electrical property of the GeSi electroabsorption modulator simplifies the design for high-speed modulation. A Si MZI modulator, on the other hand, would require a traveling wave electrode design to compensate for its transient variation of the voltage along the modulator arms due to the long modulator length (millimeter), which is comparable to the electrical wavelength of a RF electrical signal above 50 GHz. For a strained GeSi modulator, on the other hand, its maximum operating frequency is limited by its resistance-capacitance (RC) constant. The internal resistance of a driver source is 50 Ω. The resistance of a GeSi modulator is negligible compared to the source resistance. The capacitance in the driver circuit is a sum of the modulator capacitance and electrical contact pad capacitance, as illustrated in Figure 10.1. The capacitance values of the strained $Ge_{0.99}Si_{0.01}$ modulators and electrical pads are listed in Table 10.1. The limiting factor in the current strained $Ge_{0.99}Si_{0.01}$ modulator design is its large capacitance from the electrical contact pads. The strained $Ge_{0.99}Si_{0.01}$ modulator has a bandwidth of 8.8 GHz for a 400nm wide modulator and 5.8 GHz for a 4um wide modulator based on their overall RC constants. The capacitance from the electrical contact pad contributes 96.7 %

of the total capacitance for the 400nm wide modulator and 64.2 % for the 4 um wide modulator. This large capacitance from the electrical contact pads is due to the small spacing between the top metal pad and the bottom contact layer, as illustrated in Figure 10.1. The bottom Si contact is doped at 10^{20} cm^{-3} for a fast electric field response. In the current device design, the bottom Si contact is only 500nm separated from its top metal pad with 50µm x 50µm dimensions, which causes a large capacitance in a driver circuit. The silicon nitride stressor layer lies between those two contacts has a higher dielectric constant than the traditional silicon oxide layer, which further increases the capacitance. Therefore, the strained GeSi modulator array is estimated to have an electrical bandwidth of ~6 GHz, limited by the smallest bandwidth from a 4um wide modulator.

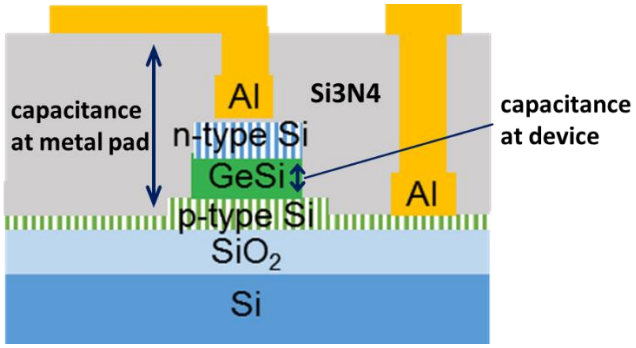

Figure 10.1. Schematic of the capacitance parameters in the strained GeSi modulator.

Table 10.1. The capacitances and estimated electrical bandwidth of the strained GeSi modulators.

Modulator Width (nm)	Active Device Area (um^2)	Capacitance at Device (pF)	Capacitance at Metal Pad (pF)	Total Capacitance (pF)	RC time constant (ps)	Bandwidth limit (GHz)
400	25	0.012	0.352	0.364	18.2	8.8
500	31	0.015	0.352	0.367	18.3	8.6
700	44.6	0.021	0.352	0.373	18.7	8.5
1000	88	0.042	0.352	0.394	19.7	8.1
2000	189	0.090	0.352	0.442	22.1	7.2
3000	310	0.148	0.352	0.500	25.0	6.7
4000	410	0.196	0.352	0.548	27.4	5.8

10.2 Design and process flow improvements for ultralow insertion loss and high-speed modulation

Although a broad optical bandwidth has been demonstrated in strained GeSi modulator arrays, the device performance can be improved by reducing insertion loss and redesigning electrical contacts to achieve an ultralow insertion loss toward ~1dB and high electrical bandwidth beyond 100 GHz.

The ultralow insertion loss design requires improvements in two different sections: (1) top metal contact-induced absorption, (2) free carrier absorption from GeSi modulator and doped Si contacts. The current top metal contact in a strained $Ge_{0.99}Si_{0.01}$ modulators contribute an extra loss of ~4dB, as analyzed in Chapter 7. That is due to the insufficient isolation of the optical mode from the top metal layer. The 3D FDTD transmission model is modified to understand the cause of this issue and to predict the Si top electrode thickness. The metal-induced absorption is extracted from the 3D FDTD model as a function of the top Si thickness. By increasing a top Si electrode thickness from 300 nm to 500 nm, the metal-induced absorption is significantly reduced from 4dB to nearly zero dB, as simulated. Besides the solution to the metal-contact-induced absorption, top and bottom Si electrode doping concentrations are considered to lower the free-carrier absorption. The current doping concentration of 10^{20} cm^{-3} is too high for both top and bottom Si electrodes. The current doping profile gives a response frequency of ~1THz at -3V. This fast transient response is far above the bandwidth limitation from its RC constant. That provides a design margin to reduce dopants concentrations in the Si electrodes, therefore, to reduce the free carrier absorption in the modulators. The transient electric field simulation is utilized to investigate a transient response in different doping combinations in the p-Si/Ge/n-Si diode structure. The dopant concentration is optimized in the Si to be ~ 10^{18} cm^{-3} of boron dopants and ~$10^{18}$$cm^{-3}$ of phosphorous dopants in bottom and top Si electrodes, respectively. That provides a transient response close to 300 GHz at

-3V and the electrical field intensity of 40kV/cm. The free carrier absorption in the GeSi modulator is then evaluated to achieve an absorption-induced modulator propagation loss of ~0.5dB per modulator. That would improve the total insertion loss from 6.15dB ±0.6dB to 1.15dB ±0.6dB in a strained $Ge_{0.99}Si_{0.01}$ modulator.

The capacitance from the metal contact pads can be reduced via two approaches, as illustrated in Figure 10.2,: (1) an oxide layer can be deposited on top of stressor layer to increase the separation between top metal pad and bottom Si layer; (2) the p-Si region below the top metal pad can be etched by adding one more lithography and patterning step before the stressor layer deposition so that the top metal pad will not form a capacitance with the bottom Si layer. In the first approach, a top oxide layer can be placed via PECVD right after silicon nitride stressor layer deposition. The dual frequencies in the PECVD oxide deposition need to be controlled to ensure no or minimal stress in the top oxide layer. Otherwise, the strain model needs to be modified to take into account of intrinsic stress from top oxide. The electrical bandwidth is estimated as a function of the top oxide thickness, as shown in Figure 10.3. The 2um top oxide cladding layer would reduce the metal-pad-induced capacitance, and enhance the electrical bandwidth toward 60 GHz for a 400nm wide $Ge_{0.99}Si_{0.01}$ modulator. However, this approach is not sufficient to further improve the electrical bandwidth toward 100 GHz. The second approach, as illustrated in Figure 10.2, is a promising solution to this challenge. Instead of placing micrometers thick oxide on top of a device layer and increasing the difficulty of integrating with CMOS circuit layers, the p-type conductive Si region can be patterned and etched before the top metal formation. That dramatically reduces the overall capacitance and increases the electrical bandwidth to 250 GHz for a 400nm wide $Ge_{0.99}Si_{0.01}$ modulator. That approach is also more feasible in the foundry processing without

adding extra layers for thicker oxides. Alternatively the boron implantation can be directly masked with implantation regions only linked between bottom electrodes and bottom metal contacts.

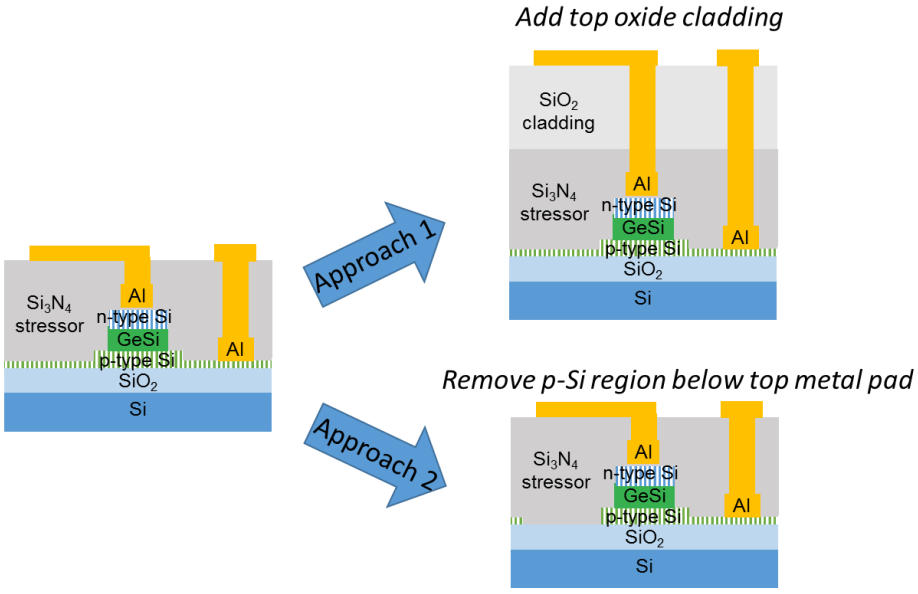

Figure 10.2. Illustration of two different approaches to enhance the electrical bandwidth of the strained modulators.

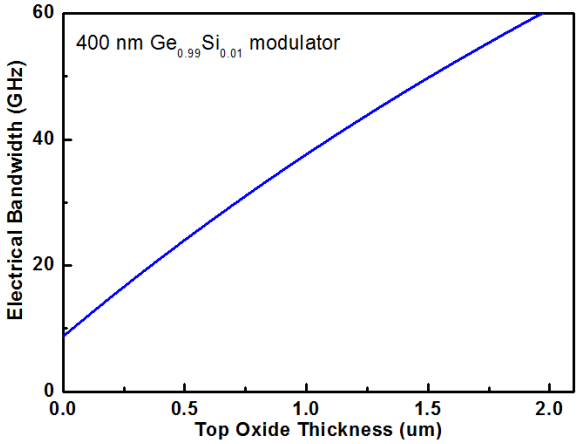

Figure 10.3. The 400 nm wide $Ge_{0.99}Si_{0.01}$ modulator's electrical bandwidth as a function of the top oxide thickness.

After making the design improvements in insertion loss reduction and electrical bandwidth enhancement, the strained GeSi modulator array will double its current ER/IL value from ~2 to 5, ultrabroad optical bandwidth of 100 nm, and high electrical bandwidth above 100GHz. In the device process flow development, two main modifications are made: (1) optimizing the ion implantation conditions for both dopants, (2) adding one more set of alignment, lithography, and etching before the metal layer formation. The TCAD simulation is performed for optimized boron and phosphorous dopants concentrations in bottom and top Si electrodes, respectively. For boron ion implantation, conditions are modified to be with an implantation energy of 60 keV, a dosage of $2.5\text{x}10^{13}/\text{cm}^2$, and annealing temperature at 1000 ºC for 30 minutes to achieve active boron concentration of 10^{18} cm^{-3} in the bottom Si electrode. For phosphorous ion implantation, the conditions are modified to be with an implantation energy of 190 keV, a dosage of $8.0\text{x}10^{13}/\text{cm}^2$, and annealing temperature at 650 ºC for 30 minutes to achieve the active phosphorous concentration of 10^{18} cm^{-3} in the top Si electrode. The improved process flow is CMOS-compatible and readily adaptive to foundry processing.

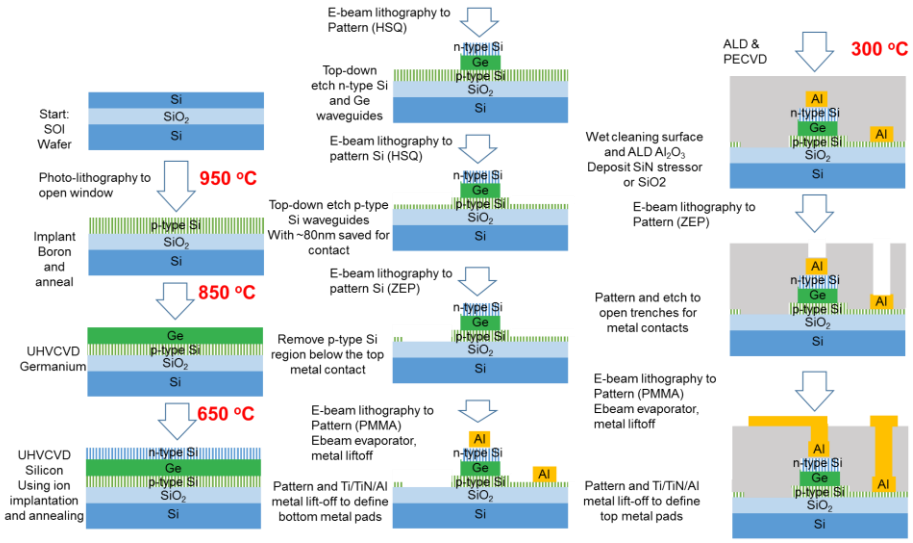

Figure 10.4. Modified process flow for strained GeSi modulator array.

Chapter 11 Summary and Outlook

11.1 Conclusions and Impact

Electronic and photonic integrated circuits serve as a promising platform for telecommunications and sensing applications. Electroabsorption modulators allow fast modulation, small device footprint, and low power consumption. Epitaxially grown GeSi films on SOI substrates are a suitable materials platform for integrated modulator applications due to the Si CMOS compatibility and distinctive optoelectronic materials properties. A modulator's operation wavelength adjustment and its system integration for broadband modulation are two major challenges of fabricating on-chip modulator arrays for telecommunication. Unlike Si MZI modulators, GeSi electroabsorption modulators are not broadband due to its limited working region near absorption edge for Franz-Keldysh effect. Optimization of a modulator material for a target wavelength can be achieved by tuning material composition or applying strain to the material. In order to realize an integrated system with a broadband modulation, multiple electroabsorption modulators have to be fabricated individually and assembled onto a chip in a conventional approach. Each fabrication step adds cost to design and processing. Integrating more modulators for multiple operating wavelengths allows a broader optical band coverage and higher optoelectronic data processing capacity, which is desirable for lower cost, simpler layout, and easier electronic and photonic circuits integration.

In this thesis work, a one-for-all strained GeSi modulator array design is proposed and demonstrated to cover a broad telecommunication band with multiple modulators designed and fabricated simultaneously in the same process flow. A stressor layer applies a homogeneous strain to a waveguide modulator. By changing a modulator width, strain in the modulator changes, tuning

the material bandgap and, therefore, the modulator operational wavelength. Modulators made of the same material can operate at various wavelengths with the same stressor layer by simply designing a modulator array with various waveguide widths.

The matrix of investigation consists of two compositions (Ge and $Ge_{0.99}Si_{0.01}$) and three types of strain (compressive, tensile, and no strains). A desirable modulator performance is the balance of low insertion loss, high extinction ratio, high speed, broad optical bandwidth, and low modulation power consumption, as summarized in Figure 11.1. In terms of extinction ratio over insertion loss (ER/IL) values, the Si RR modulator has the highest ER/IL. The strained GeSi EAM has a ER/IL value of 1.7, similar as that of IIIV EAM. individual GeSi EAMs presented in this thesi, with waveguide width less than 2 μm, have an improved ER/IL performance from 1 to 1.7 due to a reduction of insertion loss with a tapered modulator coupling design. The GeSiEAM has an average optical bandwidth of 30nm, which is in the 15nm to 40nm ranged reported in the literature for Ge and GeSi EAM's. However, the strained GeSi EAM's can operate in arrays, in which an identical stressor layer is applied on all modulators in an array, and the one-for-all strained array demonstrates the highest optical bandwidth of ~100nm among all the electroabsorption modulators. Minor design improvements can be made on the current devices. Increasing the top Si electrode thickness to 500nm will improve the modulator insertion loss to 2dB, as experimentally indicated in strained Ge and $Ge_{0.97}Si_{0.03}$ modulators. As highlighted in Figure 11.1, this reduction in insertion loss will further improve the device ER/IL value to 3, which is higher than the ER/IL values of GeSi EAM, IIIV EAM, and Si MZI.. Patterned boron ion implantation for p-Si electrodes will eliminate capacitance from the metal contact pads, and obtain high-speed modulation well above 100 GHz. The dynamic power value of a strained GeSi modulator needs to be related to a specifically measured modulation frequency. Based on the

modulation energy equation of $(1/2)CV^2$, the current device has an energy consumption of ~30 fJ/bit at a modulation frequency of 10 GHz due to its large capacitance contribution from the metal contact pad. Overall, the strained GeSi EAM arrays with minor improvements show excellent ER/IL performance, high optical bandwidth, and a moderate modulation energy consumption.

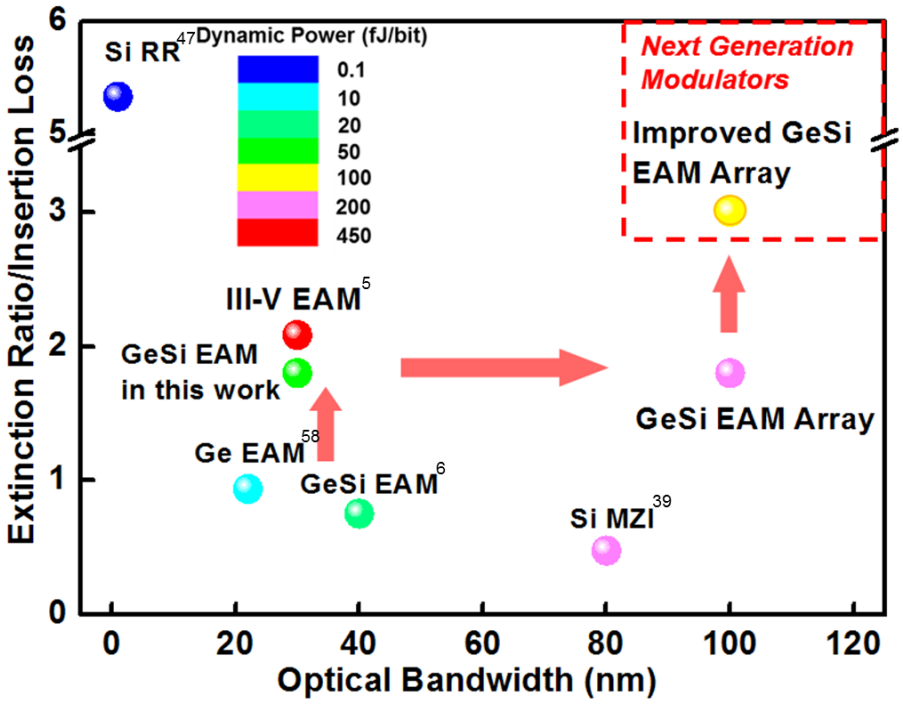

Figure 11.1. Modulator performance comparison of GeSi EAM array with other modulators.

Although the broad optical bandwidth has only been demonstrated in the optical testing window from 1510nm to 1610nm, this one-for-all strained GeSi modulator array approach is not limited to the C- and L- bands. An increase in Si composition to 4% allows a strained $Ge_{0.96}Si_{0.04}$ modulator array to cover the optical wavelength from 1300nm to 1450nm. Besides strained GeSi modulators, the same strain engineering approach has been demonstrated by my collaborator Dr. Yiding Lin on strained Ge photodetectors. The tensile strained Ge photodetectors have shown enhancement on photon detection at a higher wavelength range of beyond 1600nm. Therefore, this

one-for-all strain engineering approach will allow GeSi modulator and detector arrays to be integrated into the same process flow for an on-chip broadband multi-channel optical transceiver with a simplified design layout and low-cost fabrication, as illustrated in Figure 11.2. That presents a promising platform for integrated photonic devices with an ultrawide optical coverage over an entire telecommunication bandwidth.

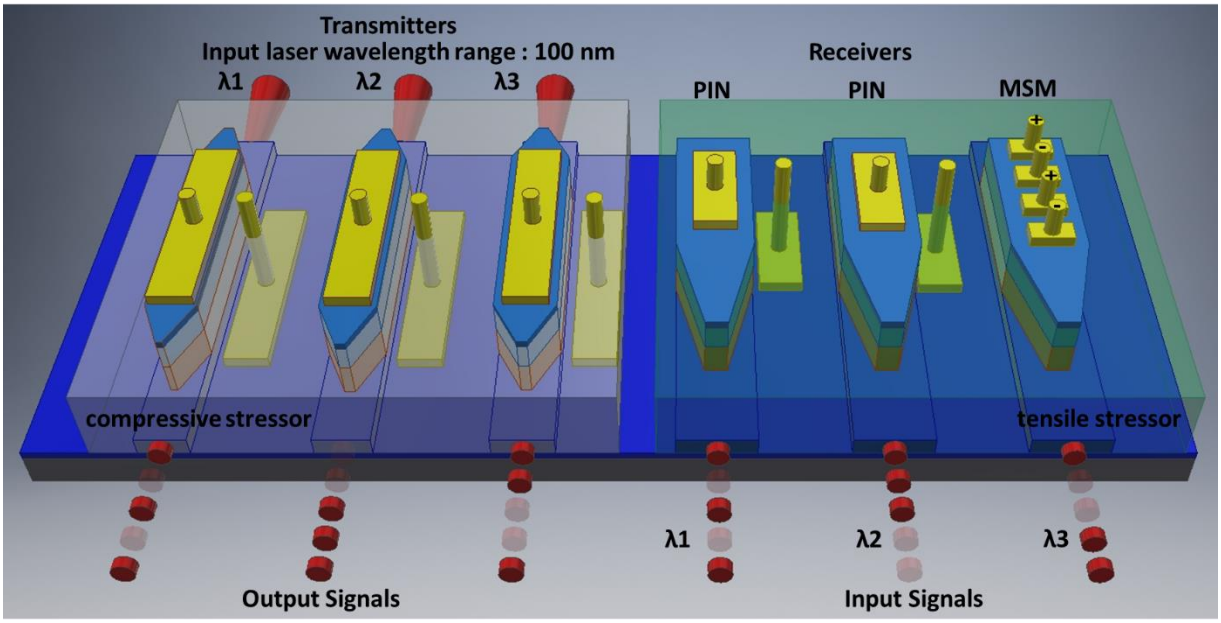

Figure 11.2 Schematic of strained GeSi modulator and photodetector arrays for an on-chip broadband optical transceiver.

11.2 Future Work

The demonstration of strained Ge and $Ge_{0.99}Si_{0.01}$ modulator arrays points out the possibility for strained $Ge_{0.98}Si_{0.02,}$ $Ge_{0.97}Si_{0.03,}$ $Ge_{0.96}Si_{0.04}$ modulator arrays to achieve a modulation coverage over the entire telecommunication bands. Future work needs to be done in terms of optical coupling design, optical transmission optimization, and electrical contact optimization for realizing modulations over specific telecommunication bands. Successful integration of modulator and photodetector arrays requires further work on combined process flow for strained arrays.

The one-for-all strain engineering innovation can also be applied to waveguide integrated light-emitting arrays, such as III-V and Ge lasers. The fundamental approach is the same for strain engineering of III-V materials, where the bandgap can be tuned by an external stressor applied to a waveguide structure. As a preliminary study for a strained III-V waveguide array, $(Al_{0.3}Ga_{0.7})_{0.5}In_{0.5}P$ multiple-quantum well layers have been made into waveguides with widths varies from 0.1 μm to 10 μm. The $(Al_{0.3}Ga_{0.7})_{0.5}In_{0.5}P$ multiple-quantum well layers were deposited by Dr. Bing Wang in the Low Energy Electronic Systems (LEES) center of the Singapore-MIT Alliance for Research and Technology (SMART). A 1.0 GPa compressive stressor is applied to the waveguide array following a similar procedure for a strained GeSi modulator array fabrication without Si electrode and metal contact formation. A Horiba Micro-Raman Spectrometer is used to evaluate photoluminescence (PL) performance of those strained III-V waveguides, as plotted in Figure 11.3 (a). A constant PL peak shift is observed as a function of waveguide width. Similar to the strain effect on GeSi waveguide modulators, a wider waveguide experiences less strain effect compared to a narrower waveguide structure. Therefore, a 0.1 μm wide IIIV waveguide shows the most shift from the un-strained PL wavelength of 693nm to 686nm. Deformation potential theory

has been applied to evaluate a compressive strain effect on the IIIV waveguide array with a modified strain model for the $(Al_{0.3}Ga_{0.7})_{0.5}In_{0.5}P$ quantum well structures. The experimental results in PL spectra agree with the strain model, as shown in Figure 11.3 (b). Therefore, this preliminary study supports the statement for a potential application of this one-for-all strain engineering in a light emitter array. Future work is then required to demonstrate a strained light-emitter array operating in the wavelength range from 1300nm to 1600nm. That eventually allows full on-chip integration of light sources, modulators, and photodetectors with a strained array configuration, simplified layouts, and low integration and fabrication cost.

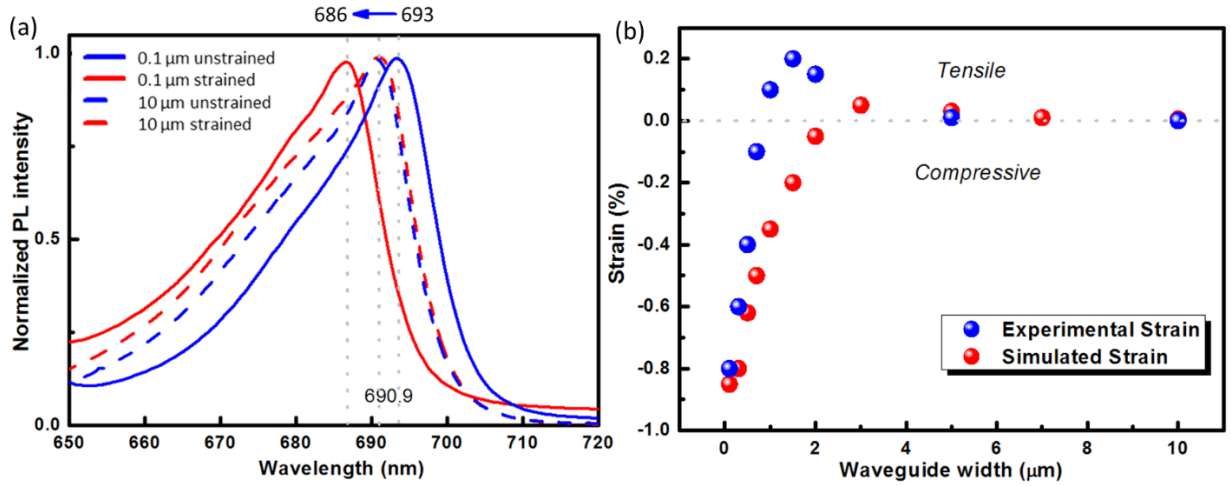

Figure 11.3. (a) photoluminescence spectrum of 0.1 μm and 10 μm wide III-V waveguides with and without a 1.0 GPa compressive stressor. (b) Comparison of strain effect in the III-V waveguide arrays between experimental and simulation results as a function of waveguide width.

References

[1] R. G. Hunsperger, "Integrated Optics Theory and Technology," Springer, New York, 2002.

[2] R.A. Soref and B.R. Bennett, "Electrooptical Effects in Silicon," *IEEE Journal of Quantum Electronics,* QE-23, 123-129, 1987.

[3] J. Liu, et al., "Waveguide-integrated, ultralow-energy GeSi electro-absorption modulators," *Nat. Photonics*, **2**, 433-437, 2008.

[4] J. Michel, J. Liu, L. C. Kimerling, "High-performance Ge-on-Si photodetectors," *Nat. Photonics*, **4**, 527–534, 2010

[5] Y. Tang, et al., "Over 67 GHz bandwidth hybrid silicon electroabsorption modulator with asymmetric segmented electrode for 1.3 μm transmission," *Opt. Exp.*, **20**, 11529–11535, 2012.

[6] L. Mastronardi, et al., "High-speed Si/GeSi hetero-structure Electroabsorption Modulator," *Opt. Exp.,* **26**, 6663-6673, 2018.

[7] G. Masini, L. Colace, G. Assanto, H.-C. Luan, and L. C. Kimerling, "High performance *p-i-n* Ge on Si photodetectors for the near infrared: from model to demonstration," *IEEE Transactions on Electron Devices,* 48(6), 2001.

[8] Z. Huang, J. Oh, J. Campbell, "Back-side-illuminated high-speed Ge photodetector fabricated on Si substrate using thin SiGe buffer layers," *Appl. Phys. Lett.,* **85**, 3286-3289, 2004.

[9] D. Feng, et. al., "High-speed Ge photodetector monolithically integrated with large cross-section silicon-on-insulator waveguide, " *Appl. Phys. Lett*., **95**, 261105, 2009.

[10] D. Suh, S. Kim, J. Joo, G. Kim, "36-GHz high-responsivity Ge photodetectors grown by RPCVD," *IEEE Photon. Technol. Lett.,* **21**, 672-674, 2009.

[11] A. Ghrib, et al., "All-around SiN stressor for high and homogeneous tensile strain in germanium microdisk cavities," *Adv. Opt. Mater.,* **3**, 353–358, 2015.

[12] S. Wirths, et al., “Lasing in direct-bandgap GeSn alloy grown on Si,” *Nat. Photonics,* **9**, 88, 2015.

[13] W. Hu, et al., “Germanium/perovskite heterostructure for high-performance and broadband photodetector from visible to infrared telecommunication band.” *Light Sci. Appl.,* **8,** 106, 2019.

[14] F. T. Pilon, et al., “Lasing in strained germanium microbridges,” *Nat Commun,* **10,** 2724, 2019.

[15] E. D. Palik, “Handbook of Optical Constants of Solids,” Academic Press, NY, 1985.

[16] R. People, "Physics and applications of GexSi1-x/Si strained-layer heterostructures," *IEEE Journal of Quantum Electronics,* **22**, 1696-1710, 1986.

[17] E. A. Fitzgerald, et. al. “Relaxed Ge_xSi_{1-x} structures for III–V integration with Si and high mobility two-dimensional electron gases in Si,” *Journal of Vacuum Science & Technology B: Microelectronics and Nanometer Structures Processing, Measurement, and Phenomena,* 10, 1807, 1992

[18] E. A. Fitzgerald, “GeSi/Si Nanostructures,” *Science,* **25**, 417-454, 1995

[19] S. B. Samavedam, E. A. Fitzgerald, “Novel dislocation structure and surface morphology effects in relaxed Ge/Si-Ge(graded)/Si structures,” *Journal of Applied Physics,* **81**, 3108, 1997.

[20] M. T.Currie, et al., “Controlling threading dislocation densities in Ge on Si using graded SiGe layers and chemical-mechanical polishing,” *Appl. Phys. Lett.,* **72**, 1718, 1998.

[21] H.-C. Luan et. al.,“ High-quality Ge epilayers on Si with low threading-dislocation densities,” *Appl. Phys. Lett.*, **75,** 2909, 1999.

[22] J. Liu, et al., “Ge-on-Si optoelectronics,” *Thin Solid Films*, **520**, 3354-3360, 2012

[23] C. Sun, et al., “Single-chip microprocessor that communicates directly using light,” *Nature*, **528**, 534-538, 2015.

[24] M. Shulaker, et al., “Three-dimensional integration of nanotechnologies for computing and data storage on a single chip,” *Nature,* **547,** 74–78, 2017.

[25] G. S. Jeong, W. Bae, D. K. Jeong, “Review of CMOS Integrated Circuit Technologies for High-Speed Photo-Detection,” *Sensors (Basel)*, **17**, 1962, 2017

[26] A. H. Atabaki, et al., "Integrating photonics with silicon nanoelectronics for the next generation of systems on a chip," *Nature,* **556**, 349-354, 2018.

[27] M. Rakowski, et al., "Hybrid 14nm FinFET-Silicon Photonics Technology for Low-Power Tb/s/mm 2 Optical I/O," *2018 IEEE Symposium on VLSI Technology*, 221-222, 2018.

[28] R. Mayank, et al., "A 50Gb/s Hybrid Integrated Si-Photonic Optical Link in 16nm FinFET," *2019 Symposium on VLSI Circuits*, IEEE, 2019.

[29] M. Rakowski, et al., “45nm CMOS Silicon Photonics Monolithic Technology for next-genreation, lower power and high speed optical interconnects,” *2020 Optical Fiber Communications Conference and Exhibition (OFC)*, T3H.3, 2020.

[30] L. Vivien, “Computer technology: Silicon chips lighten up,” *Nature*, **528**, 483-484, 2015.

[31] P. Chaisakul, et al., “Recent Progress on Ge/SiGe Quantum Well Optical Modulators, Detectors, and Emitters for Optical Interconnects,” *Photonics, 6,* 24, 2016.

[32] S. Gupta, et al., "50GHz Ge waveguide electro-absorption modulator integrated in a 220nm SOI photonics platform," *2015 Optical Fiber Communications Conference and Exhibition (OFC)*, Tu2A.4, 2015.

[33] G. Kim, et al., “Single-chip photonic transceiver based on bulk-silicon, as a chip-level photonic I/O platform for optical interconnects,” *Sci. Rep.*, **5,** 11329, 2015.

[34] G. T. Reed, and C. E. Jason Png, "Silicon optical modulators," *Materials Today,* **40**, 40-50, 2015.

[35] Q. Xu, B. Schmidt, S. Pradhan, and M. Lipson, "Micrometer-scale silicon electro-optic modulator," *Nature,* **435**, 325-327, 2005.

[36] A. Liu, et al., "A High-speed Silicon Optical Modulator based on a metal-oxide semiconductor capacitor," *Nature,* **427**, 615-618, 2004.

[37] L. Liao, et al., "High speed silicon Mach-Zehnder modulator," *Optics Express,* **13** (8), 3129-3135, 2005.

[38] X. Xiao, et al., "High-speed, low-loss silicon Mach–Zehnder modulators with doping optimization," *Opt. Express,* **21**, 4116-4125, 2013.

[39] M. Streshinsky, et al., "Low power 50Gb/s silicon traveling wave Mach-Zehndermodulator near 1300 nm," *Opt. Exp.,* **21**, 30350–30357, 2013.

[40] J. Witzens, "High-Speed Silicon Photonics Modulators," *Proceedings of the IEEE*, **106**, 2158-2182, 2018.

[41] J. Sourabh, R. Swati, V. Kaushik, M. Kumar, "High speed optical modulator based on silicon slotted-rib waveguide," *Optics Communications*, **434**, 49-53, 2019.

[42] W. D. Sacher, J. K. S. Poon, "Dynamics of microring resonator modulators," *Opt. Express*, **20**, 15741–15753, 2008.

[43] Y. Amemiya, et al., "Optical modulator using metal-oxide-semiconductor type Si ring resonator," *Opt. Rev.* **16**, 247–251, 2009.

[44] R. M. Briggs, I. M. Pryce, and H. A. Atwater, "Compact silicon photonic waveguide modulator based on the vanadium dioxide metal-insulator phase transition," *Opt. Express,* **18**, 11192-11201, 2010.

[45] L. Zhang, et al., "Silicon-based Microring Resonator Modulators for Intensity Modulation," *J. Select. Topics Quantum Electron.,* **16**, 149–158, 2010.

[46] X. Xiao, et al., "25 Gbit/s silicon microring modulator based on misalignment-tolerant interleaved PN junctions," *Opt. Express,* **20**, 2507-2515, 2012.

[47] E. Timurdogan, et al., "An ultralow power athermal silicon modulator," *Nature Commun.*, **5**, 4008, 2014.

[48] J. Müller, et. al., “Optical Peaking Enhancement in High-Speed Ring Modulators,” *Sci. Rep.*, **4,** 6310, 2015.

[49] X. Zheng, et al., "A high-speed, tunable silicon photonic ring modulator integrated with ultra-efficient active wavelength control," *Opt. Express*, **22**, 12628-12633, 2014.

[50] J. Hyoung Lee, et al., “High power and widely tunable Si hybrid external-cavity laser for power efficient Si photonics WDM links," *Opt. Express*, **22**, 7678-7685, 2014.

[51] V. Jeyaselvan, et al., "Thermally-induced optical modulation in a vanadium dioxide-on-silicon waveguide," *OSA Continuum*, **3**, 132-142, 2020.

[52] S. L. Chuang, “*Physics of Optoelectronic Devices,”* John Wiley & Sons, Inc., New

York, 1995.

[53] Y.-H. Kuo, et al., “Strong quantum-confined stark effect in germanium quantum-well structures on silicon,” *Nature, 437,* 1334-1336, 2005.

[54] Y. Kim, et al., "Ge-rich SiGe-on-insulator for waveguide optical modulator application fabricated by Ge condensation and SiGe regrowth," *Opt. Express,* 21, 19615-19623, 2013.

[55] D. C. S. Dumas, et al., "Ge/SiGe quantum-confined Stark effect electro-absorption modulation with low voltage swing at $\lambda = 1550$ nm," *Opt. Express,* **22**, 19284-19292, 2014.

[56] S. Gupta, et al., "50GHz Ge Waveguide Electro-Absorption Modulator Integrated in a 220nm SOI Photonics Platform," *Optical Fiber Communication Conference*, Tu2A.4, 2015.

[57] J. Gao, et al., "Design and analysis of electro-absorption modulators with uniaxially stressed Ge/SiGe multiple quantum wells," *Opt. Express,* **25**, 10874-10884, 2017.

[58] S. Srinivasan, et al., “56 Gb/s Germanium waveguide Electro-Absorption Modulator,” *Journal of Lightwave Technology*, **34**, 419 – 424, 2017.

[59] Y. Tong, et al., "Compact and High-Speed Ge Franz-Keldysh I/Q Modulator Used with Kramers-Kronig Receiver," *2018 IEEE Photonics Conference (IPC)*, Reston, VA, 1-2, 2018.

[60] L. Mastronardi, et al., “High-speed Si/GeSi hetero-structure Electro Absorption Modulator,” *Opt Express*, **26**, 6663-6673, 2018.

[61] L. Mastronardi, et al., "56 Gbps Si/GeSi integrated EAM," *Proc. SPIE 10823, Nanophotonics and Micro/Nano Optics IV,* 108230D, 2018.

[62] S. M. Gates, and S. K. Kulkarni, "Kinetics of surface reactions in very low-pressure chemical vapor deposition of Si from SiH4," *Applied Physics Letters,* **58** (25), 2963-2965, 1991.

[63] B. Cunningham, J.O. Chu and S. Akbar, "Heteroepitaxial growth of Ge on (100) Si by ultrahigh vacuum, chemical vapor deposition," *Applied Physics Letters,* **59** (27), 3574-3576, 1991.

[64] E. A. Fitzgerald, S.B. Samavedam, Y.H. Xie and L. M. Giovane, "Influence of strain on semiconductor thin film epitaxy," *Journal of Vacuum Science Technology A,* **15** (3), 1048-1056, 1997.

[65] B. J. Spencer, P. W. Voorhees and S. H. Davis, "Morphological Instability in Epitaxially Strained Dislocation-Free Solid Films," *Physical Review Letters,* **67** (26), 3696-3699, 1991.

[66] H. Gao and W. D. Nix, "Surface Roughening of Heteroepitaxial Thin Films," *Annual Review Material Science,* **29**, 173-209, 1999.

[67] L. M. Giovane, H.-C. Luan, A. M. Agarwal, L. C. Kimerling, "Correlation between leakage current density and threading dislocation density in SiGe p-i-n diodes grown on relaxed graded buffer layers," *Applied Physics Letters,* **78** (4), 541-543, 2001.

[68] E. A. Fitzgerald, et al., "Totally relaxed Ge_xSi_{1-x} layers with low threading dislocation densities grown on Si substrates," *Applied Physics Letters,* **59** (7), 811-813, 1991.

[69] S. B. Samavedam, and E. A. Fitzgerald, "Novel dislocation structure and surface morphology effects in relaxed Ge/Si-Ge(graded)/Si structures," *Journal of Applied Physics*, **81** (7), 3108-3116, 1997.

[70] G.E. Beltz, et al., "A theoretical model for threading dislocation reduction during selective area growth," *Materials Science and Engineering: A*, **234**, 794-797, 1997.

[71] G. Kissinger and S. Pizzini, "Silicon, Germanium, and Their Alloys: Growth, Defects,

Impurities, and Nanocrystals," Springer International Publishing, 2014.

[72] B. Schwartz and H. Robbins, "Chemical etching of silicon: IV. Etching technology," *Journal of the Electrochemical Society*, **3**, 1903, 1976.

[73] H. Robbins and B. Schwartz, "Chemical etching of silicon: III. A temperature study in the acid system," *Journal of the Electrochemical Society*, **107**, 108, 1960.

[74] O. Madelung, et al., "Physics of Group IV Elements and III-V Compounds," *Numerical Data and Functional Relationships in Science and Technology*, **22a**, Springer, Berlin, 1987.

[75] O. Madelung, et al., "Properties of Group IV Elements and III- V, II- V, and I- VII Compounds," *Numerical Data and Functional Relationships in Science and Technology*, **17a**, Springer, Berlin, 1982.

[76] J. F. Liu, et al., "Deformation potential constants of biaxially tensile stressed Ge epitaxial films on Si (100)," *Phys. Rev B*, **70**, 155309, 2004.

[77] H. Shen, F. H. Pollak, "Generalized Franz-Keldysh theory of electromodulation," *Phys. Rev. B*, **42**, 7097, 1990.

[78] H. Shen, M. Dutta, "Franz-Keldysh oscillations in modulation spectroscopy," *J. Appl. Phys.*, **78**, 2151, 1995.

[79] F. H. Pollak and M. Cardona, "Piezo-electroreflectance in Ge, GaAs, and Si," *Phys. Rev.* **172**, 816, 1968.

[80] M. Chandrasekhar and F. H. Pollak, “Effects of uniaxial stress on the electroreflectance spectrum of Ge and GaAs,” *Phys. Rev. B,* **15**, 2127, 1977.

[81] A. R. Gohi, K. Syassen, M. Cardona, “Direct-band-gap absorption in germanium under pressure,” *Phys. Rev. B,* **39**, 12921, 1989.

[82] B. Welber, M. Cardona, Y. F. Tsay, B. Bendow, “Effect of hydrostatic pressure on the direct absorption edge of germanium,” *Phy. Rev. B,* **15**, 875, 1977.

[83] G. H. Li, A. R. Goii, K. Syassen, M. Cardona, “Intervalley scattering potentials of Ge from direct exciton absorption under pressure,” *Phys. Rev. B,* **49**, 8017, 1994.

[84] 1. Balslev, “Influence of uniaxial stress on the indirect absorption edge in Silicon and Germanium,” *Phys. Rev.* **143**, 636, 1966.

[85] J. J. Hall, “Large-strain dependence of the acceptor binding energy in Germanium,” *Phys. Rev.* **128**, 68, 1962.

[86] A. P. Smith III, M. Cardona, F. H. Pollak, “Band structure of Germanium under uniaxial stress,” *Am. Phys. Soc.,* **12**, 101, 1967.

[87] J. C. Hensel and K. Suzuki, “Quantum resonances in the valence bands of germanium. II. Cyclotron resonances in uniaxially stressed crystals,” *Phys. Rev.* **B9**, 4219, 1974.

[88] D. Ma, Y. Lin, J. Michel, “Strained Germanium Silicon Modulators Array for Integrated High Speed Broadband Modulation,” *PCT International Patent/US19/53353,* filed Sept. 27, 2019.

[89] Y. Lin, D. Ma, K. Lee, J. Michel, C. Tan, “A self-aligned dry etching method for mechanical strain enhancement of germanium and its uniformity improvement for photonic applications,” *Silicon Photonics XIII* 10537, 1053704, 2018.

[90] C. Pickering, et al., “In-situ dual-wavelength and ex-situ spectroscopic ellipsometry studies of strained SiGe epitaxial layers and multi-quantum well structures,” *Thin Solid Films,* **233**, 126-130, 1993.

[91] A. Adachi, “Silicon-Germanium Alloy (Si_xGe_{1-x}). In: Optical Constants of Crystalline and Amorphous Semiconductors,” Springer, Boston, MA, 1999.

[92] A. Frova and P. Handler, “Franz-Keldysh effect in the Space-Charge Region of a Germanium p-n junction,” *Phys. Rev.,* **137**, A1857, 1965.

[93] A. Frova, P. Handler, F. A. Germano, and D. E. Aspnes, “Electro-absorption effects at the band edges of silicon and germanium,” *Phys. Rev.,* **145**, 575, 1966.

[94] B. O. Seraphin and R. B. Hess, “Franz-Keldysh effect above the fundamental edge in germanium,” *Phys. Rev. Lett.,* **14**, 138, 1965.

[95] J. Humlicek, M. Garriga, M. I. Alonso, and M. Cardona, “Optical spectra of Si_xGe_{1-x} alloys,” *J. Appl. Phys.,* **65**, 2827, 1989.